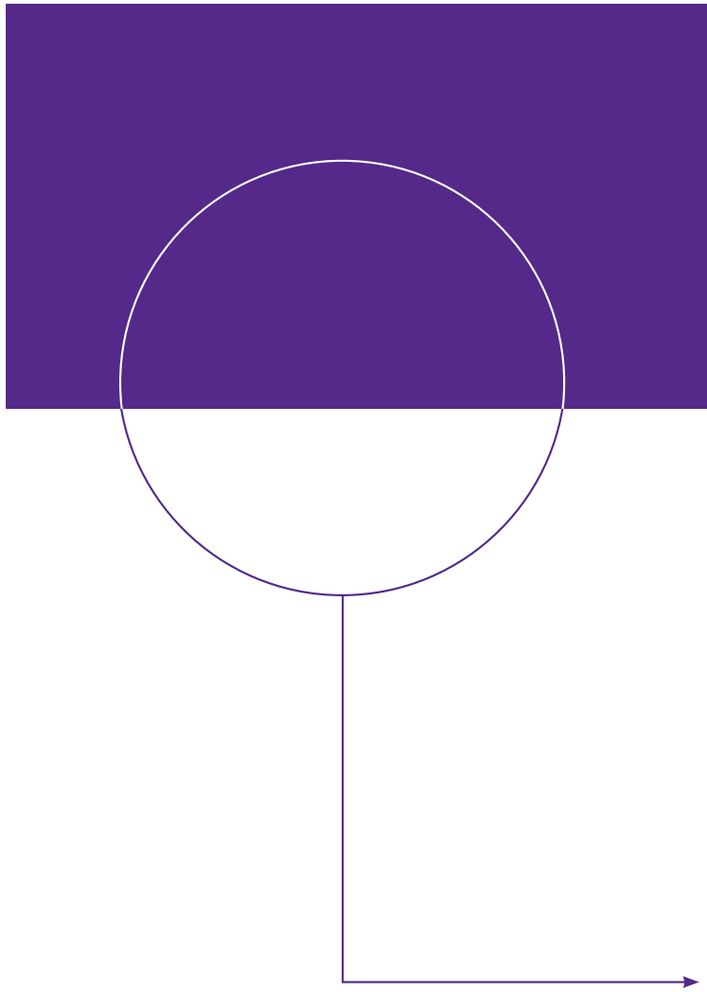

Master's thesis

2019

Abdulrahman Toutounji

NTNU
Norwegian University of
Science and Technology
Faculty of Natural Sciences
Department of Chemical Engineering

Abdulrahman Toutounji

Methodology Development for the Characterization of Carbon Formed in the Direct Process

June 2019

NTNU
Norwegian University of
Science and Technology

NTNU
Norwegian University of
Science and Technology

NTNU

Norwegian University of
Science and Technology

Methodology Development for the Characterization of Carbon Formed in the Direct Process

Abdulrahman Toutounji

Chemical Engineering
Submission date: June 2019
Supervisor: Hilde Johnsen Venvik, IKP
Co-supervisor: Edd Anders Blekkan, IKP
Mehdi Mahmoodinia, IKP

Norwegian University of Science and Technology
Department of Chemical Engineering

Preface

This master's thesis has been made as a completion of the MSc. degree in Chemical Engineering at the Norwegian University of Science and Technology (NTNU) in Trondheim. The thesis work has been done at the Department of Chemical Engineering (IKP) in the Spring semester of 2019. Professor Hilde J. Venvik acted as the main supervisor with Professor Edd Blekkan and researcher Mehdi Mahmoodinia acting as co-supervisors.

I would like to express my sincere gratitude to my supervisor Professor Hilde J. Venvik for guiding me throughout the thesis work and for providing valuable academic support. I would also like to thank my co-supervisors Professor Edd Blekkan and researcher Mehdi Mahmoodinia for the continuous and priceless input on the thesis work. A big thanks to the Elkem team, especially Torbjørn Røe, for their support, feedback, and provision of samples.

The endless technical support and positive vibes from senior engineers Estelle M. Vanhaecke and Anne Hoff are gratefully acknowledged. They have also provided valuable technical training in order for the work to be done.

Finally, I would like to thank my family and friends for all the motivation and support throughout this work. Thanks to Dumitrita Spinu who helped and supported with the training for pyrolysis-gas chromatography experiments. Thanks also to Martin Meuche who provided great input on infrared spectroscopy measurements. Lastly, I am eternally grateful for the support and motivation provided by my parents throughout the two-year masters program.

Abstract

Silicone is one of the most important industrial products in our present time. The Müller-Rochow process, also known as the direct process, is the most efficient way to produce dimethyldichlorosilane, which is the key precursor to the silicone industry. The direct process is represented as a gas-solid-solid reaction where gaseous methyl chloride reacts with an alloy of silicon and copper known as the contact mass to produce methylchlorosilanes. The copper acts as a catalyst in this process, and a trace amount of promoters is usually added to the contact mass. Mechanism of the direct process has proven to be challenging to comprehend, and it is still debated until recent days. Deactivation of the contact mass is caused by the phenomena of undesired carbon formation. It would be highly beneficial to minimize carbon formation in order to optimize the efficiency of the direct process. The work in this thesis is focused on an investigation concerning the carbon formation phenomena in the direct process. The aim of this work is to develop a methodology to characterize the carbon formed in the direct process in order to understand its nature and what influences its formation in the direct process.

Three samples of contact mass obtained at different reaction temperatures and a sample of metallic copper exposed to methyl chloride have been examined in this thesis work. In addition, a sample of pure silicon has been examined in order to be used as a reference for non-reacted silicon. Investigations were carried out by using various characterization methods such as thermogravimetric analysis, pyrolysis-gas chromatography coupled with mass spectrometry, Raman spectroscopy, scanning electron microscopy correlated with energy dispersive X-ray spectroscopy, and X-ray diffraction. There is an attempt to extract carbonaceous species in a Soxhlet extraction setup from samples that have shown high carbon content. The obtained extract was then analyzed by using attenuated total reflection Fourier-transform infrared spectroscopy.

Thermogravimetric analysis was useful to observe the mass loss in the samples, and it was correlated with evolved gases detected by mass spectrometry. The results of pyrolysis-gas chromatography showed that the decomposition products of the samples are oxygenated carbon compounds. Raman spectroscopy was helpful to indicate the degree of disorder of the carbon in the samples and how it varies with process temperature. Reaction pits observed by scanning electron microscopy and the effect of process temperature were also obvious. Extracting the carbon from the contact mass and characterizing it would be highly beneficial for the aim of the project, but the infrared spectra did not show bands related to carbonaceous species. The work included in this thesis showed the crucial effect of temperature on carbon formation in the direct process and how free copper also plays a role in carbon formation.

Contents

List of Figures

List of Tables

1 Introduction

Ever since the 1940s and until recent days, silicone has proven to be one of the most valuable industrial products in the world. Due to its special characteristics and properties, silicone is implemented in various important products that are used by consumers. Considering its thermal aging resistance property, silicone is commonly used as an insulator for electrical cables and as elastomers for oven seals[1]. In addition, its chemical aging and weathering resistance property makes it an essential sealant for the construction industry [1]. Other applications of silicone include textile fabrics, healthcare products, and cosmetics [1]. Silicone is also known as siloxane polymers or polysiloxanes due to its molecular structure that is formed of an alternating chain of silicon and oxygen atoms identified as siloxane bond [2]. This backbone structure is of inorganic nature, but the compounds that are usually bonded to the silicon atom are of organic nature. This mix of organic and inorganic nature makes silicone a product with unique characteristics and properties. Those properties are emphasized as great thermal and oxidative stability, considerably low glass transition temperature, perfect dielectric properties, and suitable biocompatibility [2]. Another interesting aspect of the chemistry of silicone is that there is a variety of options to be selected for the organic part that is attached to the silicon such as methyl, phenyl, hydrogen, or amino groups [2]. The flexibility in the production and modification of silicone polymers leads to endless possibilities of usage. The most common form of silicone is known to be polydimethylsiloxane (PDMS) [2]. Polydimethylsiloxanes are the result of a hydrolysis reaction of dimethyldichlorosilane, which are the precursors to form the silicone monomers [1]. In other words, dimethyldichlorosilane is the key compound to the whole production process of silicones.

Production of dimethydichlorosilane is done through what is known as the Müller-Rochow process, also known as the direct process. In the year of 1940, Eugene G. Rochow and Richard Müller developed the Müller-Rochow process in order to produce methylchlorosilanes [3]. The motivation to produce siloxane polymers came from the fact that they were needed to optimize aircraft performance during the world war [3]. This process proceeds through a gas-solid reaction between elemental solid silicon and gaseous methyl chloride in the presence of a solid copper catalyst[4]. The mixture of silicon and copper solids is referred to as contact mass. The direct process provides the most economical way to produce methylchlorosilanes, and its most abundant product is dimethyldichlorosilane which is also the most desired product [4]. Due to its complexity, extensive research has been done in order to understand the reaction mechanism and the factors that affect the process. It would be economically beneficial to optimize the efficiency of the process by increasing the yield of dimethyldichlorosilane [4].

The Müller-Rochow process remains dominant in terms of production of dimethyldichlorosilane for the silicone industry. Even though this process has been discovered in the 1940s, the reaction mechanism remains ambiguous and questionable due to the complexity of the gas-solid-solid reaction. In addition to the formation of methylchlorosilanes, some byproducts are also formed during the direct process. One of the byproducts formed is carbon, and it is an undesirable product to have in the process. The presence of carbon hinders the formation of dimethyldichlorosilane and eventually leads to catalyst deactivation. It would be an advantage to comprehend the phenomena of carbon formation in order to enhance and improve the Müller-Rochow process.

1.1 Motivation

Even though carbon formation has a great influence on the direct process, not much studies have been reported on this matter. The aim of this report is to develop a methodology that can help in comprehending the surface phenomena that affect carbon formation in the direct process. The nature of the carbon has to be understood by applying different characterization methods. Preventing unwanted side reactions from occuring would be of great benefit for the economics of the process. For this reason, three samples of contact mass obtained at different reactor conditions are characterized by various characterization methods. As mentioned earlier, contact mass is a mixture of solid silicon and solid copper that has been exposed to methylchloride in a fluidized bed reactor. In addition, a sample of pure copper exposed to methyl chloride has also been characterized to evaluate the carbon formed on pure copper as well. A sample of pure silicon has been used as a reference. All the samples have been provided by Elkem Silicon Materials in Trondheim.

Thermogravimetric analysis along with differential scanning calorimetry were used in correlation with a mass spectrometer. Pyrolysis-gas chromatography was also connected to a mass spectrometer to detect the evolved compounds. Raman spectroscopy, scanning electron microscopy, energy dispersive spectroscopy, and X-ray diffraction were also used for characterization. In addition, the pure copper sample that has been exposed to methylchloride and the contact mass sample that is carbon rich were placed in a Soxhlet extraction experiment. Those samples were particularly chosen because they showed high carbon content. The extracts were then analyzed by the use of attenuated total reflection-fourier transform infrared spectroscopy.

2 Theory

2.1 The Müller-Rochow process

In order to carry out the Müller-Rochow process, elemental silicon is needed for the reaction. Silicon is the second most abundant element in the crust of earth, but it is naturally found bonded to oxygen in the form of silica[5]. Reduction of silica by the use of carbon at an elevated temperature of 3000°C was first reported by Henri Moissan, and it is still used for the industrial scale production of silicon[5]. The reduction of silica proceeds as seen in Equation 2.1[5]:

$$SiO_2 + 2\,C \longrightarrow Si + 2\,CO \tag{2.1}$$

In the year of 1940, Eugene G. Rochow found the basis for the modern silicone industry by an experiment where he reacted gaseous methylchloride with a 50% Cu-Si mixture in a tube furnace to produce methylchlorosilanes[5]. At the time Rochow was developing the synthesis of methylchlorosilanes, Richard Müller in Germany was also working on developing the same reaction but it was disclosed and continued after the world war[5]. The effort to produce silicones at that time is explained by the urge to develop the waterproof insulators for military aircraft[5].

The Müller-Rochow process remains the most economical and viable route to produce methylchlorosilanes for the silicone industry. The process proceeds in the form of a gas-solid-solid reaction, with solid silicon and gaseous methyl chloride as reactants in the presence of a solid copper catalyst. The use of copper catalyst by itself cannot provide high enough selectivity and reaction rate. Therefore, the addition of trace amounts of promoters is necessary to enhance the selectivity and rate of reaction[6]. Commonly used promoters are zinc, tin, aluminum, and phosphorous. The most widely used in the industry are zinc and tin due to their high efficiency to boost the performance of the process[6]. The role of the promoters and their influence on the direct process will be further discussed later on. The reaction is conventionally carried out in a fluidized bed reactor at a temperature range between 280°C to 350°C[7]. The general reaction equation proceeds as in Equation 2.2:

$$Si_{(s)} + CH_3Cl_{(g)} \xrightarrow{Cu(s)} (CH_3)_xH_ySiCl_z \tag{2.2}$$

where $(x+y+z) = 4$. As mentioned earlier, dimethyldichlorosilane is the most abundant and most desired product obtained from the direct process.

Table 2.1: Products of the direct process and their boiling points[4]

Product	Formula	Boiling Point (°C)
Methyldichlorosilane	$(CH_3)HCl_2Si$	40.7
Trimethylchlorosilane	$(CH_3)_3SiCl$	57.9
Methyltrichlorosilane	$(CH_3)SiCl_3$	66.4
Dimethyldichlorosilane	$(CH_3)_2SiCl_2$	70.3
Tetramethylsilane	$(CH_3)_4Si$	26.6
Trichlorosilane	$HSiCl_3$	31.5
Dimethylchlorosilane	$(CH_3)_2HSiCl$	36.0
Silicon tetrachloride	$SiCl_4$	57.6

In addition to dimethyldichlorosilane, other monomers with low boiling points are also produced in the direct process at a low yield. The products of the direct process and their boiling points are shown in Table 2.1.

Methyldichlorosilane, trimethylchlorosilane, methyltrichlorosilane, and dimethyldichlorosilane are identified as the prinicipal monomers. On the other hand, tetramethylsilane, trichlorosilane, dimethylchlorosilane, and silicon tetrachloride are identified as trace monomers[4]. In addition to the low boiling point products, Ward also referred to products with boiling points higher than 80°C as the residue which consist mainly of disilanes[4]. Launer has also indicated the formation of hydrocarbons during the direct process reaction[8]. Presence of those hydrocarbons makes it difficult for the distillation of methylchlorosilanes. It has been reported that these hydrocarbons may result from impurities in the methyl chloride feed[8]. Hydrocarbon by-products were observed to be alkanes and alkenes with branched structures[8].

According to Acker and Bohmhammel, the typical yield range of dimethyldichlorosilane is in the range between 83 mol% and 93mol%[9]. It has been reported that the product distribution and the yields of the products from the direct process are influenced by several parameters such as[9]:

- Preparation of the catalyst and the added promoters
- Process temperature and pressure
- Type of reactor and its geometry
- Impurities in the used silicon
- Inhomogeneiety in the composition of the catalyst

All these factors indicate the complexity of the direct process and how unpredictable it can be in some aspects.

2.1.1 Mechanism of the direct process

Even though the direct process has been discovered since the year 1940, the mechanism of the reaction remains debatable until recent times. Researchers are still investing their knowledge and efforts in order to set a clear mechanism to one of the most important and complex processes in the world today.

The first proposal for a reaction mechanism was done by Rochow and Hurd in 1945[10]. The proposed mechanism was built on the theory that role of copper is to be a chlorine transporter from the methyl chloride to the silicon in the form of copper(I) chloride[10]. The formation of copper(I)chloride is done by reacting the copper with methyl chloride as a first step in the mechanism.
After copper(I) chloride is obtained, it reacts in an exothermic manner with silicon to produce Si-Cl. Rochow and Hurd reported that Si-Cl is the activated intermediate form of silicon that reacts with free methyl radicals[10]. The free methyl radicals were explained to be obtained by the decomposition of methyl-copper. The full reaction order proposed by Rochow and Hurd is stated as the following[10]:

$$2\,Cu + CH_3Cl \longrightarrow CuCl + CuCH_3 \tag{2.3}$$

$$Si + CuCl \longrightarrow Cu + (Si{-}Cl) \tag{2.4}$$

$$(Si{-}Cl) + \cdot CH_3 \longrightarrow CH_3SiCl \tag{2.5}$$

$$(Si{-}Cl) + CuCH_3 \longrightarrow CH_3sicl + Cu \tag{2.6}$$

$$(Si{-}Cl) + CuCl \longrightarrow SiCl_2 + Cu \tag{2.7}$$

Reactions 2.6 and 2.7 are possible alternatives to reaction 2.5. The reactions proposed by Rochow and Hurd make the mechanism of heterogeneous-homogeneous nature. This proposed mechanism was not accepted by the researchers that were working in the same field. Voorhoeve has stated several objections on Rochow and Hurd's proposed mechanism such as[7]:

- The proposed mechanism suggests a random product distribution while the process is selective towards dimethyldichlorosilane
- The proposed mechanism suggests the importance of initial chlorination of silicon, but tetramethylsilane is one of the products and that denies the stated silicon chlorination importance.

- The proposed mechanism does not show why copper is important to produce dimethyldichlorosilane in a selective manner.

Lead researchers in the field such as Voorhoeve, Klebansky, Fikhtengolts, and Bazant moved on after that to believe that the process is heterogeneous where a silicon-copper alloy, Cu_3Si, is responsible for the selectivity towards dimethyldichlorosilane. Therefore, it has been assumed that the process mechanism proceeds by the dissociative adsorption of methyl chloride on the contact mass[7]. Based on that assumption, Klebansky and Fikhtengolts proposed a mechanism in which the adsorption of methyl chloride is depends on its own dipole momentum. In addition, it also depends on the charge distribution in the silicon-copper alloy[11]. Upon reaction, the methyl group will be bonded to the silicon and the chlorine will be bonded to the copper as seen in Equation 2.8:

$$Cu^{\delta+} - Si^{\delta-} + CH_3^{\delta+} - Cl^{\delta-} \longrightarrow \begin{matrix} & & \mathrm{Cl} & \cdots & \mathrm{CH_3} \\ & & \vdots & & \vdots \\ \mathrm{Cu} & \cdots & \mathrm{Si} & & \end{matrix} \tag{2.8}$$

After that, a rearrangement occurs as the following:

$$\begin{matrix} \mathrm{Cl} & \cdots & \mathrm{CH_3} \\ \vdots & & \vdots \\ \mathrm{Cu} & \cdots & \mathrm{Si} \end{matrix} \longrightarrow \mathrm{Cu} + \mathrm{R}\begin{matrix} & & \mathrm{X} \\ \diagdown & \diagup & \\ & \mathrm{Si_{ads}} & \end{matrix} \tag{2.9}$$

Joklik, Kraus, and Bažant suggested a similar mechanism with one difference where the adsorption will occur by having a bond between the methyl group and the copper and a bond between the silicon and chlorine[12]. Bažant and his coworkers also proposed that the reaction of the contact mas with methyl bromide would give a faster reaction rate than the reaction with methyl chloride[12]. However, Voorhoeve discusses that Bažant and his coworkers interpretation does not agree with the fact that the reaction with methyl bromide needs a higher activation energy (37kcal/mole) than the activation energy for the reaction with methyl chloride (25.3kcal/mole)[7]. Recently, Zhang and his coworkers also proposed a possible reaction mechanism for the direct process where they used CuO as a catalyst. The catalyst is first mixed with the silicon to form an interface. When methyl chloride is introduced at high temperatures, it reacts with the oxygen and gives Cu* as a result. Cu* diffuses into the Si surface and the Cu_3Si alloy is formed[13]. Adsorption of the methyl chloride occurs and and the Si*, which is very unstable, is used up to produce dimethyldichlorosilane. During the reaction, carbon deposition will occur on the the Cu_3Si surface leading to the deactivation of the contact mass[13]. The reaction mechanism still remains a challenge to interpret, and many efforts are still being put into comprehending it.

2.1.2 Copper as a catalyst

In order to have an efficient production of methylchlorosilanes, it is necessary to utilize copper as a catalyst in the direct process. Using copper as a catalyst along with a trace amount of promoters enhances the rate of the reaction and increases the selectivity towards dimethyldichlorosilane, which is the most desired product. According to Clarke, after a long induction period of 31 hours at a temperature of 670 Kelvin, reaction between silicon and methyl chloride yielded trichlorosilane ($HSiCl_3$) and dichloromethylsilane (CH_3HSiCl_2) as the main products with dimethyldichlorosilane being only a minor product[14]. The induction period is defined as the time needed for the formation of the active surface for methylchlorosilanes. During the induction period no silanes are formed, but methane, hydrogen, and carbon are formed instead[14]. It was proposed that the products of the induction period are a result of methyl chloride cracking on copper as shown in Equation 2.10[14].

$$2\,Cu + 2\,CH_3Cl \longrightarrow 2\,CuCl + CH_4 + H_2 + C \tag{2.10}$$

Contact masses containing silicon, copper(I) chloride, and trace amount of promoters have proven to have short induction periods. During the induction period when using copper(I) chloride, the surface would be rich in chlorinated products[14]. Reaction between copper(I) chloride and silicon is described in Equation 2.11.

$$4\,CuCl + n\mathrm{Si} \longrightarrow (n-1)\mathrm{Si} + 4\,Cu + SiCl_4 \tag{2.11}$$

After the chlorine transfer to the silicon, free copper will diffuse into the silicon to form Cu_3Si, known as the η-phase. When the catalyst is introduced as copper(I) chloride, it is expected to have shorter induction periods than when introducing the catalyst as copper[14].

Frank and his coworkers indicated that using an alloy of silicon-copper would decrease the induction period by more than two orders of magnitude[15]. Alloying silicon with copper to form Cu_3Si modifies the bonding to become weaker, and the formation of weaker bonds makes it faster and easier to oxidize silicon at room temperature[15]. Frank and his coworkers showed that using catalysts other than copper would shift the selectivity of the reaction towards products other than dimethyldichlorosilane, and they have proposed that the role of copper catalyst is the stabilizing or destabilizing effect on adsorbed species[15]. Frank and coworkers also indicated that the active sites for the formation of dimethyldichlorosilane have silicon bound to chlorine on the surface and concluded that the induction period is related to the time needed to form active sites with Si-Cl bonds rather than formation of Cu_3Si[15]. Voorhoeve reports that contact masses that contained the η-phase (Cu_3Si) yielded high selectivity towards

dimethyldichlorosilane while contact masses with free copper allowed the formation of cracked products[16].

The direct process has proven to be an efficient way to produce the Cu_3Si alloy. In general, the formation of Cu_3Si alloy requires temperatures above 800°C, but this is not the case for the direct process where the process temperature is typically less than 350°C. This suggests that the formation of Cu_3Si alloy in the direct process is due to a chemical process [14].

Two copper compounds have proven to be successful for industrial production of methylchlorosilanes. One of those compounds is copper(I) chloride which provides high activity, and the other compound is copper oxide which provides high reaction selectivity[17]. Wang and his coworkers proposed that a bi-component catalyst composed of copper(I)chloride and copper oxide gives better catalytic performance than mono-component catalysts. They have reported that increasing the proportion of copper(I) chloride leads to a faster start of the reaction[17]. This highlights the importance of copper(I) chloride in reducing the induction period. Using a bi-component catalyst showed an enhancement in the activity and higher conversion of silicon in the direct process[17].

2.1.3 Role of promoters

The addition of trace amounts of promoters to the contact mass is essential for the selectivity and reaction rate of the direct process. As mentioned earlier, zinc and tin are the most commonly used promoters in the industry due to their highly proven effectiveness in the direct process[6]. According to Gordon and coworkers, contact mass that was promoted with zinc provides high selectivity towards dimethyldichlorosilane. Contact mass that has been promoted with tin showed high reactivity and high conversion rates of silicon and methyl chloride[18]. Wang and coworkers reported that the optimal concentration of zinc in the contact mass should be 0.1%. Increasing the concentration of zinc beyond that would lead to lower dimethyldichlorosilane selectivity and zinc can become a poison if its concentration reaches 1% in the contact mass[6]. They have also discussed that zinc is necessary for the formation of the Cu_3Si η-phase and this is explained by its enhancement of silicon diffusion into the alloy phase. On the other hand, tin plays a role in activating the Cu_3Si alloy and consuming it[6].

Furthermore, Kim and Rethwisch concluded that zinc can decrease the activation energy for the reaction and for the formation of dimethyldichlorosilane. They have proposed that zinc has the ability to organize the dissociative adsorption of methyl chloride so that the methyl group would attach to the silicon. In addition, they have suggested that promotion with tin enhances the formation of active sites and the surface transfer of chlorine[19].

2.2 Catalyst Deactivation

The activity of a catalyst tends to decrease with time and this is what is known as catalyst deactivation. Catalyst deactivation is usually witnessed as a change in reaction rate, conversion rate, and/or selectivity. This can lead to a huge impact on the economics of a process due to loss of production and materials' costs. The issue of catalyst deactivation costs the industry billions of dollars per year[20].This is why it is essential to take catalyst deactivation into consideration when modelling a process. It is a phenomena that can not be avoided, but its harmful consequences can be reduced by acquiring more knowledge about the reaction mechanism and kinetics. Catalyst deactivation has been attributed to the following reasons[20]:

(i) Catalyst poisoning by impurities

(ii) Catalyst sintering, also known as thermal deactivation

(iii) Fouling of the catalyst by deposition of species on its surface

(iv) Vapor-solid reactions with the catalyst phase

(v) Solid-solid reactions with the catalyst phase

(vi) Mechanical failure due to attrition or crushing

The risk of catalyst poisoning can be handled by removing all possible harmful contaminants and impurities in the reactants prior to the reaction[21].As for sintering, it usually occurs at high reaction temperatures where either crystalline growth or support collapse occurs. Crystalline growth would lead to the loss of catalyst surface area, and support collapse would lead to the loss of support area[21]. This could be avoided by setting an appropriate temperature for the process without affecting the catalyst negatively[21]. Fouling leads to the blocking of active catalytic sites by deposition of species on the catalyst surface. A common example of fouling is the deposition of carbon or coke on the surface of the catalyst. According to Kumbilieva and his coworkers, the most common form of catalyst deactivation occurs by coke formation in a process[21]. The main focus will be on catalyst deactivation by coke formation due to its relevance to the work in this project.

Catalyst deactivation by carbon or coke formation is a potential problem for every process that involves hydrocarbons, carbon monoxide, and/or carbon dioxide in high temperature conditions. A main difference between coke and carbon is their origin. Carbon originates from the disproportion of carbon monoxide, while coke is a product of the decomposition of hydrocarbons on the surface of the catalyst.

The type of coke formed is dependent on the process conditions, and it may vary in form from being hydrocarbons with high molecular weight to primary carbon such as graphite[20]. According to Menon, deactivation by coke formation is based on the nature of the coke, where it has been deposited, and its structure[22]. Menon has classified catalytic reactions that are accompanied by coke formation either as coke-sensitive reactions or coke-insensitive reactions[22]. In case of coke-sensitive reactions, the coke that is deposited on the active site is not reactive. However, it is harmful and it leads to a decline in catalytic activity[22]. On the other hand, the coke formed in the coke-insensitive reactions is reactive in nature and can be removed by hydrogenation[22]. In addition to the nature of coke, the type of the catalyst being used has a high influence on the coke formation mechanism. For metal catalysts, Bartholomew reports that carbon may chemisorb or physically adsorb on the surface to block the reactants from reaching the active sites[20]. In addition, the carbon may either encapsulate metal particles leading to their deactivation or plug micro and mesopores so that reactants would not have access [20].

2.2.1 Carbon formation in the direct process

The direct process is also a victim of carbon formation which eventually leads to deactivation. Carbon formation makes it obligatory to continuously replace spent contact mass with fresh contact mass in order to proceed with the production of methylchlorosilanes. It has been reported that coke resulting from the cracking of methyl chloride will be deposited on the surface of the contact mass and this would limit the diffusion of copper into the silicon matrix leading to deactivation[23]. According to Luo and coworkers, premature deactivation of the contact mass could be avoided by better catalyst dispersion and by having less copper enrichment[23]. They have also reported that there was no peak obtained for carbon in X-ray diffraction and concluded that the carbon formed is of amorphous form[23]. It was reported that the main factor contributing to deactivation is the enrichment of free copper on the surface where methyl chloride decomposes to give high levels of carbon and chlorine[23]. Methyl chloride cracks on free copper as described in Equation 2.12:

$$Cu + CH_3Cl \longrightarrow CuCl + CH_3\cdot \tag{2.12}$$

The organic methyl radical continues to decompose to carbonaceous species and hydrogen[16]. According to Voorhoeve and Vlugter, converting free copper into the active η-phase would lead to a higher conversion of silicon into methylchlorosilanes. The conversion of free copper into the active η phase was done by heat treatment of the contact mass at 400°C in inert argon atmosphere, and this has resulted in a higher percentage of silicon conversion[16].

In addition, Anderson and McConkey showed that methyl chloride decomposes on pure copper to form hydrogen and carbon on the surface between 0°C and 200°C[24]. Wessel and Rethwisch also reported about the formation of carbonaceous residue on the surface of the contact mass and how it can block the active sites for silanes production. They have reported the formation of two different types of coke that were witnessed from temperature programmed oxidation, which are the α-coke and β-coke[25]. Those two types of coke differ by chemical composition where the α-coke has a higher hydrogen/carbon ratio. The formation of α-coke had no effect on the activity of the reaction, but deactivation was related to the formation of β-coke on the surface of copper-silicon contact mass promoted with zinc and tin[25]. Coke formation on non-promoted contact mass was higher than that on promoted contact mass, but the promoted contact mass suffered from a more thourough deactivation[25]. It was concluded that the coke formed on promoted contact mass is deposited on the active sites leading to deactivation, and a proposed method to reduce deactivation is to flush hydrogen into the reactor feed which leads to less coke formation[25]. According to Kim and Rethwisch, the ratio of hydrogen/methyl groups in the total products of the reaction can be used as an indicator to how much coke is formed[19]. Applying higher temperatures to the reaction resulted in higher hydrogen/methyl ratios and consequently higher coke formation on the surface of the catalysts. An increase in coke formation was accompanied with higher chlorine and hydrogen content in the process products and less methyl group in the products[19]. Kim and Rethwisch revealed that using only zinc as a promoter would lead to higher methyl fractions and lower chlorine and hydrogen fractions in the reaction products[19]. In another study that was done by Zou and coworkers, it has been declared that promoting copper oxide (CuO) with tin dioxide (SnO_2) reduces the rate of coke formation and deactivation of the contact mass[26].

Furthermore, Frank and his coworkers declared a graphitic carbon concentration up to 85% on the surface of zinc promoted contact mass. Although the carbon concentration was high, selectivity towards dimethyldichlorosilane still appeared to be high. This showed that the graphitic carbon did not seem to block the active sites in this case[15]. Graphite concentration increased with the increase of process temperature, and it was proposed that the graphite might have been produced from carbide[15].

2.3 Characterization and experimental methods

Selection of characterization methods for the samples has been done after a thorough literature review. Wessel and Rethwisch have conducted thermogravimetric analysis experiments to study the deactivation of contact mass by coke formation[25]. Banholzer and coworkers performed scanning electron microscopy to study the topography and the reaction pits of reacted contact mass[27]. It is important to point out that it was desirable to use a scanning

(transmission) electron microscopy (S(T)EM) to get higher resolution images, but this was not possible due to technical issues with the instrument. X-ray diffraction has been reported for the characterization of contact mass and it was used by Zou and coworkers to study the structure of the contact mass[26]. Even though Raman spectroscopy is widely used for the study of carbon materials, no literature has been found about the use of Raman spectroscopy for the characterization of contact mass from the direct process. In addition, pyrolysis-gas chromatography has also not been reported to be used for the characterization of contact mass. However, it is of interest to check for byproducts of the direct process and their decomposition compounds. Soxhlet extraction has been also used in order to extract the carbonaceous species from the samples by the use of dichloromethane in order to characterize the carbon without other components. The extract was then characterized by using attenuated total reflection Fourier-transform infrared spectroscopy. This section includes theoretical background about all characterization methods that have been used and about soxhlet extraction.

2.3.1 Thermogravimetric Analysis (TGA)

Thermogravimetric analysis is an analytical technique that is used in order to measure the mass change (loss or gain) as a function of temperature, time, and atmosphere. Measurements could be carried out in an oxidative atmosphere by using a flow of air, or it can be carried out in an inert atmosphere by using an inert gas flow such as argon or helium. Typically, few milligrams of the sample are placed in a small pan and suspended into the microbalance of the instrument. Cleaning the used pan is necessary after every experiment to remove any possible residues. There is usually an empty reference pan placed inside the instrument. The thermogravimetry instrument must be calibrated prior to measurements and this is done by creating a correction file for the temperature profile and the gas flows. The measurement is initiated with a controlled gas flow along with a linear temperature ramp. Users have the option to hold the temperature at isothermal conditions if desired. Some instruments can also measure the heat flow into the pan by differential scanning calorimetry which will be explained further.

At the end of the measurement, a profile of mass change versus time and temperature is obtained. This profile could show mass gain or mass loss. Mass loss could be explained by decomposition of the materials being tested, reduction of the materials, evaporation of volatiles, and possibly desorption as well. On the other hand, mass gain could be justified by the oxidation of the materials and could also be accredited to absorption or adsorption phenomenas. It is also important to point out that the results obtained could differ according to the applied heating rate and the initial mass of the sample.

According to MacCallum, if the material being tested is not homogeneous, the sample that is placed in the pan may not represent the whole material[28]. Thermogravimetric analysis has proven to be useful to analyze the thermal stability of materials and to perform kinetics studies[28]. It is one of the mostly used characterization methods for carbon materials in order to comprehend carbonization of different precursors and the oxidation of carbonaceous species for stabilization[29]. In addition, theromogravimetric analysis is often correlated with mass spectrometry in order to determine the gases evolving from the sample.

2.3.2 Differential scanning calorimetry

As mentioned earlier, differential scanning calorimetry (DSC) is also obtained from the same instrument used for thermogravimetric analysis . Differential scanning calorimetry is an analysis technique that measures the needed heat flux or power supply to have no difference in temperature between the sample and a reference that are are placed at an isothermal temperature or in a heating/cooling environment[30]. This technique could be used to determine the melting temperature and the crystallinity of the sample[30]. Differential scanning calorimetry can give information about endothermic and exothermic effects, the specific heat capacity, phase transitions, and reaction enthalpies[31]. There are two types of differential scanning calorimetry: heat-flux DSC and power compensation DSC[32]. In both types of differential scanning calorimetry the measured signal is proportional to the rate of heat flow[32]. For the heat-flux DSC, the primary measurement signal is temperature difference between the sample and the reference[32]. Any changes in the enthalpy of the sample will lead to a change in its temperature relative to the reference. The temperature difference is given in terms of voltage. Enthalpy changes are an indication of exothermic or endothermic phases. The heat balance equation for the heat-flux DSC is as follows[33]:

$$\frac{dH'}{dt} = \frac{T_{SP} - T_{RP}}{R_D} + (C_S - C_R)H + C_S \frac{R_D + R_S}{R_D} \frac{d(T_{SP} - T_{RP})}{dt} \tag{2.13}$$

where T_{SP} = temperature of sample;

T_{RP} = temperature of reference;

R_D = thermal resistance between the wall of the furnace and the sample or reference;

C_S,C_R = heat capacity of the sample and the reference respectively;

R_S = thermal resistance between the sample and the reference;

H = imposed heating rate;

The term $\frac{dH'}{dt}$ is a description for the heat evolution of an exothermic transition. The term $\frac{T_{SP}-T_{RP}}{R_D}$ is a representation of the area below the DSC peak. In order to determine the specific heat, the term $(C_S - C_R)H$ is used.

It is important to take into consideration that part of the heat is consumed by the sample, and this is the purpose of the term $C_S \frac{R_D+R_S}{R_D} \frac{d(T_{SP}-T_{RP})}{dt}$ [33].

2.3.3 Pyrolysis-gas chromatography-Mass spectrometry

Analytical pyrolysis-gas chromatography (Py-GC) is a separation technique that allows the separation of compounds based on their boiling points and polarities. Temperatures that are used in this technique are usually high in order to have chemical changes in the sample being tested[34]. This is done by the application of high heat in the absence of oxygen which makes it a destructive technique. According to Wampler, reactions in pyrolysis-gas chromatography include dehydration, decarboxylation, and bond dissociation to form free radicals to a large extent[34].Large molecules are broken down into smaller volatile fragments and those elude to the gas chromatography where they are analyzed. Introduction of the sample into the instrument is commonly done by the use of an autosampler. The use of an autosampler offers higher precision than manually injecting the sample[35]. In addition, using an autosampler is more efficient than manual injection and provides a higher sample throughput[35]. Samples typically consist of 0.1 to 0.5 milligrams and they are placed in small cups in the autosampler. There are three most commonly used pyrolyzers: the microfurnace, Curie-point, and the resistively heated filament. In this project, a microfurnace is used with a capillary column and a mass spectrometer. A microfurnace can increase the temperature rapidly to the pyrolysis temperature and keep it constant for the desired pyrolysis time[36]. It is essential to transfer the products in a fast and efficient manner from the pyrolyzer to the gas chromatography column. The interface between the pyrolyzer and the column must be kept hot to avoid cold spots and condensation of the compounds[36].

Chromatographic systems consist of a mobile phase and a stationary phase. The mobile phase is defined as the carrier gas that is used to transport the resulting volatile compounds towards the stationary phase. Separation of the various compounds is possible due to their affinities towards the mobile and stationary phases[35]. The carrier gas is usually an inert gas such as helium, nitrogen, or argon. Each compound has a specific distribution constant which makes the separation possible. The distribution constant is defined as the ratio of solute concentration in the stationary phase to its concentration in the mobile phase as seen in Equation 2.14[35]:

$$K_c = \frac{C_{stationary}}{C_{mobile}} \tag{2.14}$$

The values of the distribution constant explain how fast a compound moves in the chromatography system. High values of distribution constant refer to slow compound movement, and low distribution constant values refer to

faster compound movement[35]. The abundance of the peak of a compound in the obtained chromatogram is an estimation of the amount of the compound present.

The column is the most important part of the gas chromatograph. Golay invented the capillary column in 1958 and it became the most commonly used column because of its high resolution[35]. The stationary phase is on the inner walls of the capillary column and the inert carrier gas passes through the hollow tube. The column is chosen based on four main factors that could affect separation: thickness of the column, its length, its diameter, and the chemical nature of the stationary phase[35]. The column is placed inside an oven where the temperature can be programmed. After separation occurs in the column, the volatile compounds are directed towards a coupled detector which is most commonly a mass spectrometer. Mass spectrometry provides valuable information to identify the various compounds. The compounds will be ionized in the mass spectrometer and fragmented into several ions. After that, the ions are arranged according to their mass-to-charge ratios and detected to form a mass spectrum[35]. A typical configuration of pyrolysis-gas chromatography/mass spectrometry system is represented in Figure 2.1.

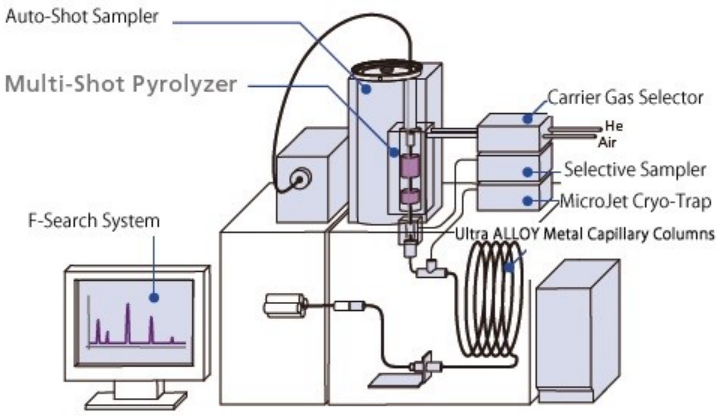

Figure 2.1: Typical Py-GC/MS setup

2.3.4 Raman spectroscopy

Spectroscopic techniques are utilized in order to observe the interaction of electromagnetic radiation with matter. Those techniques can be based on the aspects of emission, scattering, fluorescence, and absorption[37]. Light scattering by sound waves has been observed in 1928 by Sir C.V. Raman whom the characterization method is named after[38]. Raman spectroscopy is a non-destructive technique that can be used qualitatively by measuring the frequency of the produced scattered radiations, and it can be used quantitatively by measuring the intensity of those scattered radiations[37]. Raman spectroscopy is mainly based on the Raman effect which is defined as the difference between the frequency of a little fraction of the scattered radiations and the frequency of the

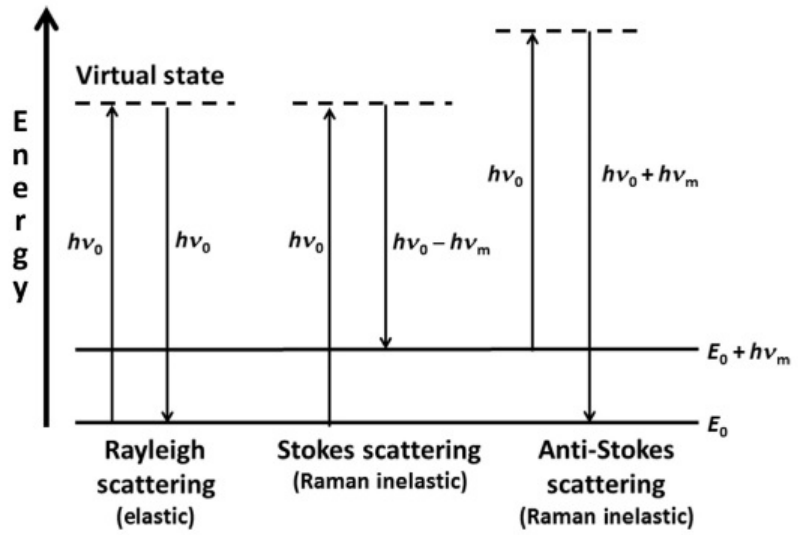

Figure 2.2: Representation of Rayleigh, Stokes, and anti-Stokes scattering. E_0 is the lowest energy state, upward arrow is for lower energy, and downward arrow is for the scattered energy[41]

monochromatic incident radiation[37]. Raman scattering is the result of the inelastic scattering of light photons due to the excitation of the material by an energy source[38]. The scattered light is generated by the interaction between a monochromatic laser beam and the molecules in the material being tested. The difference in frequencies between the incident light and the scattered light is used to build up the Raman spectrum. The incident laser beam has a frequency denoted as ν_o, and the frequency shift ν_m is related to the vibration of the material. Raman shift(cm^{-1}) is correspondant to $\frac{\nu_m}{c}$, where c is the speed of light[39]. If the scattered radiations have the same frequency as the incident radiation, this is referred to as Rayleigh scattering. In addition, if the incident radiation has a higher frequency than the scattered radiations, Stokes lines will be observed in the Raman spectrum. Stokes scattering is denoted as ν_o - ν_m[39]. Anti-stokes lines will appear in the Raman spectrum if the scattered radiations have a higher frequency than the incident radiation[37]. Anti-stokes scattering is denoted as $\nu_o + \nu_m$[39]. Stokes bands are known to have a higher intensity than anti-stokes and therefore it is the Stokes bands that are measured in Raman spectroscopy[39]. A graphical representation of the scattering is shown in Figure 2.2. There are some factors that can affect the quality of the Raman spectra such as the instrument's stability, sufficient resolution, and high signal to noise ratio[39]. An advantage in Raman spectroscopy is that sample preparation is easy.

A Raman spectrometer is typically composed of an excitation source (laser), a sample holder, a detector, and a wavelength selector. There two types of Raman spectrophotometers: dispersive and non-dispersive. In this project, a dispersive Raman spectrophotometer that uses grating has been utilized. Obtained Raman spectra are presented in the intensity versus the wavelength shift, and the spectra can be measured in the range of 4000-10cm^{-1}[37].

Raman spectroscopy has been used since the 1970s to characterize carbon materials such as graphite, graphene, and amorphous carbon[40]. Raman spectra of carbon materials can reflect their structure since the spectrum is responsive to imperfections in the structure such as lattice defects[39].

2.3.5 Scanning electron microscopy (SEM)

Scanning electron microscopy is a technique that is used in order to characterize the topography, composition, physical properties, and chemical properties of various materials. Knoll was the first to show the principle of scanning electron microscopy in 1935 and it was first developed by von Ardenne in 1938[42]. A scanning electron microscope utilizes a high-energy electron beam to scan the surface of the material. The electrons that are emitted from this beam have an energy that is in the range of 0.1keV to 30keV. The electron beam interacts with the sample by what is known as scattering events. This leads to the emission of electron signals from the surface of the sample which are either backscattered electrons (BSE) or secondary electrons (SE). The resulting electron signals are collected by a detector and combined in order to form images. The chamber inside the instrument, where the sample is situated, is operated in high vacuum in order to avoid undesired scattering.

Backscattered electrons are beam electrons that are generated by elastic scattering[43]. They are emitted after scattering with a significant fraction of the incident energy still intact. Backscattered electrons usually have an energy that is higher than 50eV and they provide valuable information about the composition, topography, and crystallography of the material being characterized[43]. On the other hand, secondary electrons are the result of inelastic scattering and they are emitted from the surface of the sample with kinetic energy values lower than 50eV[43]. They are generated along the trajectory of the beam electron, but only a minimal fraction can reach the surface of the sample and escape. Secondary electrons signal is used for topographical investigations and they are usually detected by the use of an Everhart-Thornley detector(ETD). Everhart and Thornley enhanced secondary electron detection in 1960 by developing this detector which has a positively biased grid for the collection of electrons, a scintillator that converts electrons to light, and a light pipe that directs the light towards a photomultiplier tube[42]. This type of detector was used in this project to detect emitted secondary electrons signals.

In addition to secondary and backscattered electrons, characteristic X-ray photons are also produced upon contact of the high-energy electron beam with the material. Characteristic X-rays can be used in order to identify the elements that are present within the sample. An energy dispersive X-ray spectrometer (EDS) is used in order to detect characteristic X-rays. Energies of the atomic shells of an element are well defined, hence the X-ray photons have an energy that is a characteristic of the atom emitting it[43].

The scanning electron microscope consists mainly of an electron gun, a lens system, and detector(s). The electron gun is responsible for the production and acceleration of electrons, the lens system generates the electron probe and scans it, and the detector(s) are for detecting the scattered secondary and backscattered electrons[44]. In general, there are three different electron guns that are usually utilized in scanning electron microscopy and they are the thermoionic emission gun, the Schottky-emission gun, the field emission gun[44]. For this project, an instrument equipped with a Schottky-emission gun was used. The cathode of the Schottky gun is made of a single crystal tungsten (W) that is coated with zirconium oxide (ZrO), and it is possible to generate high emission current at a low cathode temperature[44]. An example of the scanning electron microscope system can be seen in Figure 2.3.

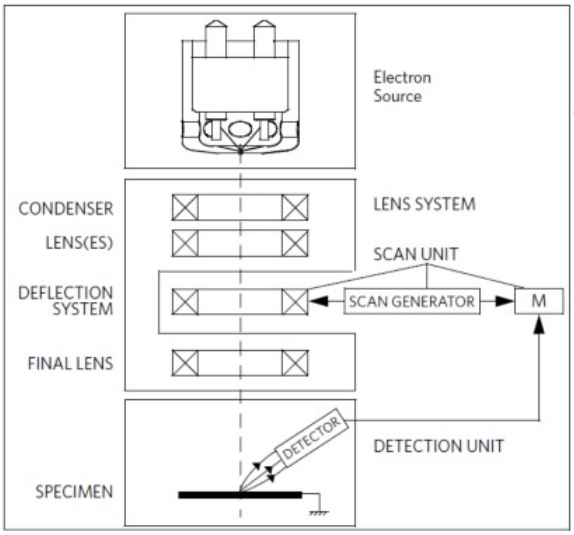

Figure 2.3: Example of the scanning electron microscope setup

2.3.6 X-ray diffraction (XRD)

X-ray diffraction is a non-destructive technique that is used in order to study the structure and the phase composition of the material. If a material is crystalline enough to diffract X-rays, X-ray diffraction method can be used for qualitative and quantitative analysis. Crystals can diffract X-rays in a characteristic manner and this allows the identification of the structure of crystalline phases[45]. Interactions of the generated X-ray photons with the material will lead to elastic scattering of the X-ray photons in a periodic lattice. As a result, constructive or destructive scattered radiation will occur which in turn generates the the characteristic diffraction phenomena[45]. W.L. Bragg explained the geometrical analysis of the X-ray diffraction phenomena by stating Bragg's law that is written in Equation 2.15[46].

$$n\lambda = 2d.\sin\theta \tag{2.15}$$

where n is an integer that is named the order of reflection, λ is the wavelength, d is the interplanar lattice spacing between the crystal planes, and θ is the angle of diffraction of the beam. Measurement of the diffraction pattern is typically displayed as intensity distribution as a function of 2θ angle. The intensity of the peak provides information about the crystal structure, and the shape of the peak can provide information about the crystallite size[45]. There are several factors that can affect the shape of the diffracted signal and the obtained signal is a convolution of heterogeneity of the composition, crystal defects (dislocations and stacking), and instrumental broadening[45]. Data of the d-values and relative intensities of diffraction lines are collected, and then they are compared to standard data from the Powder Diffraction File (PDF) database in order to identify the material[46]. The Scherrer equation can be used in order to calculate the crystallite size as shown in Equation 2.16:

$$L = \frac{k\lambda}{\beta.\cos\theta} \tag{2.16}$$

where L is the size of the crystallite, k is a constant close to 1, λ is the wavelength of the X-ray, β is the width at half peak height, and θ is the angle of diffraction.

2.3.7 ATR-FTIR

Infrared spectra are used in order to determine the molecules that are present in a sample. Peak positions that are obtained from the spectra usually correlate with specific molecular structures. Each material has a unique combination of atoms resulting to the formation of a unique infrared spectrum. In addition, the size of the peaks obtained from the spectrum indicates the amount of the molecules relevant to that specific peak. Fourier transform-infrared spectroscopy (FTIR) is a vibrational spectroscopic technique based on the excitation of molecules that can absorb infrared light. One of the prominent advantages of FTIR is measuring the spectra with a high signal-to-noise ratio where this ratio indicates the quality of the peak formed[47].

Another advantage is that FTIR spectrometers offer a high precision with wavenumbers which makes it possible to reproduce the infrared spectrum in a fast manner[47]. Major components of the FTIR spectrometer are the infrared source that emits the infrared radiation, the interferometer, the beam splitter, a detector, and the laser. The setup also includes reflecting mirrors to direct the infrared light[48]. The essential piece of hardware in an FTIR spectrometer is an optical device that is called the interferometer. The objective of the interferometer is to split the beam of radiation into two beams by using a beamsplitter. The most common interferometer is the Michelson interferometer[47]. The two light beams will travel two different paths and then they are recombined to form a single beam leaving the interferometer.

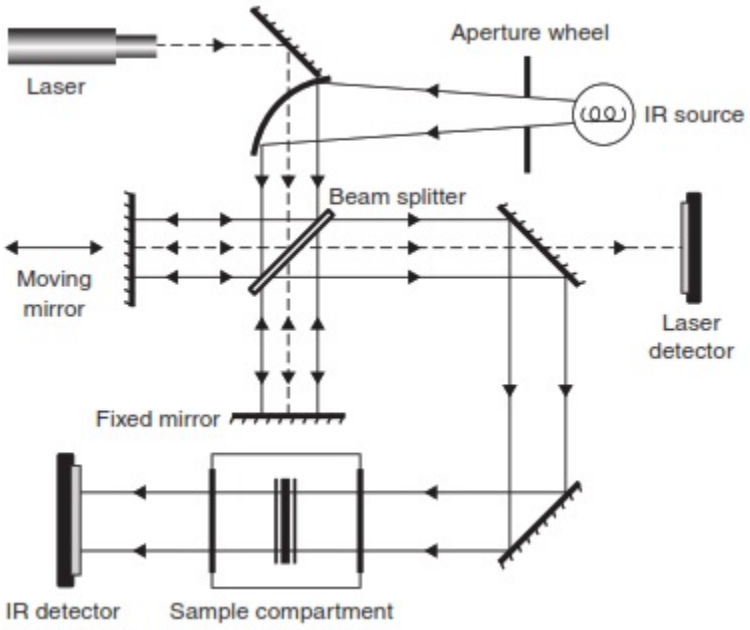

Figure 2.4: Typical FTIR spectrometer configuration[48]

The signal leaving the interferometer is the result of interfering of the two beams leading to the formation of an interferogram, which is a plot of light intensity versus optical path difference. The resulting interferograms are measured by scanning and are then Fourier transformed to produce a spectrum[47]. It is necessary to measure a background spectrum where there is no sample beam. This is done in order to a spectrum with features only related to the sample itself. A typical configuration of an FTIR spectrometer can be seen in Figure 2.4.

Attenuated total reflectance (ATR) is a type of sampling technique used in FTIR spectrometry. There are several crystal materials that are used with ATR such as zinc, silicon, and diamond[48]. The infrared beam will travel from the crystal, which has a high refractive index, to the sample that has a low refractive index. leading to reflection of part of the light back to the low refractive index[48]. At a certain angle, all the light waves are reflected back and this is referred to as total internal reflection. Some light energy escapes from the crystal to travel a small distance beyond the surface. The intensity of the reflected light decreases at this point and this is how attenuated total reflectance occurs[48]. The absorbed infrared radiation by the sample is then transformed into an infrared spectrum.

2.3.8 Soxhlet extraction

Soxhlet extraction is a conventional solid-liquid extraction experimental method that is used to extract certain compounds from a solid material. A Soxhlet setup is mainly composed of a round bottom flask, a Soxhlet extractor, and a reflux condenser. The solid sample is placed in a thimble holder that is made from filter paper, and the thimble

holder is then placed in the thimble chamber of the Soxhlet extractor. The solvent used for extraction, which is placed in the round bottom flask, is heated and it vaporizes into the thimble inside the Soxhlet extractor. After that, the liquid solvent is condensed and drips in the Soxhlet extractor until it reaches the siphon arm of the Soxhlet extractor. Once the liquid reaches the siphon arm, the solvent returns back to the round bottom flask along with the extracted compounds. According to Castro and Ayuso, the advantages of Soxhlet extraction are emphasized in the maintained high temperature of the setup and the continuous contact of fresh solvent with the sample in the thimble holder[49]. However, Soxhlet extraction needs a long time for the extraction to occur and there is a possibility of thermal decomposition of the extracted compounds due to continuous heating of the setup[49]. Soxhlet extraction has been in done in this project by using dichloromethane, which has a boiling point of 39.6°C, as an attempt to extract carbonaceous species.

3 Materials and methods

3.1 Materials

All the tested samples were provided by Elkem Silicon Materials. Two of the samples are old samples that were collected from the fluidized bed reactor in the year of 2015. Those two samples will be denoted from here on as MCS400 and MCS325. MCS400 and MCS325 are both a mixture of contact mass that have been collected from the fluidized bed reactor but at different reactor conditions. MCS400 was operated at a process temperature of 400°C while MCS325 was operated at a process temperature of 325°C. Another two samples were obtained in the year of 2018 and from here on will be denoted as MCS300 and MCS-Cu. MCS300 is a mixture of contact mass that was operated at a process temperature of 300°C and it was used for a long time in the reactor. MCS-Cu is not a mixture of contact mass which makes it a special sample. MCS-Cu is the result of CH_3Cl reacting on pure copper surface in the absence of silicon solids. This sample was obtained from different parts of the reactor, and it has been partly characterized in the catalysis specialization project TKP4580 in the fall semester of 2018. Copper catalyst has been introduced to the contact mass in the form of copper(I) chloride. In addition to those four samples, a sample of pure solid silicon denoted as SIL has also been characterized in order to be used as a reference.

3.2 Thermogravimetric analysis

Samples typically weighing in the range of 10-20 milligrams were placed in an alumina crucible and suspended into the microbalance of the instrument. An empty reference pan is also situated in the instrument. Experiments were done by the utilization of a Netzch STA 449C Jupiter TGA/DSC instrument which was connected to a Netzsch Aerlos QMS 403C MS to perform the mass spectrometry of the compounds evolving from the sample. Experiments were done in two different atmospheres by the use of two different gases: an oxidizing atmosphere with a controlled gas flow of 25 ml/min of pure argon and 55 ml/min of synthetic air (containing 20% O_2), and an inert atmosphere with a controlled gas flow of 80ml/min of pure argon. Argon is always employed as the protective line and the purge line is chose to be either synthetic air or argon.

The main masses that are expected to be detected in the mass spectrometry are the masses of CO_2 (44 g/mole) and H_2O (18 g/mole). Additional masses that were also looked for are Cu_2O (143.09 g/mole), CuCl (99 g/mole), CH_3Cl (50.49 g/mole), CH_4 (16 g/mole), CuO (79.54 g/mole), HCl (36.46 g/mole), $CuCl_2$ (134.45 g/mole), Cl_2 (70.91 g/mole).

O_2 (32 g/mole) and CO (28 g/mole) were also looked for but only in the case of inert atmosphere. This has been done through the creation of a parameter file in the Aëolos software to scan single masses. As for the TGA/DSC instrument software, two different correction files were created before conducting measurements in order to standardize a temperature program for each experimental atmosphere.

The only difference between both correction files is the gas that is selected as a purge line (synthetic air or argon). Creation of correction files was done by placing an empty crucible in the tool and setting the temperature program to be between 35°C and 800°C. Once 800°C is reached, the program is set to have an isothermal period at 800°C for one hour. The temperature increase has been set to a value of 10°C/min. After running experiments, used crucibles were placed in hydrochloric acid solution and left overnight in a fume hood to be cleaned. Following that, they were flushed with distilled water and acetone and then placed in a drying oven at a temperature of 100°C. A graphical representation of the instrument setup can be seen in Figure 3.1.

1. Computer + Software
2. Netzsch OU851.08 power unit
3. Julabo F257MC water bath
4. DCU Pfeiffer vacuum controller
5. Netzsch TASC 41474 controller
6. Netzsch temperature controller
7. Netzsch STA 449C Jupiter TGA/DSC
8. Netzsch Aërlos QMS 403C MS
9. Netzsch vacuum pump
10. Pfeiffer turbo pump

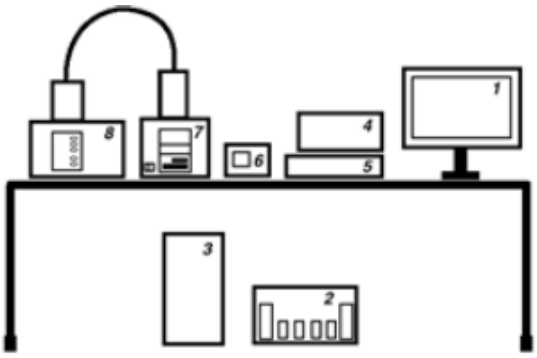

Figure 3.1: Setup of the thermal gravimetric/mass spectrometer instruments used

3.3 Pyrolysis-Gas chromatography

Samples weighing in the range of 0.1-0.5 milligrams were placed in small stainless steel cups. The sample cups are in turn placed in an autoshot sampler that injects the sample into the pyrolyzer. Pyrolysis was done by using a single-Shot Pyrolyzer "PY-3030S" from Frontier lab. The temperature used in the furnace for pyrolysis was chosen to be 500°C. Helium is used as the inert carrier gas at a flow of 2 mL/min, and a split ratio of 100:1 is employed. Products of pyrolysis are carried by the carrier gas to the capillary column in the Agilent 7820A gas chromatograph. The interface temperature between the pyrolyzer and chormatograph is maintained at 300°C and pressure of 1.5 bar. The column that is used in the chromatograph is an Ultra ALLOY$^+$ - 5 capillary column which has 5% diphenyldimetyl polysiloxane as the stationary phase. The length of the column is 30m, the diameter 0.25mm, and its thickness is 0.25µm. The initial temperature in the oven, where the column is placed, is held at 50°C for 2 minutes.

After that, a temperature ramp of 10°C occurs to reach a temperature of 200°C with 5 minutes of dwell time. Finally, another 10°C temperature ramp is done to reach 250°C and a dwell time of 5 minutes is also set. The different compounds are then directed towards the Agilent 5977 MSD mass spectrometer to be detected, and it is kept at a temperature of 300°C. The products were finally identified by matching with mass spectrometry data from the NIST library.

3.4 Raman spectroscopy

Raman spectra of the samples were measured by using a Horiba Jobin Yvon LabRAM HR800 spectrometer which is operated by through Labspec 6 software. The instrument was calibrated prior to measurements by using a Si sample. A x50LWD objective was used along with an internal standard Ne-Ne laser (633nm-visible). Scanning was operated continuously in the range of 200-2000cm^{-1}. The instrument was set to have a grating of 600 gr/mm, an acquisition time of 15s, an accumulation value of 3, a hole value of 200μm, and the laser had a 50% filter applied to it. The spectrometry system gives ultra high spectroscopic resolution and a unique wavelength range capability.

3.5 Scanning electron microscopy

Scanning electron microscopy was done by using a SEM Apreo instrument that is placed in a cleanroom. A conductive copper tape is sticked on the sample holder and the sample is placed on the tape. Nitrogen is used to remove particles that did not stick on the tape in order to avoid contamination of the instrument. The instrument operates in vacuum conditions and utilizes a Schottky-emission electron gun. Everhart-Thornley detector (ETD) was used in order to detect the scattered secondary electrons. A voltage of 20-30kV was applied on the samples along with a current of 0.80nA. Experiments were done in a standard operational mode that is ideal for navigating and imaging at low magnifications. Energy-dispersive X-ray spectroscopy (EDS) was done by using an EDX Oxford detector in order to obtain elemental analysis of the samples. The main chamber of the instrument is displayed in Figure 3.2.

3.6 X-ray diffraction

Powder X-ray diffraction was conducted on the samples in a D8 Focus DaVinci X-ray Diffractometer. Cu Kα radiation is utilized in Bragg-Brentano geometry to examine the composition and crystallinity of the samples. A continuous scan was recorded in the 2θ range of 15°-80°with a step size of 0.014°with a time of 0.33s per step and the sample is placed in a standard sample holder. The total scan time per sample is 26 minutes.

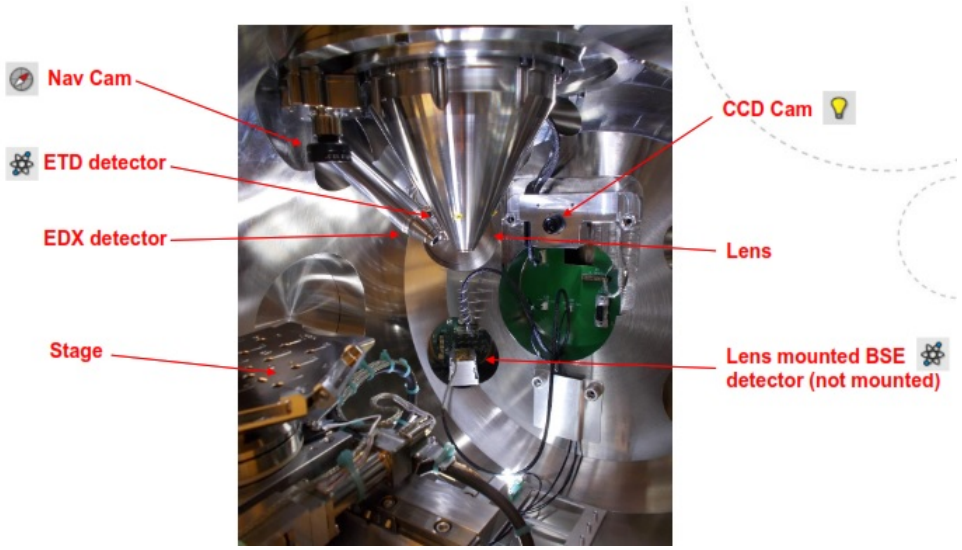

Figure 3.2: Main parts inside the SEM Apreo chamber

A divergence slit of 1mm is used and the wavelength is 1.54060Å. At the end of the experiments, the obtained diffractograms are searched and matched with data from PDF-4+ database by using the Bruker AXS DIFFRACT.EVA software.

3.7 Soxhlet extraction

Two different experiments were done in Soxhlet extraction with different parameters. For MCS400, 3 grams of the sample were weighed and placed in a cellulose filter paper that was shaped as a thimble. The thimble was then placed in the Soxhlet extraction setup. This was followed by addition of 100ml of dichloromethane from the top of the assembly. The dichloromethane flows down to the 250ml round bottom flask and the cold water flow through the condenser is initiated. The cold water flow enters the condenser from the bottom inlet and leaves from the upper outlet. Heating is then initiated to reach the boiling point of dichloromethane and the condensation of the evolved vapors occurs leading to the filling of the extractor until the solvent siphons back to the round bottom flask along with the extracted compounds. This process was operated continuously for 24 hours. In case the solvent level was going low in the flask, extra dichloromethane was added to the system from the top.

Soxhlet extraction of MCS-Cu was done before MCS400, and the initial mass of the sample was 1.7 grams. 50ml of dichloromethane were added initially and the heating was continuously done for 6 hours only. A representation of the experimental setup used can be seen in Figure 3.3.

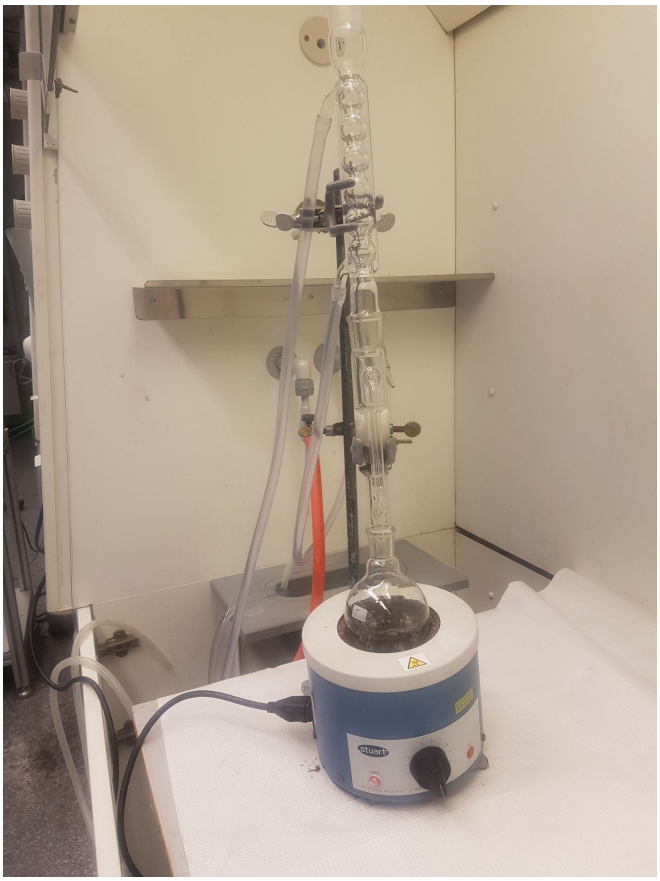

Figure 3.3: Soxhlet extraction setup with the thimble placed in the extractor. Cold water flow comes into the system from the bottom inlet and leaves from the upper outlet of the condenser

3.8 Attenuated total reflection Fourier transform-infrared spectroscopy

After the extraction has been done, the extract was then examined by a Nicolet iS50 device for the Fourier transform-infrared (FTIR) spectroscopy using attenuated total reflection (ATR) mode. The transmittance was calculated according to background in atmosphere, and the resolution used is 4 cm^{-1}. A KBr beampslitter is employed in the instrument and 32 scans per spectra were collected. The FTIR spectroscopy was done within the wavenumber range of 400-4000 cm^{-1}. Continuous dropping of the extract on the ATR crystal was done since the solution quickly evaporated due to the heat emitted from the crystal.

4 Results

4.1 Thermogravimetric analysis/mass spectrometry

4.1.1 Oxidizing atmosphere

In addition to the four samples, pure silicon has also been studied in oxidizing atmosphere after it has been dried. The results for pure silicon sample, SIL, are shown in the appendix.

The change in mass and heat exchange of MCS400 were measured as a function of time and temperature and are displayed in Figures 4.1-4.2. CO_2, CH_4, CH_3Cl, and H_2O are the compounds that are detected by the mass spectrometer as shown in Figure 4.3. The sample mass that is placed in the crucible is 15.74mg. A total mass loss of approximately 37% is seen in the results which accounts for 5.82mg. An initial minor mass loss is seen in an early period of the experiment that could be accredited to the drying of the sample. The major mass loss that is witnessed is in the range between 283°C (25th minute) and 530°C (50th minute). The DSC signal shows a sharp exothermic peak around 436°C (40th minute).As for the masses detected by the mass spectrometer, CO_2 and CH_4 signal peaks are witnessed around 436°C (40th minute). Those peaks correlate well with the major mass loss and the sharp exothermic peak that are occurring in that period of the experiment. In addition, CH_3Cl signal peak appears at 340 °C (30th minute) which is also in the period of mass loss. As for H_2O, two small peaks appear at approximately 331°C (30th minute) and 430°C (40th minute).

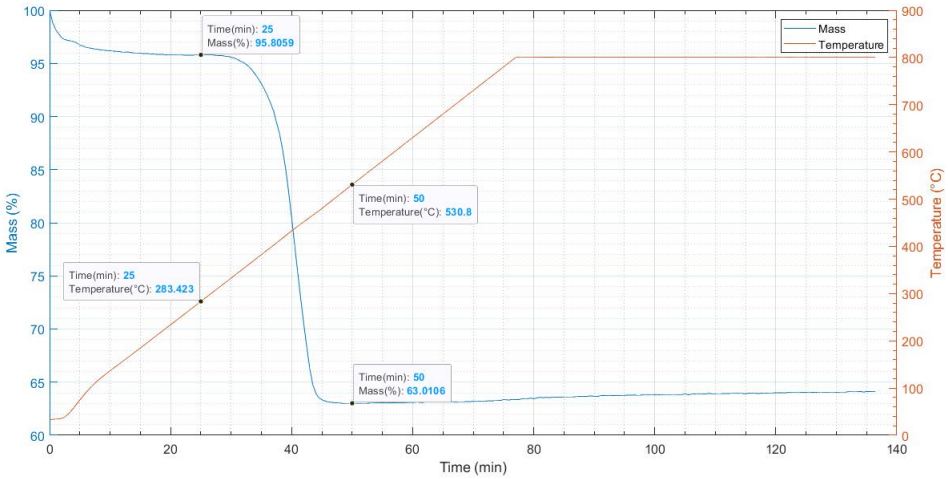

Figure 4.1: Mass change as a function of temperature and time in MCS400. Initial mass of sample is 15.74mg

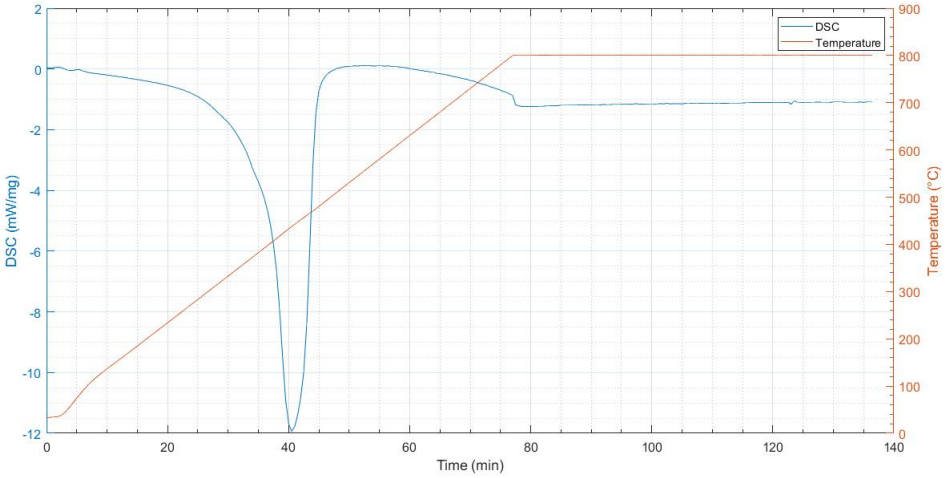

Figure 4.2: DSC signal as a function of temperature and time in MCS400

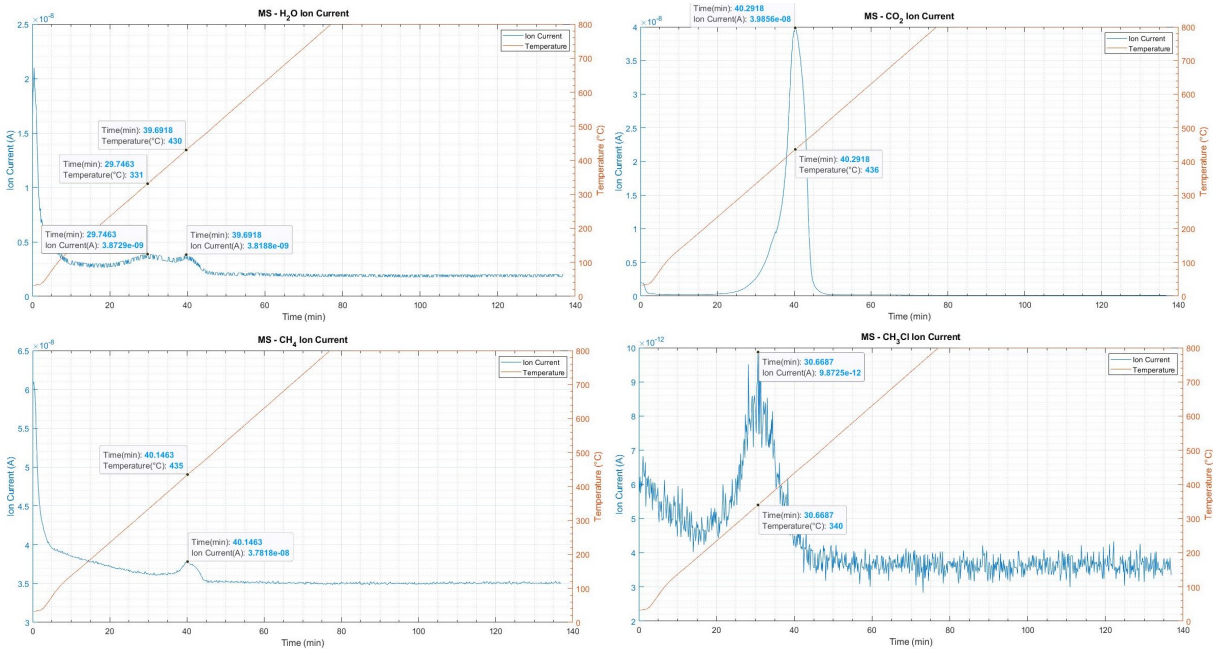

Figure 4.3: Detected compounds in mass spectrometry of MCS400

The change in mass and heat exchange of MCS325 were measured as a function of time and temperature and are displayed in Figures 4.4-4.5. CO_2, CH_3Cl, and H_2O are the compounds that are detected by the mass spectrometer as shown in Figure 4.6. The sample mass that is placed in the crucible is 16.14mg. A total mass loss of approximately 2.6% is seen in the results which accounts for 0.42mg. For this sample, the major mass loss that occurs is in the early period of experiment up till 104°C (7th minute) which could be accredited to drying of the sample. A minor mass loss occurs in the temperature range between 104°C (7th minute) and 516°C (48.5 minutes). Beyond that point, the sample seems to be gaining mass which might be due to the oxidation of silicon. The DSC signal shows three different endothermic peaks. Two peaks are at an early stage of the experiment, and the third peak, which is the largest, comes at around 630°C (60th minute).

As for the masses detected by the mass spectrometer, CO_2 signal peak was witnessed at approximately 321°C (29th minute). CH_3Cl signal peak appears at approximately 333°C (30 minutes). Both CO_2 and CH_3Cl peaks are present in the period of minor mass loss. H_2O signal is seen in an early period of the experiment.

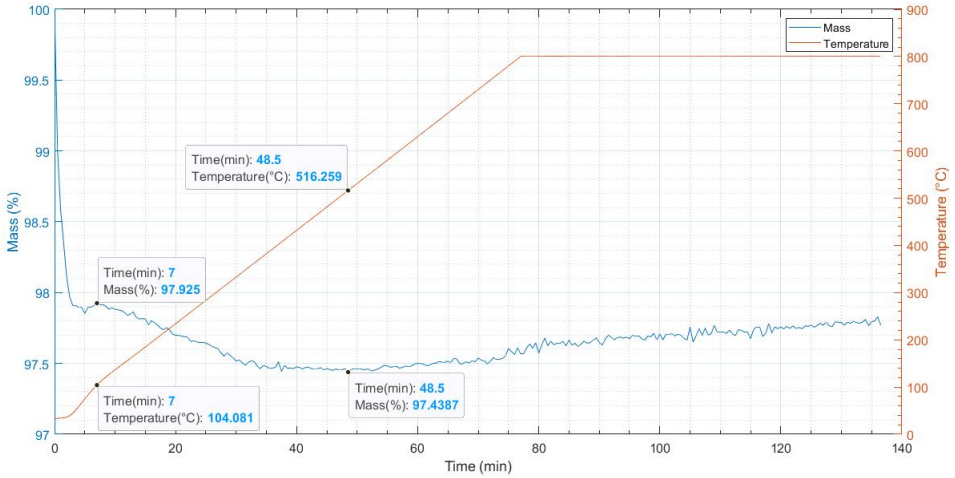

Figure 4.4: Mass change as a function of temperature and time in MCS325. Initial mass of sample is 16.14mg

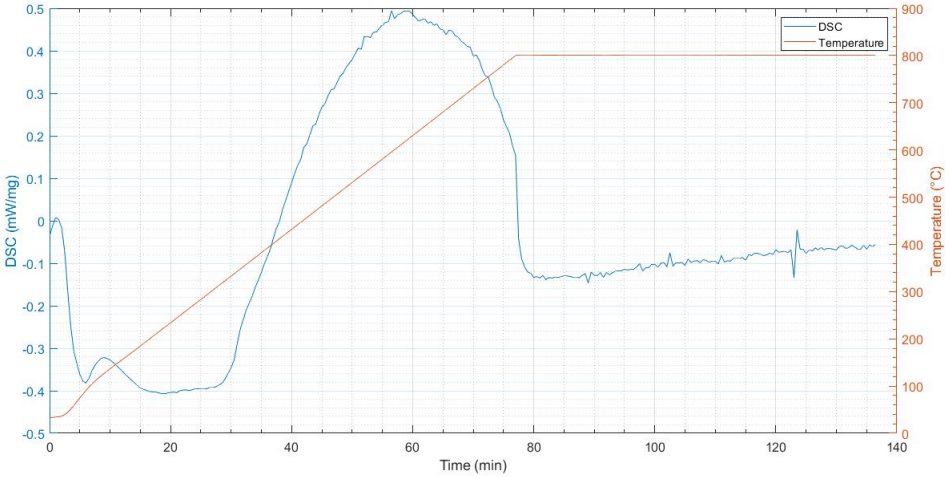

Figure 4.5: DSC signal as a function of temperature and time in MCS325

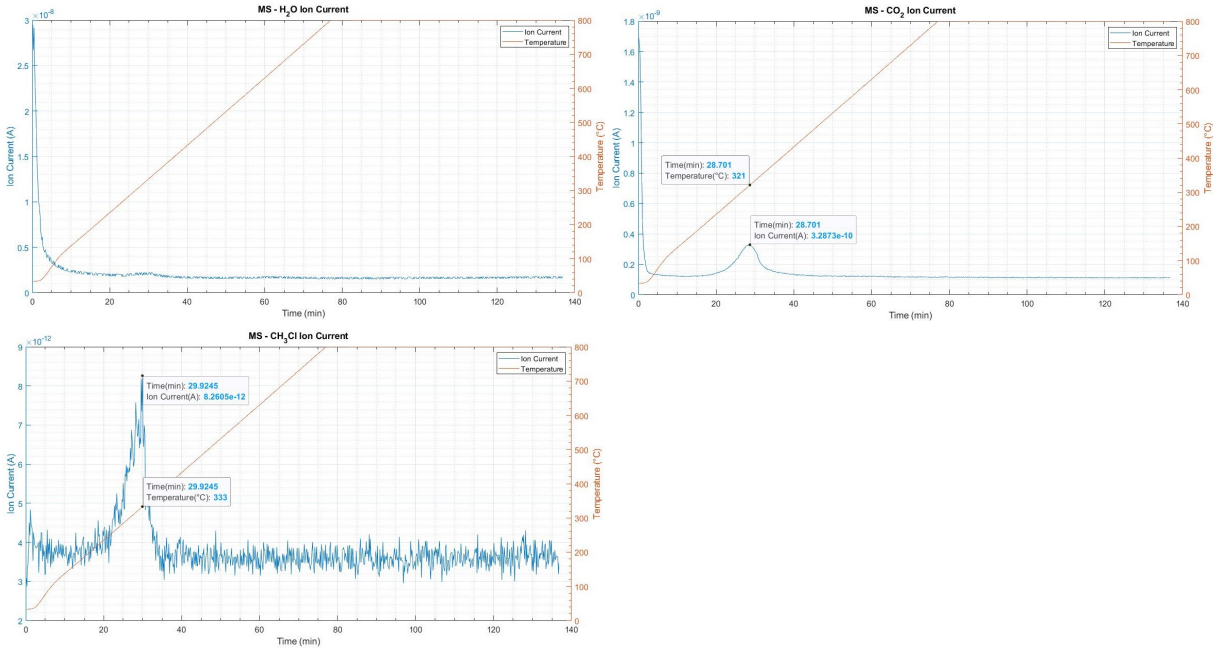

Figure 4.6: Detected compounds in mass spectrometry of MCS325

The change in mass and heat exchange of MCS300 were measured as a function of time and temperature and are displayed in Figures 4.7-4.8. CO_2, CH_3Cl, and H_2O are the compounds that are detected by the mass spectrometer as shown in Figure 4.9. The sample mass that is placed in the crucible is 16.58mg. A total mass loss of approximately 2.2% is seen in the results which accounts for 0.36mg. Similar to MCS325, the major mass loss that occurs is in the early period of experiment up till 104°C (7th minute) which could be accredited to drying of the sample. A minor mass loss occurs between 104°C (7th minute) and 476°C (44.5 minutes). Beyond that point, the sample seems to be slightly gaining mass which might be due to the oxidation of silicon. The DSC signal shows three different endothermic peaks. The heat exchange profile is also highly similar to that of MCS325. Two peaks are at an early stage of the experiment, and the third peak, which is the largest, comes at around 630°C (60th minute).

As for the masses detected by the mass spectrometer, CO_2 signal peak was witnessed at approximately 322°C (29th minute). CH_3Cl signal peak appears at approximately 334°C (30 minutes). Both CO_2 and CH_3Cl peaks are present in the period of minor mass loss. H_2O signal is seen in an early period of the experiment. The mass spectrometry shows almost identical signals to those obtained from MCS325.

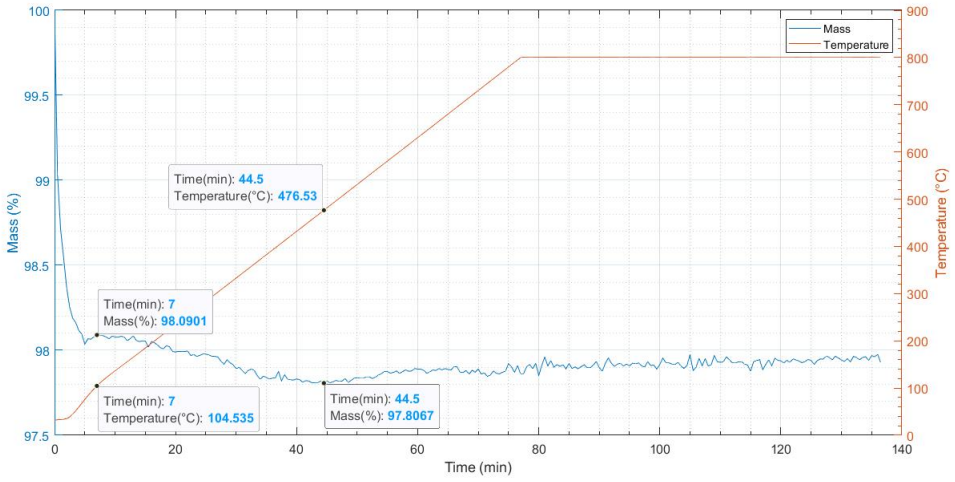

Figure 4.7: Mass change as a function of temperature and time in MCS300. Initial mass of sample is 16.58mg

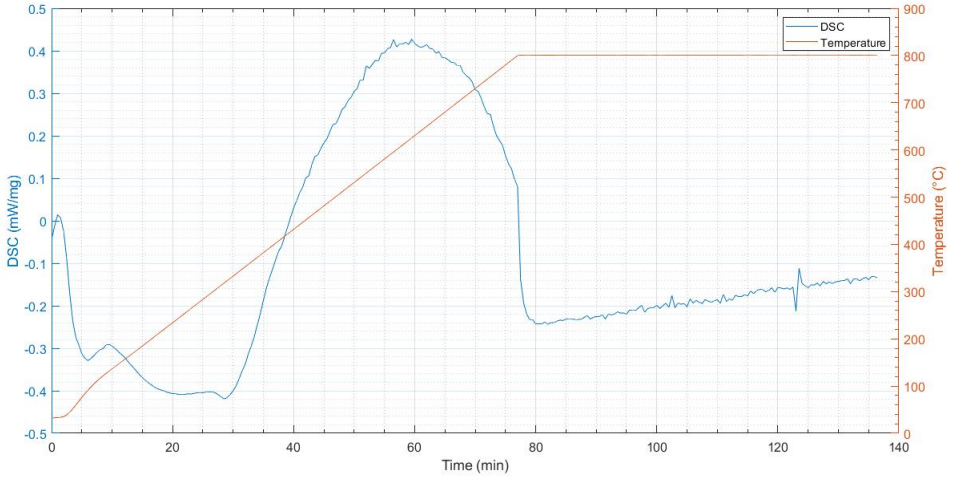

Figure 4.8: DSC signal as a function of temperature and time in MCS300.

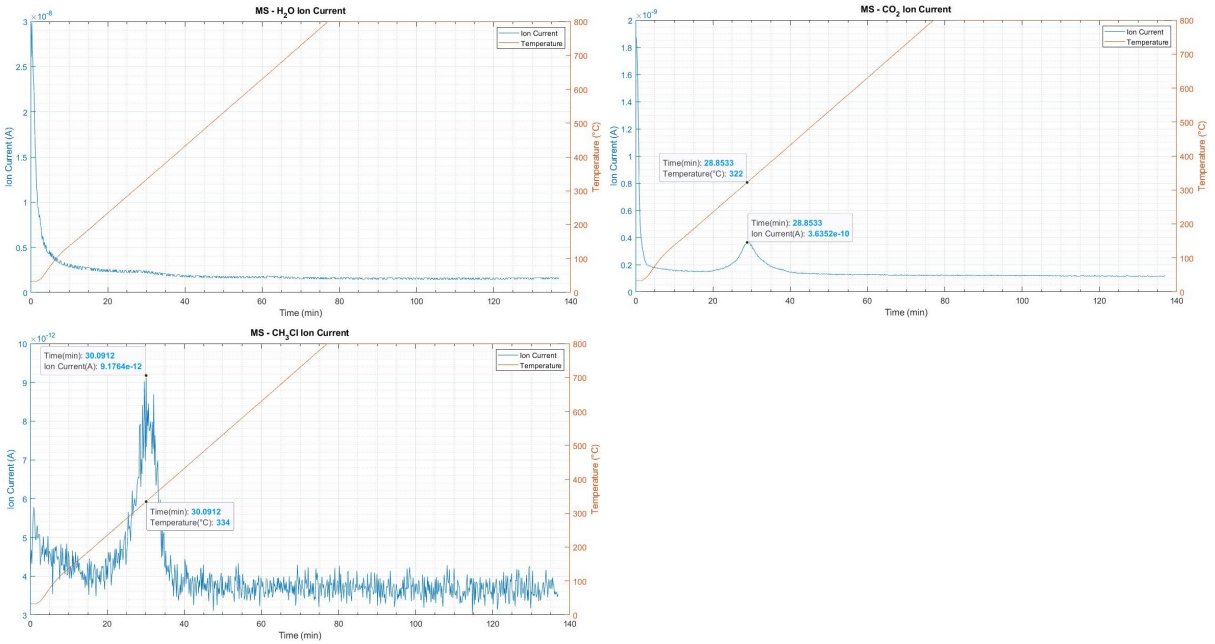

Figure 4.9: Detected compounds in mass spectrometry of MCS300

The change in mass and heat exchange of MCS-Cu were measured as a function of time and temperature and are displayed in Figures 4.10-4.11. CO_2, CH_3Cl, Cl_2, and H_2O are the compounds that are detected by the mass spectrometer as shown in Figure 4.12. The sample mass that is placed in the crucible is 18.13mg. A total mass loss of approximately 61.4% is seen in the results which accounts for 11.13mg. In the early period of the experiment, a minor mass loss occurs and this is probably due to drying of the sample. This minor mass loss is followed by a slight mass gain right before the major mass loss starts. The major mass loss occurs between 411°C (38th minute) and 780 °C (75th minute). The DSC signal shows two exothermic peaks that appear at approximately 372°C (34th minute) and 456 °C (42.5th minute). There are also two major endothermic peaks that are witnessed. One peak at 416 °C (38.5th minute) and another at 630 °C (60th minute).

As for the masses detected by the mass spectrometer, CO_2 showed three signal peaks which are witnessed around 378°C (34.5 minutes), 460°C (42.7 minutes), and the smallest magnitude peak at 741 °C (71 minutes). The CO_2 peak at 378°C appears before the major mass loss period, while the other two peaks occur during the major mass loss period. H_2O shows a small peak at 235°C (20th minute), and CH_3Cl shows a peak at 264 °C (22.9 minutes). Both H_2O and CH_3Cl signal peaks appear before the major mass loss period. In addition, Cl_2 was detected at 741°C (71.1 minutes) which is during the major mass loss period.

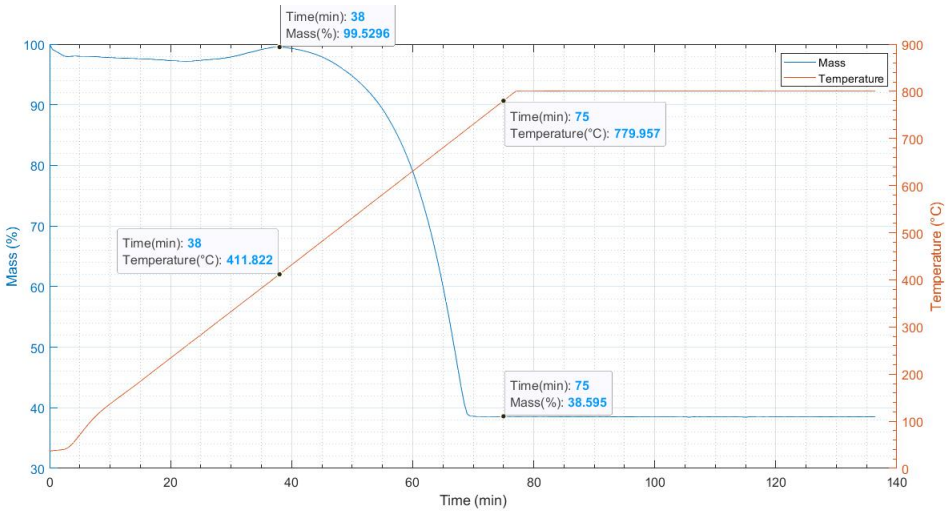

Figure 4.10: Mass change as a function of temperature and time in MCS-Cu. Initial mass of sample is 18.13mg.

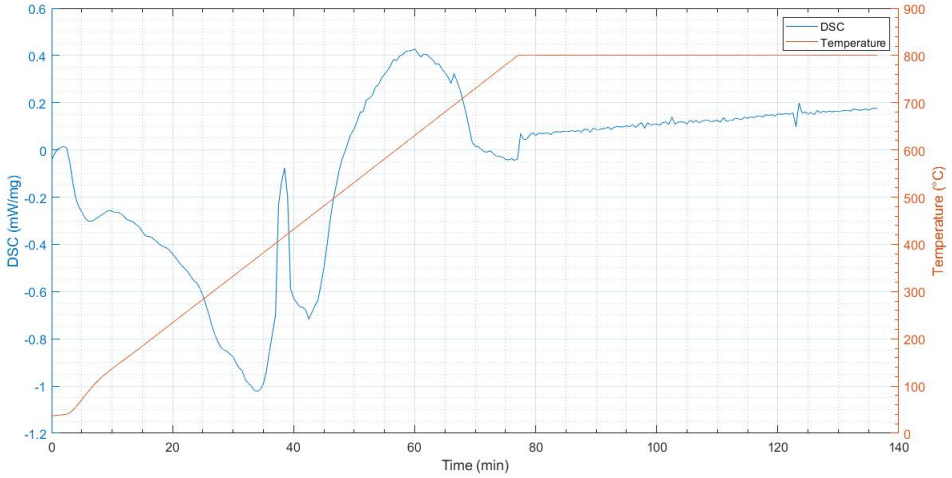

Figure 4.11: DSC signal as a function of temperature and time in MCS-Cu

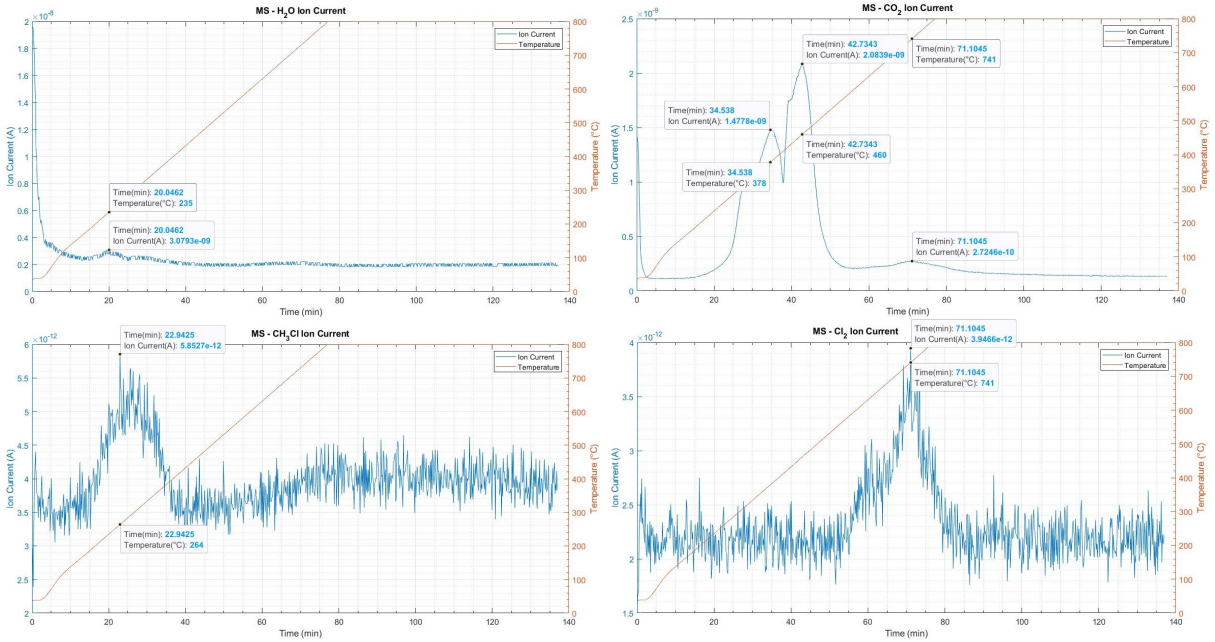

Figure 4.12: Detected compounds in mass spectrometry of MCS-Cu

4.1.2 Inert atmosphere

Changes in mass and the heat exchange of MCS400 were measured as a function of time and temperature in an inert atmosphere (80ml/min argon flow) and they are displayed in Figures 4.13-4.14. CO_2, CH_4, CH_3Cl, and H_2O were also detected in mass spectrometry in case of inert atmosphere and they are shown in Figure 4.15. Initial sample mass placed in the crucible is 14.80mg. Total mass loss of approximately 10% was witnessed which accounts for 1.48mg of the initial mass. Fast initial mass loss of approximately 3.6% is seen when the experiment starts and up to 38.7°C (2.5 minutes) that could be accredited to drying and then the mass kept on decreasing linearly even at isothermal time. The mass spectra of CO_2 showed three different signal peaks with the first being at 328°C (29.5 minutes), the second at 615°C (58.4 minutes), and the third at 800°C (77.3 minutes).CH_4 showed a single peak at 586°C (55.5 minutes) and CH_3Cl also showed a single peak at 610°C (57.8 minutes). As for H_2O, an initial peak was seen at 76°C (5 minutes) and then two broad peaks appear at 652°C (62.2 minutes) and at 800°C (77.3 minutes).

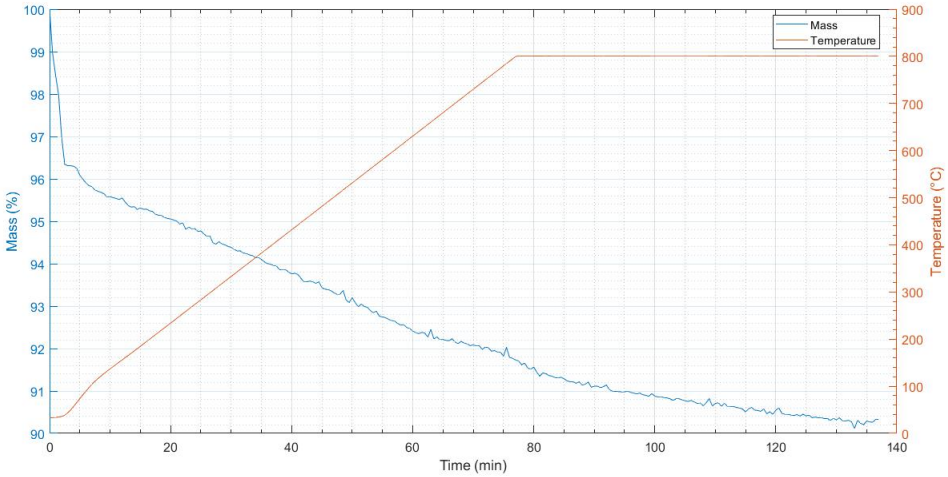

Figure 4.13: Mass change as a function of temperature and time in MCS400 in inert atmosphere. Initial mass of sample is 14.80mg.

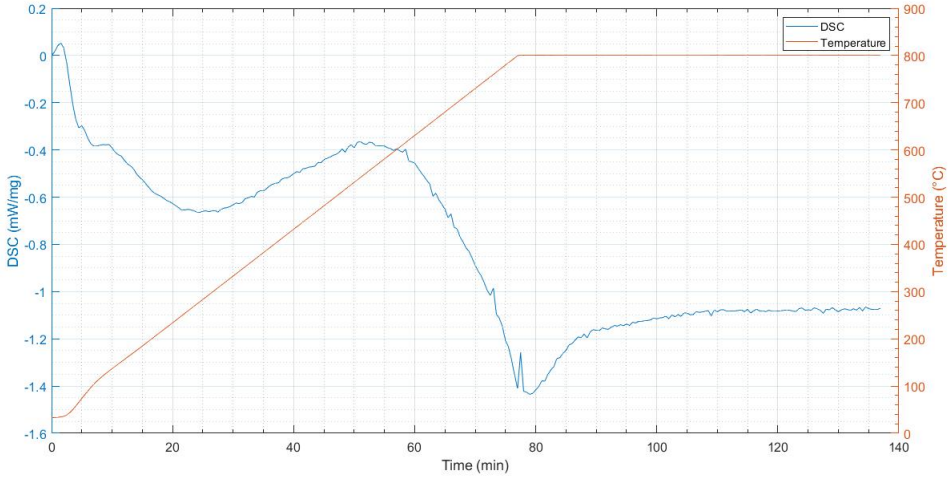

Figure 4.14: DSC signal as a function of temperature and time in MCS400 in inert atmosphere

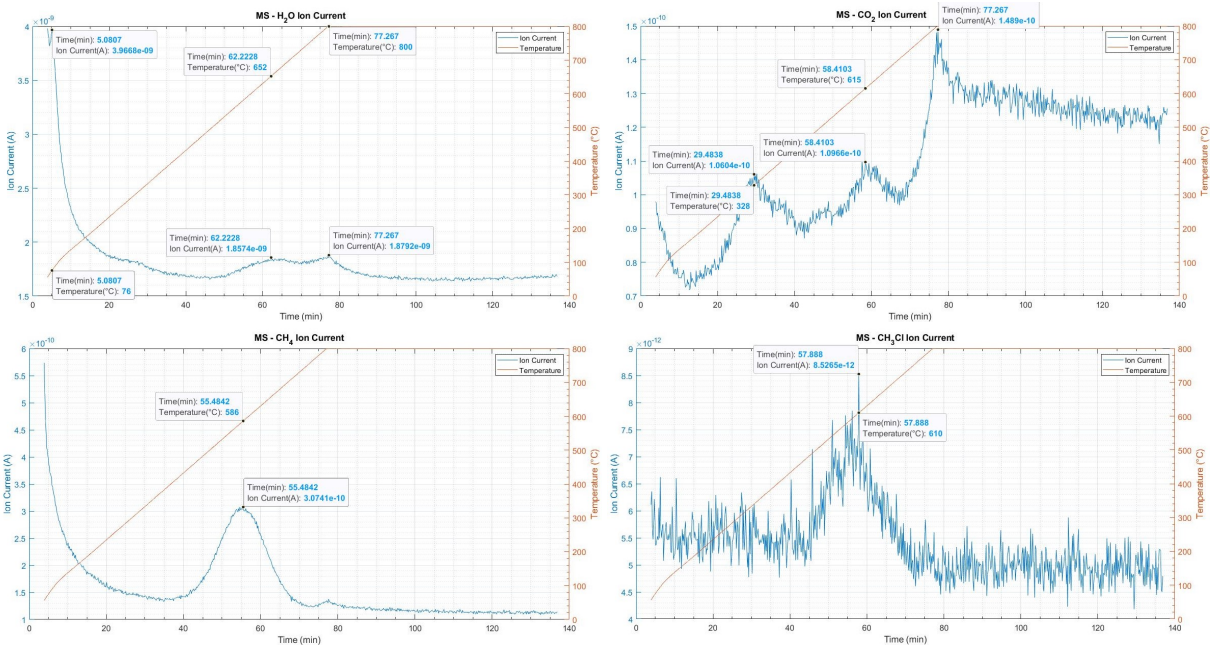

Figure 4.15: Detected compounds in mass spectrometry of MCS400 in inert atmosphere

Changes in mass and the heat exchange of MCS325 were measured as a function of time and temperature in an inert atmosphere (80ml/min argon flow) and they are displayed in Figures 4.16-4.17. CO_2 and H_2O were the only compounds to be detected by mass spectrometry in case of inert atmosphere and their mass spectra are shown in Figure 4.18. Initial sample mass in the crucible is 17.43mg. A total mass of approximately 3% is seen in the results which accounts for 0.52mg. Most of the mass loss occurs in the start up of the experiment up to 38°C (2.5 minutes) where the mass drops down to 97.2% and this could be related to drying of the sample. After that a slight mass gain is seen followed by a mass loss down to 97%.

The mass spectra of CO_2 showed a broad peak that is centered around 562°C (53.2 minutes). H_2O also showed a broad peak that is centered at 547°C (51.6 minutes).

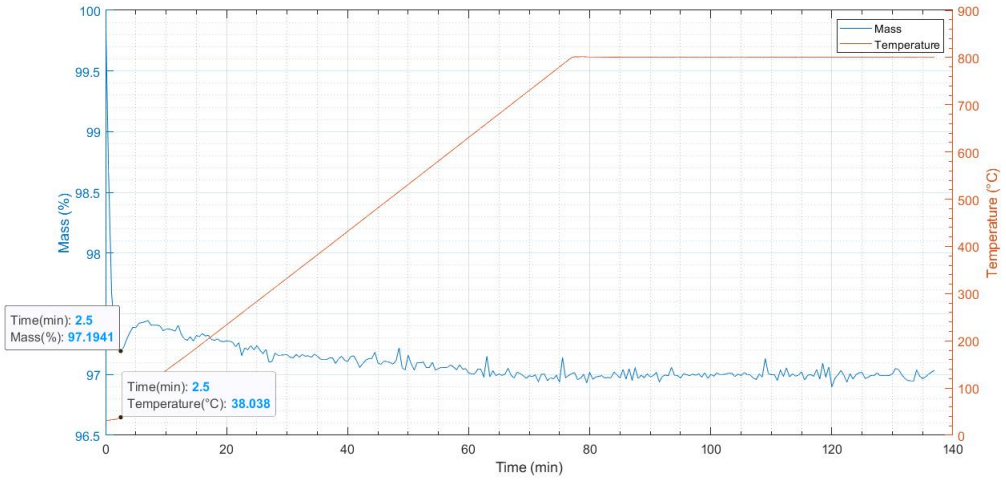

Figure 4.16: Mass change as a function of temperature and time in MCS325 in inert atmosphere. Initial mass of sample is 17.43mg

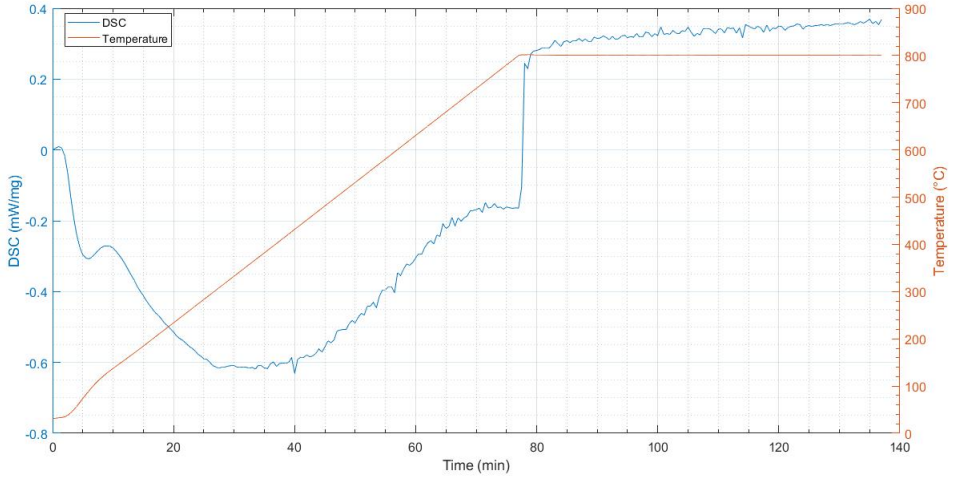

Figure 4.17: DSC signal as a function of temperature and time in MCS325 in inert atmosphere

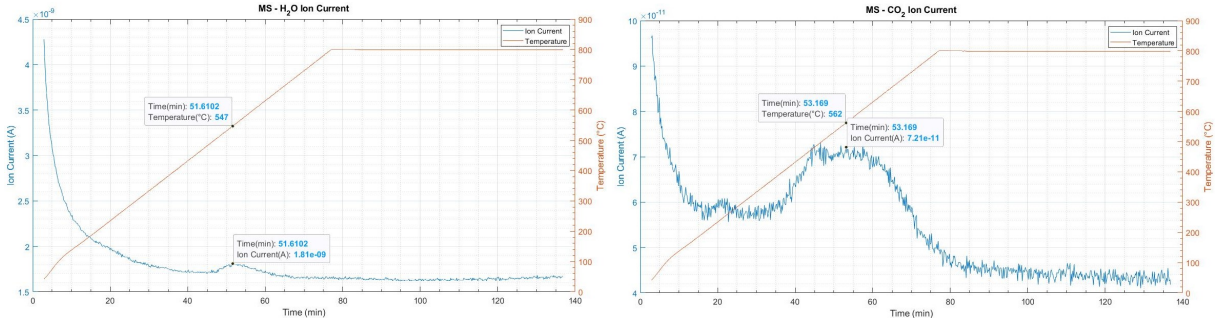

Figure 4.18: Detected compounds in mass spectrometry of MCS325 in inert atmosphere

Changes in mass and the heat exchange of MCS300 were measured as a function of time and temperature in an inert atmosphere (80ml/min argon flow) and they are displayed in Figures 4.19-4.20. CO_2 and H_2O were the only compounds to be detected by mass spectrometry in case of inert atmosphere and their mass spectra are shown in Figure 4.21.Initial mass of the sample in the crucible is 18.05mg. This sample showed similar mass loss behavior to MCS325 in inert atmosphere as well with a total mass loss of approximately 3.4% which accounts for 0.61mg. Also most of the mass loss occurs when the experiment starts and up to 38°C (2.5 minutes) where the mass drops down to 97.2% and this could be explained by drying of the sample. A slight mass gain was also witnessed and followed by mass loss down to approximately 96.6% of initial sample mass.

Mass spectra of CO_2 showed 3 signal peaks with the first being at 487°C (45.5 minutes), the second at 623°C (59.3 minutes), and the third at 792°C (76.2 minutes). As for H_2O, one broad signal peak was seen at 566°C (53.5 minutes).

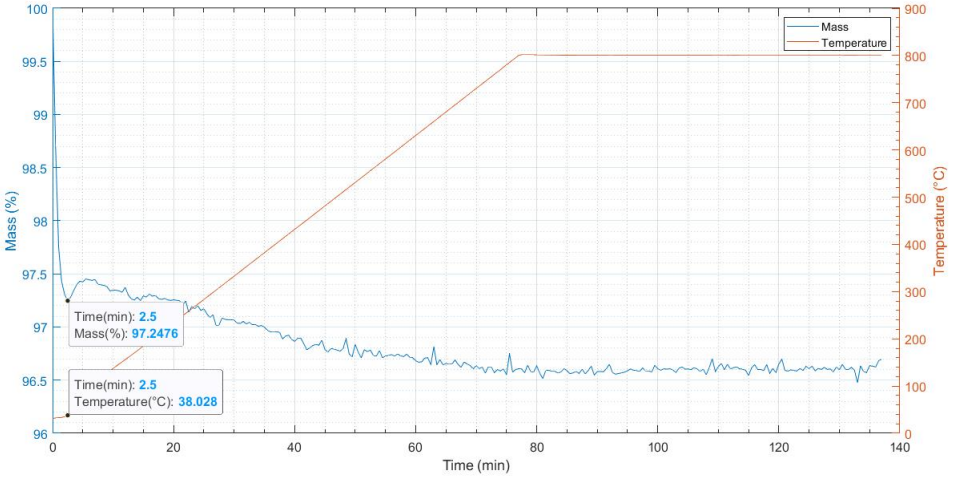

Figure 4.19: Mass change as a function of temperature and time in MCS300 in inert atmosphere. Initial mass of the sample is 18.05mg.

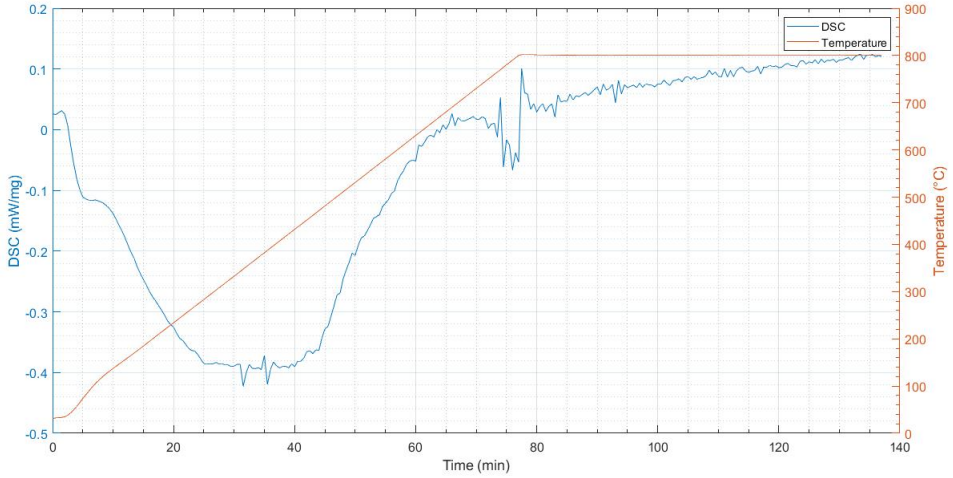

Figure 4.20: DSC signal as a function of temperature and time in MCS300 in inert atmosphere

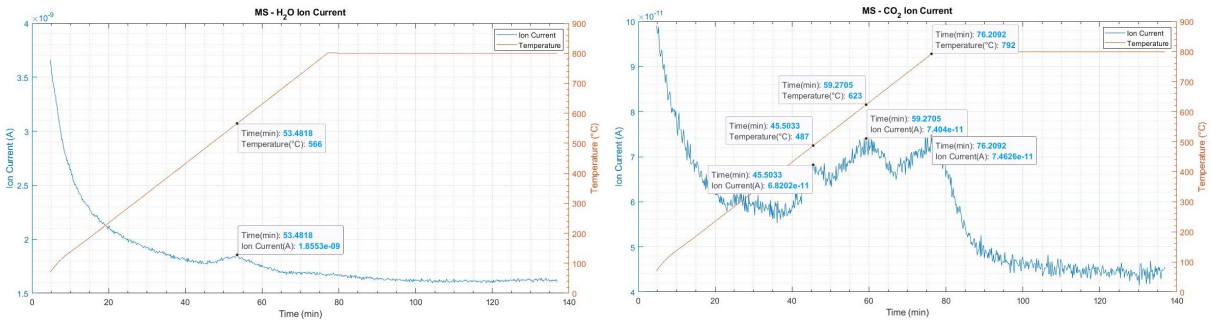

Figure 4.21: Detected compounds in mass spectrometry of MCS300 in inert atmosphere

Changes in mass and the heat exchange of MCS-Cu were measured as a function of time and temperature in an inert atmosphere (80ml/min argon flow) and they are displayed in Figures 4.22-4.23. CO_2,H_2O, and CH_4 were the only compounds to be detected by mass spectrometry in case of inert atmosphere and they are shown in Figure 4.24. Initial mass of the sample in the crucible is 17.48mg. Total mass loss of approximately 74.7% is seen in the results which accounts for 13.06mg of mass loss. A minor mass loss of approximately 5.55% occurs in the early period of the experiment up till 431°C (40th minute). The major mass loss occurs between the 431°C and 779.9°C (75th minute) where the percentage of mass drops down to 25.9%. The mass of the sample decreases in a continuous minor manner after the major mass loss period.

Mass spectra of CO_2 showed two major signal peaks with the first being at 429°C (39.7 minutes) and the second at 724°C (69.5 minutes). As for H_2O, one major signal peak is seen at approximately 224°C (19 minutes). Finally, CH_4 showed two signal peaks with the first being at 231°C (19.6 minutes) and the second at approximately 429°C (39.7 minutes).

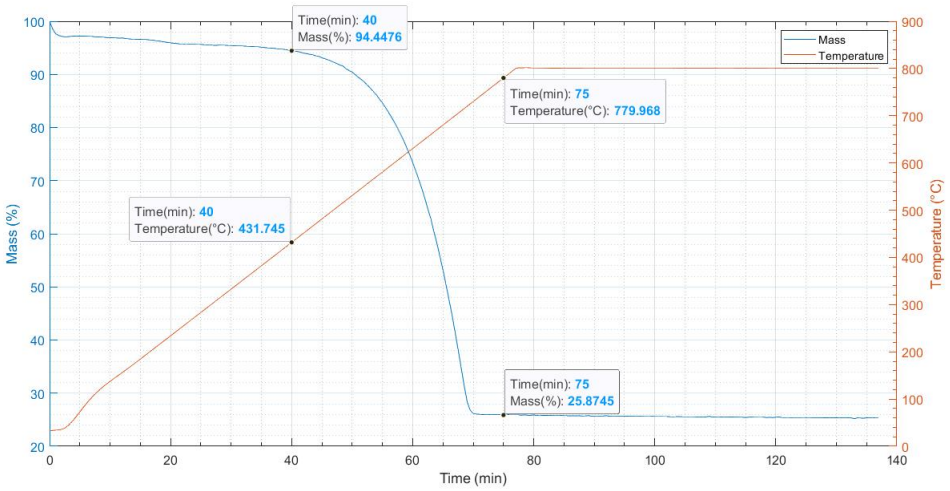

Figure 4.22: Mass change as a function of temperature and time in MCS-Cu in inert atmosphere. Initial mass of the sample is 17.48mg.

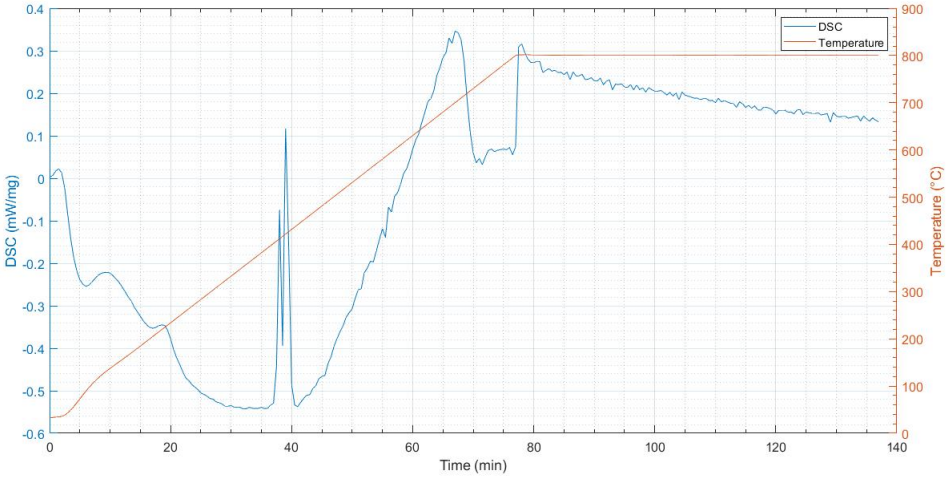

Figure 4.23: DSC signal as a function of temperature and time in MCS-Cu in inert atmosphere

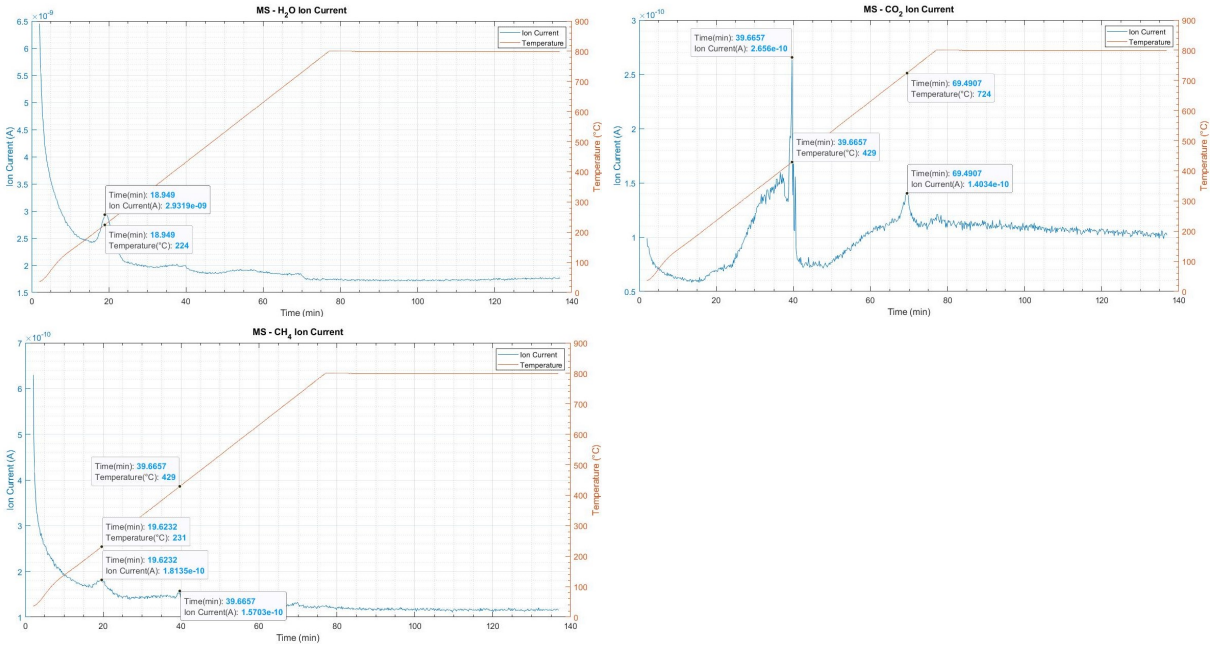

Figure 4.24: Detected compounds in mass spectrometry of MCS-Cu in inert atmosphere

4.2 Pyrolysis-gas chromatography/mass spectrometry

Mass spectra of the compounds that resulted from the pyrolysis-gas chromatography were collected and identified by using the NIST database library. Compounds to be considered in the results are the ones that had a match quality of 70 or higher according to the NIST database. Spectra of the detected compounds are plotted in terms of abundance of each compound versus experimental time. Values of retention time for each compound is pointed out on the top of their respective peaks.

4.2.1 MCS400

Mass spectra results of the detected compounds from sample MCS400 are shown in Figure 4.25. Detected compounds that will be taken into consideration according to quality are shown in Table 4.1. According to mass spectrometry results, the most abundant compound from pyrolysis-gas chromatography of MCS400 is carbon dioxide.

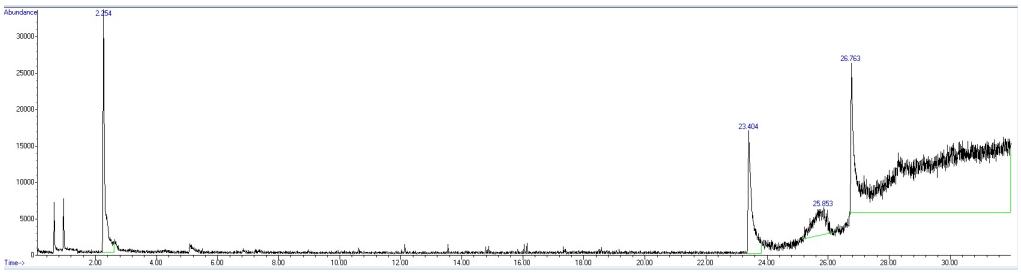

Figure 4.25: Mass spectra of detected compounds from MCS400

Table 4.1: Detected compounds by mass spectrometry from the pyrolysis-gas chromatography of sample MCS400

Detected compound	Retention time(min)	Abundance(a.u.)
Carbon dioxide	2.254	33374
n-Hexadecanoic acid	23.404	16863
Octadecanoic acid	26.763	20517

4.2.2 MCS325

Mass spectra results of the detected compounds from sample MCS325 are shown in Figure 4.26. Detected compounds that will be taken into consideration according to quality are shown in Table 4.2. According to mass spectrometry results, the most abundant compound from pyrolysis-gas chromatography of MCS325 is n-Hexadecanoic acid.

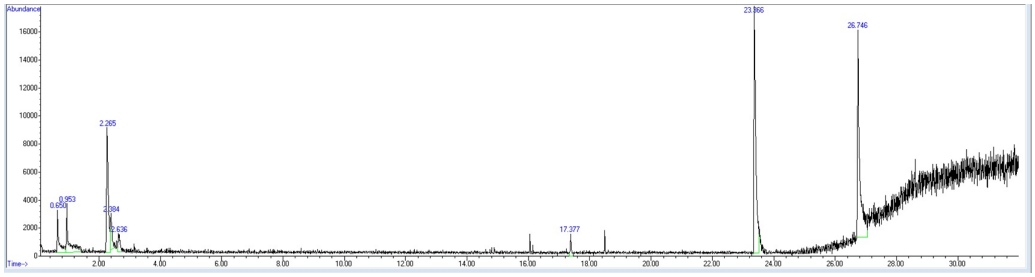

Figure 4.26: Mass spectra of detected compounds from MCS325

Table 4.2: Detected compounds by mass spectrometry from the pyrolysis-gas chromatography of sample MCS325

Detected compound	Retention time(min)	Abundance(a.u.)
Carbon dioxide	2.265	8909
n-Hexadecanoic acid	23.366	17606
Octadecanoic acid	26.746	14770

4.2.3 MCS300

Mass spectra results of the detected compounds from sample MCS300 are shown in Figure 4.27. Detected compounds that will be taken into consideration according to quality are shown in Table 4.3. According to mass spectrometry results, the most abundant compound from pyrolysis-gas chromatography of MCS300 is n-Hexadecanoic acid.

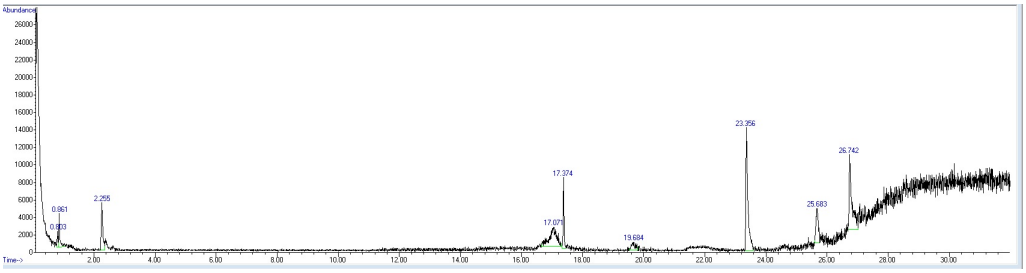

Figure 4.27: Mass spectra of detected compounds from MCS300

Table 4.3: Detected compounds by mass spectrometry from the pyrolysis-gas chromatography of sample MCS300

Detected compound	Retention time(min)	Abundance(a.u.)
Carbon dioxide	2.255	5395
Phthalic acid, 2-ethoxyethyl ethyl ester	17.374	8115
n-Hexadecanoic acid	23.356	14033
8-Methoxy-quinoline-5-sulfonic acid butylamide	25.683	3906
Octadecanoic acid	26.742	8559

4.2.4 MCS-Cu

Mass spectra results of the detected compounds from sample MCS-Cu are shown in Figure 4.28. Detected compounds that will be taken into consideration according to quality are shown in Table 4.4. According to mass spectrometry results, the most abundant compound from pyrolysis-gas chromatography of MCS-Cu is Octadecanoic acid.

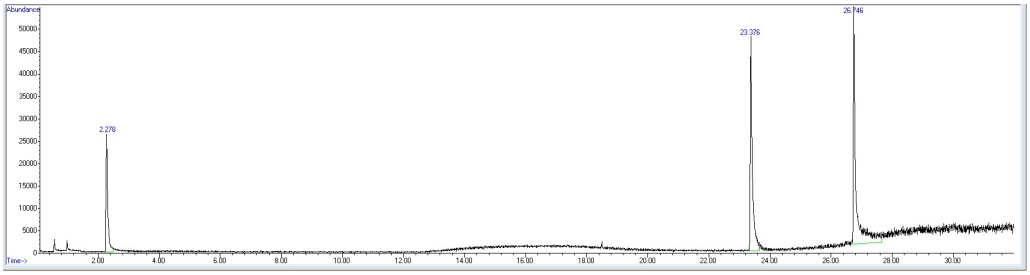

Figure 4.28: Mass spectra of detected compounds from MCS-Cu

Table 4.4: Detected compounds by mass spectrometry from the pyrolysis-gas chromatography of sample MCS-Cu

Detected compound	Retention time(min)	Abundance(a.u.)
Carbon dioxide	2.278	26316
n-Hexadecanoic acid	23.376	47840
Octadecanoic acid	26.746	52929

4.3 Surface morphology and elemental analysis

The morphology of all four samples has been studied by scanning electron micrscopy (SEM). This can help in observing the reaction pits from where methylchlorosilanes are formed and to witness the effect of reaction conditions on the contact mass. In addition, the morphology of the pure silicon sample, SIL, has been studied in order to be used as a reference. This is done in order to help compare unreacted silicon to contact masses that have been used for production of methylchlorosilanes. Furthermore, elemental analysis has been done by energy dispersive X-ray spectroscopy (EDS) to study the distribution of elements in the contact mass and in sample MCS-Cu.

The morphology of the pure silicon sample, SIL, is shown in Figures 4.29-4.30 for the same site with different magnifications.

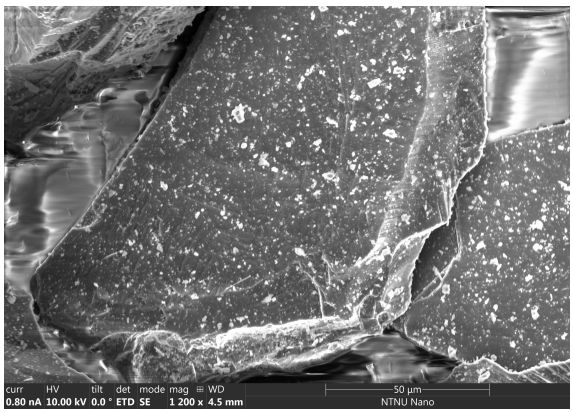

Figure 4.29: Surface morphology of pure silicon sample at 50µm magnification using a voltage of 10kV and a current of 0.80nA

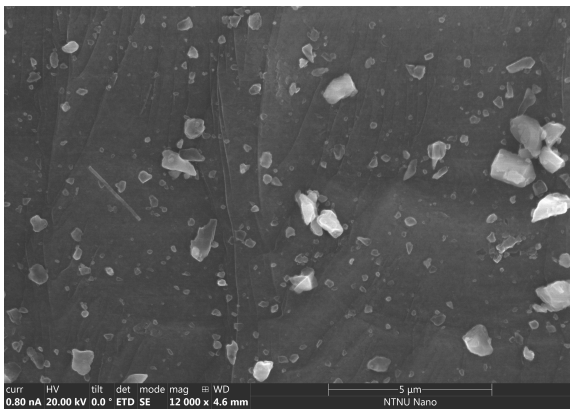

Figure 4.30: Surface morphology of pure silicon sample at 5µm magnification using a voltage of 20kV and a current of 0.80nA

Surface morphology of sample MCS400 has shown to be unique. This can be explained by the process temperature at which it was operated (400°C). This sample has shown heterogeneity in its surface morphology. Some sites were noticed to have reaction pits with fierce consumption of silicon. Such site is shown in Figures 4.31-4.32 with a magnification into the reaction pit. Elemental analysis of this site will be shown later in this section. Other sites with less fierce consumption of silicon were also seen and an example of such sites is shown in Figures 4.33-4.34 with different magnifications. Particles with such sites might have been added later in the process since fresh silicon is

added at specific intervals. Samples MCS325 and MCS300 showed somehow similar morphology. Reaction pits are developed in those samples due to the formation of methylchlorosilanes and consumption of the silicon particles. The consumption of silicon was not as fierce as it was seen in MCS400. Surface morphology of a site in MCS325 is seen in Figures 4.35-4.36 with a magnification on the reaction pits, and the morphology of a site in MCS300 is seen in Figures 4.37-4.38 also with a magnification on the reaction pits.

Figure 4.31: Surface morphology of MCS400 sample at 50µm magnification using a voltage of 20kV and a current of 0.80nA

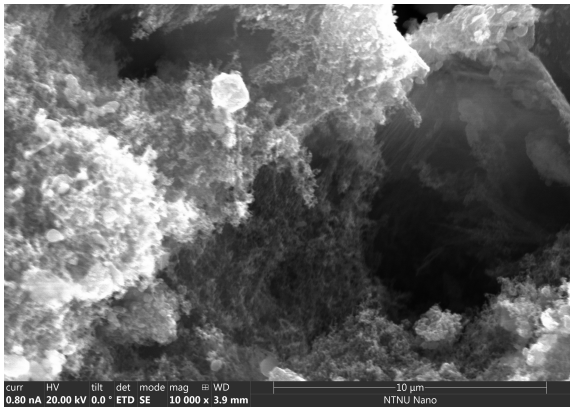

Figure 4.32: Surface morphology of MCS400 sample at 10µm magnification using a voltage of 20kV and a current of 0.80nA

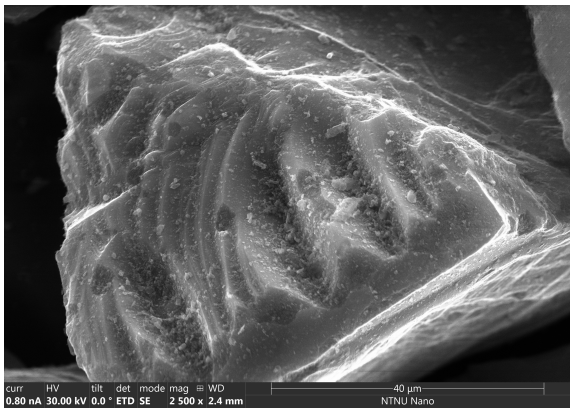

Figure 4.33: Surface morphology of MCS400 sample at 40µm magnification using a voltage of 30kV and a current of 0.80nA

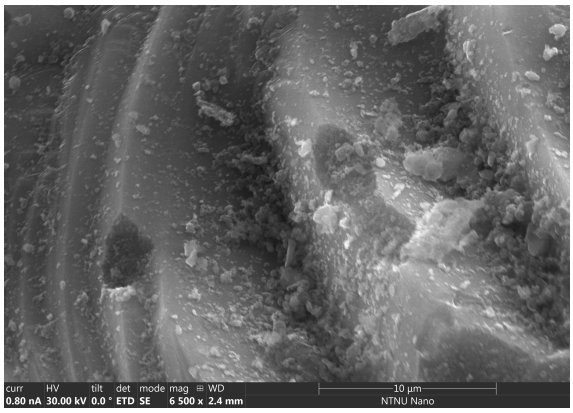

Figure 4.34: Surface morphology of MCS400 sample at 10µm magnification using a voltage of 30kV and a current of 0.80nA

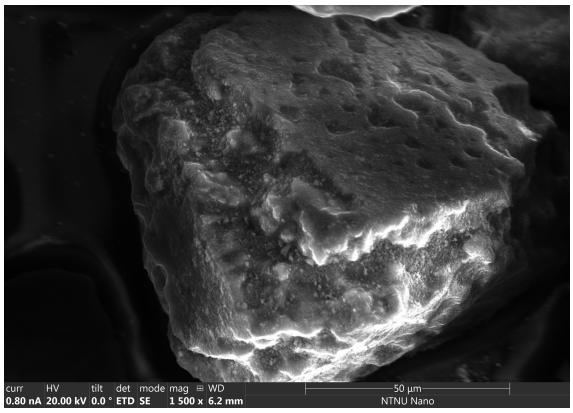

Figure 4.35: Surface morphology of MCS325 sample at 50µm magnification using a voltage of 20kV and a current of 0.80nA

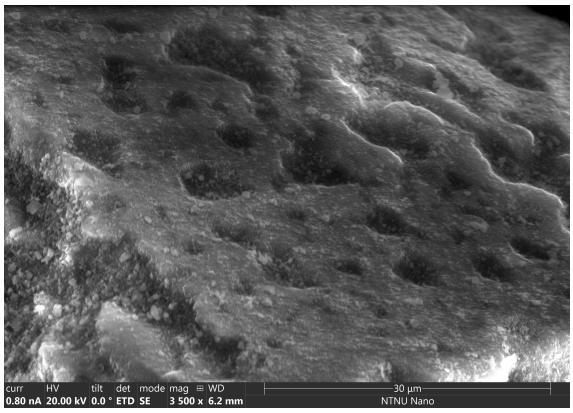

Figure 4.36: Surface morphology of MCS325 sample at 30µm magnification using a voltage of 20kV and a current of 0.80nA

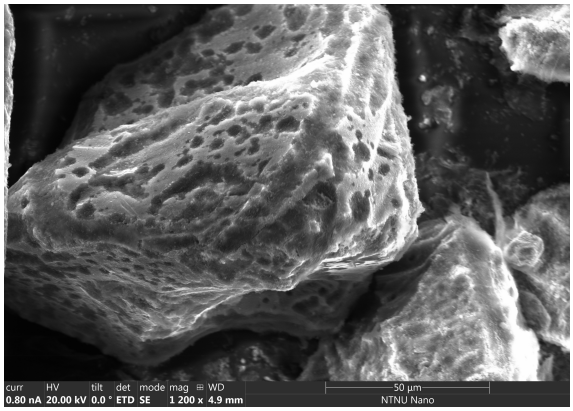

Figure 4.37: Surface morphology of MCS300 sample at 50µm magnification using a voltage of 20kV and a current of 0.80nA

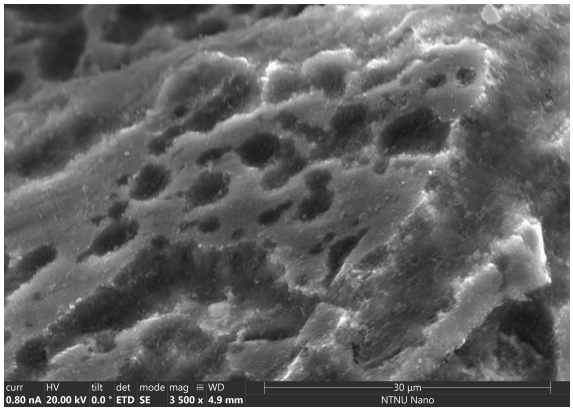

Figure 4.38: Surface morphology of MCS300 sample at 30µm magnification using a voltage of 20kV and a current of 0.80nA

Sample MCS-Cu is a unique sample that is the result of the reaction of methyl chloride with pure copper. Hence, the surface morphology that is observed is different from all other samples. This sample showed high heterogeneity in its particles. This heterogeneity can be recognized by the difference in morphology seen in Figure 4.39 and the one seen in Figure 4.40.

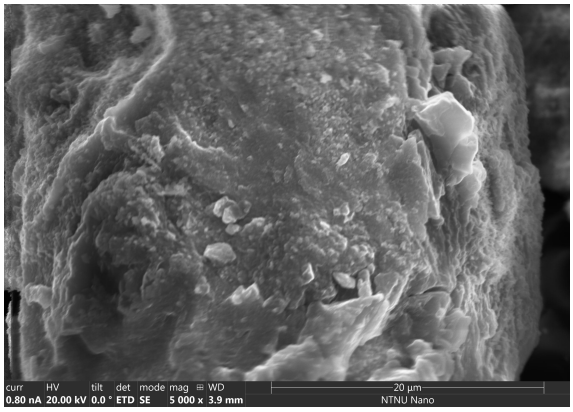

Figure 4.39: Surface morphology of a site on MCS-Cu sample at 20µm magnification using a voltage of 20kV and a current of 0.80nA

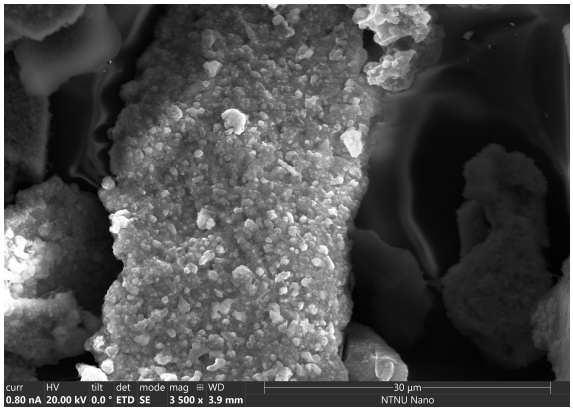

Figure 4.40: Surface morphology of a site on MCS-Cu sample at 30µm magnification using a voltage of 20kV and a current of 0.80nA

Elemental analysis has been done by EDS measurements on the site that suffered from severe silicon consumption in sample MCS400. The analysis shows the distribution of silicon, carbon, copper, chlorine, and oxygen. This analysis showed richness of copper and chlorine in the reaction pit where silicon was consumed. In addition, it showed even distribution of carbon, oxygen, and chlorine on the silicon particle. Elemental analysis of this site from MCS400 is shown in Figure 4.41. Furthermore, elemental analysis has been done by EDS measurements to study the similar reaction pits that were seen in MCS325 and MCS300 sites. The composition of reaction pits formed in MCS325 is observed in Figure 4.42 and that of the reaction pits formed in MCS300 is observed in Figure 4.43. In accordance with Banholzer and his coworkers, the reaction pits that are seen may be patches of the η-phase (Cu_3Si)[27]. Carbon is observed to have uniform distribution on the reaction pits in MCS325 and MCS300. According to Luo and coworkers, the coke that is deposited by the cracking of methyl chloride would hamper the diffusion of copper into the silicon matrix leading to a copper rich surface[23]. As for MCS-Cu, elemental analysis was done by EDS measurements in order to observe the deposition of carbon on free pure copper. Elemental analysis of a site from MCS-Cu sample can be seen in Figure 4.44. It can be seen that surface of copper has a high concentration of chlorine and this is due to methyl chloride cracking on free copper leading to the formation of CuCl which is supposed to react later with silicon in the case of the direct process to produce $SiCl_4$ and Cu. The surface of the copper also seems to be highly oxidized. However, distribution of carbon on the surface of copper doesn't seem to be highly concentrated.

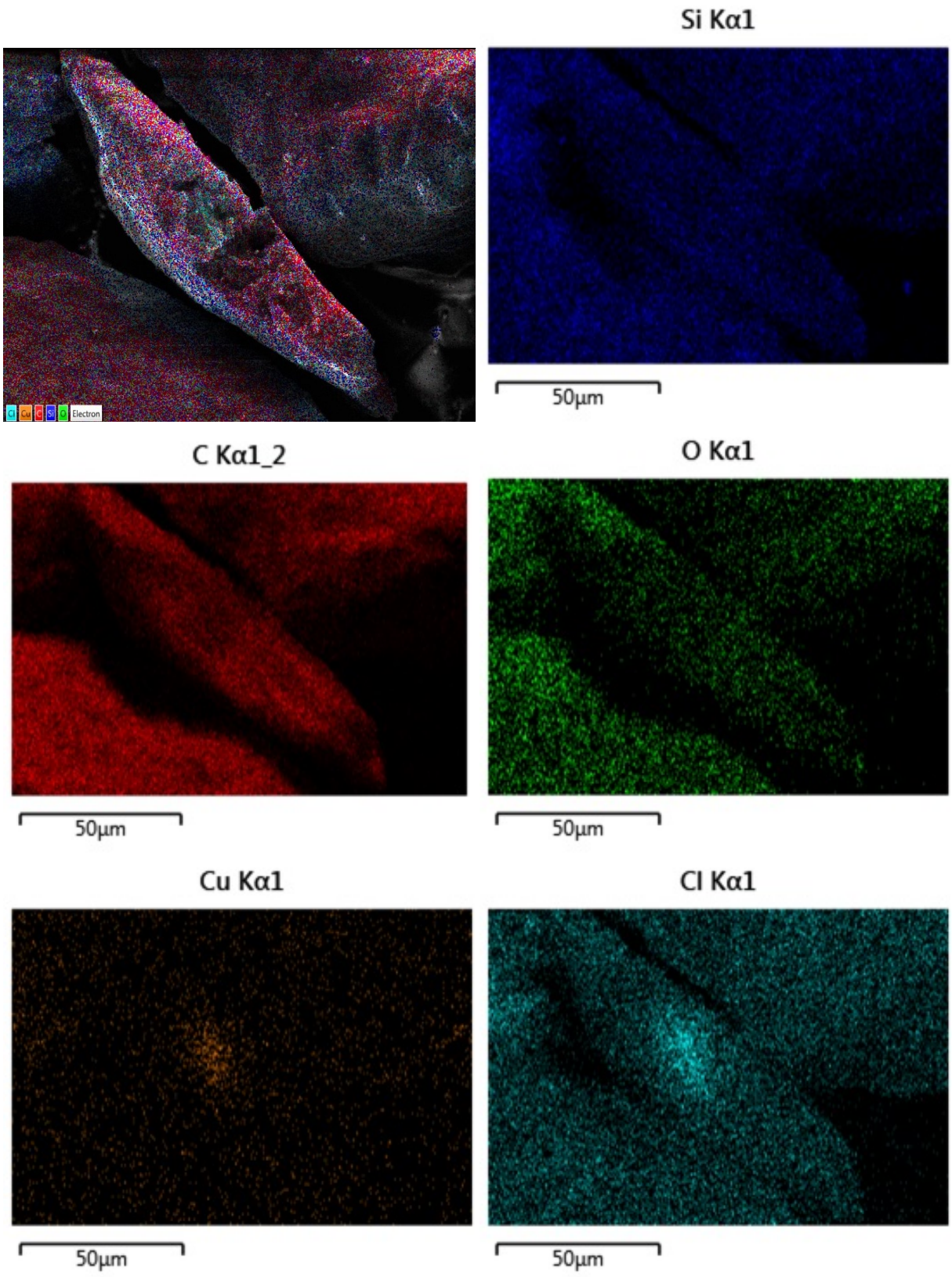

Figure 4.41: Elementary analysis of a site with severe silicon consumption from sample MCS400 showing the distribution of silicon, carbon, oxygen, copper, and chlorine.

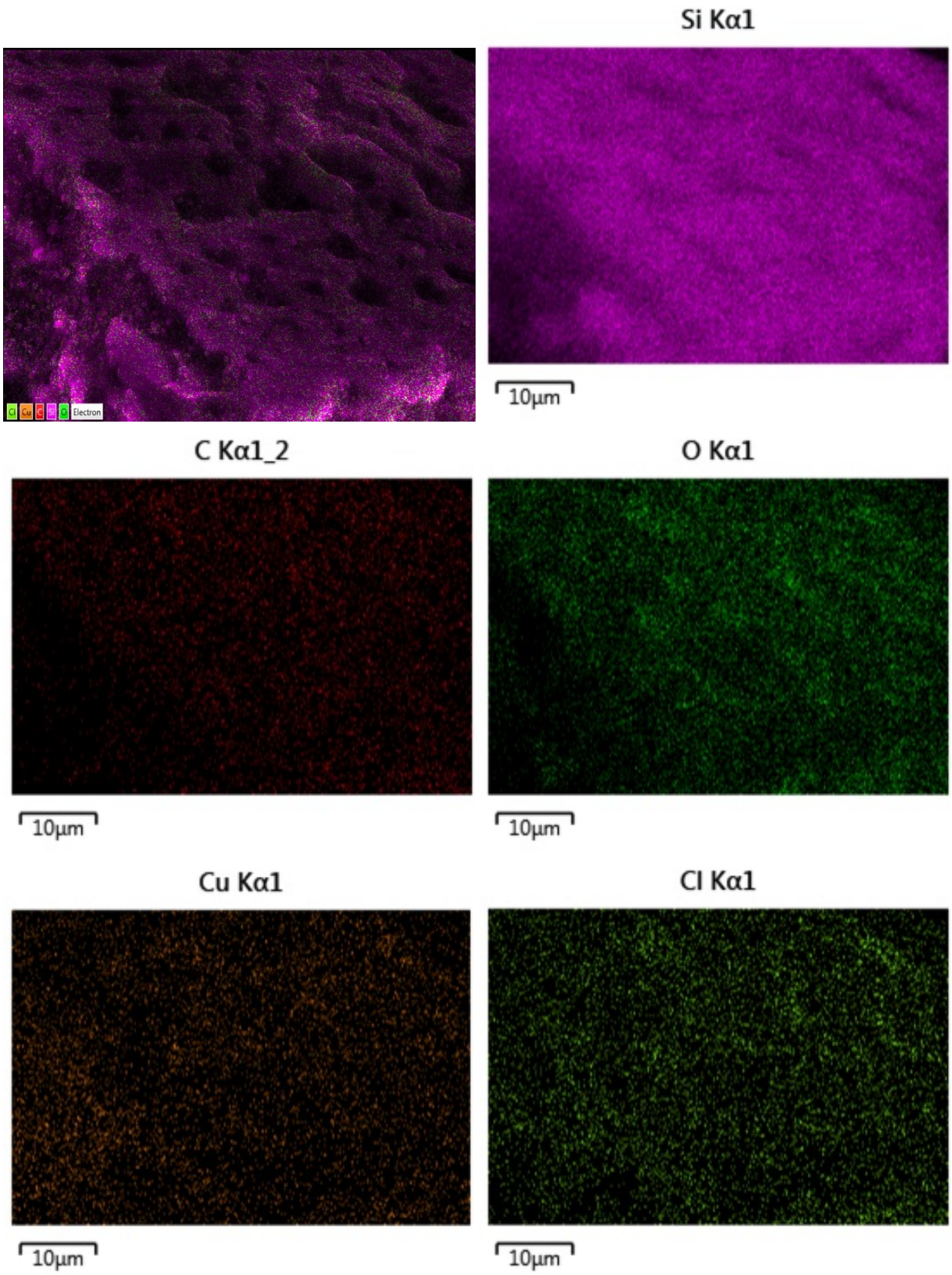

Figure 4.42: Elementary analysis of reaction pits seen on the surface from sample MCS325 showing the distribution of silicon, carbon, oxygen, copper, and chlorine.

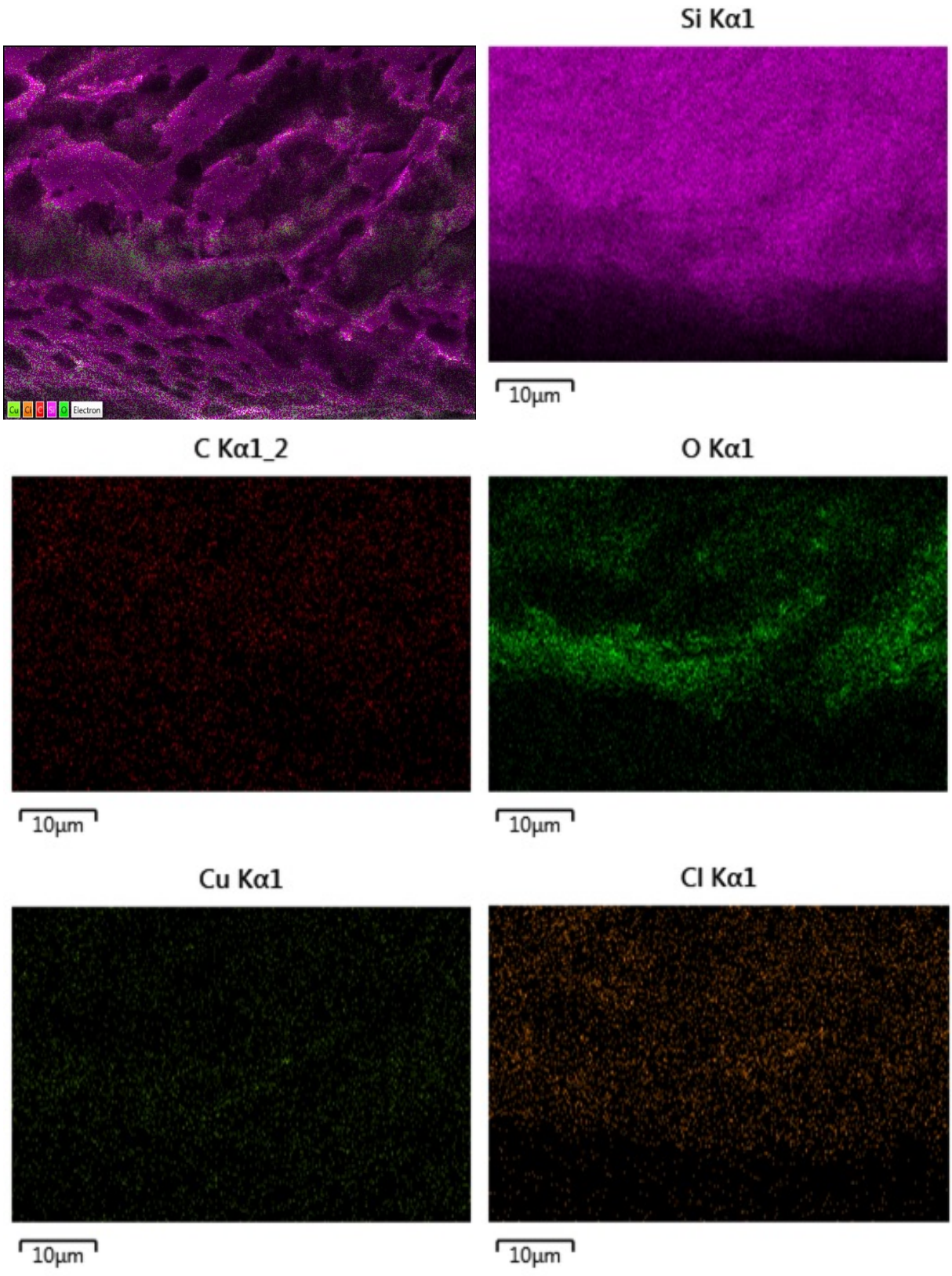

Figure 4.43: Elementary analysis of reaction pits seen on the surface from sample MCS300 showing the distribution of silicon, carbon, oxygen, copper, and chlorine.

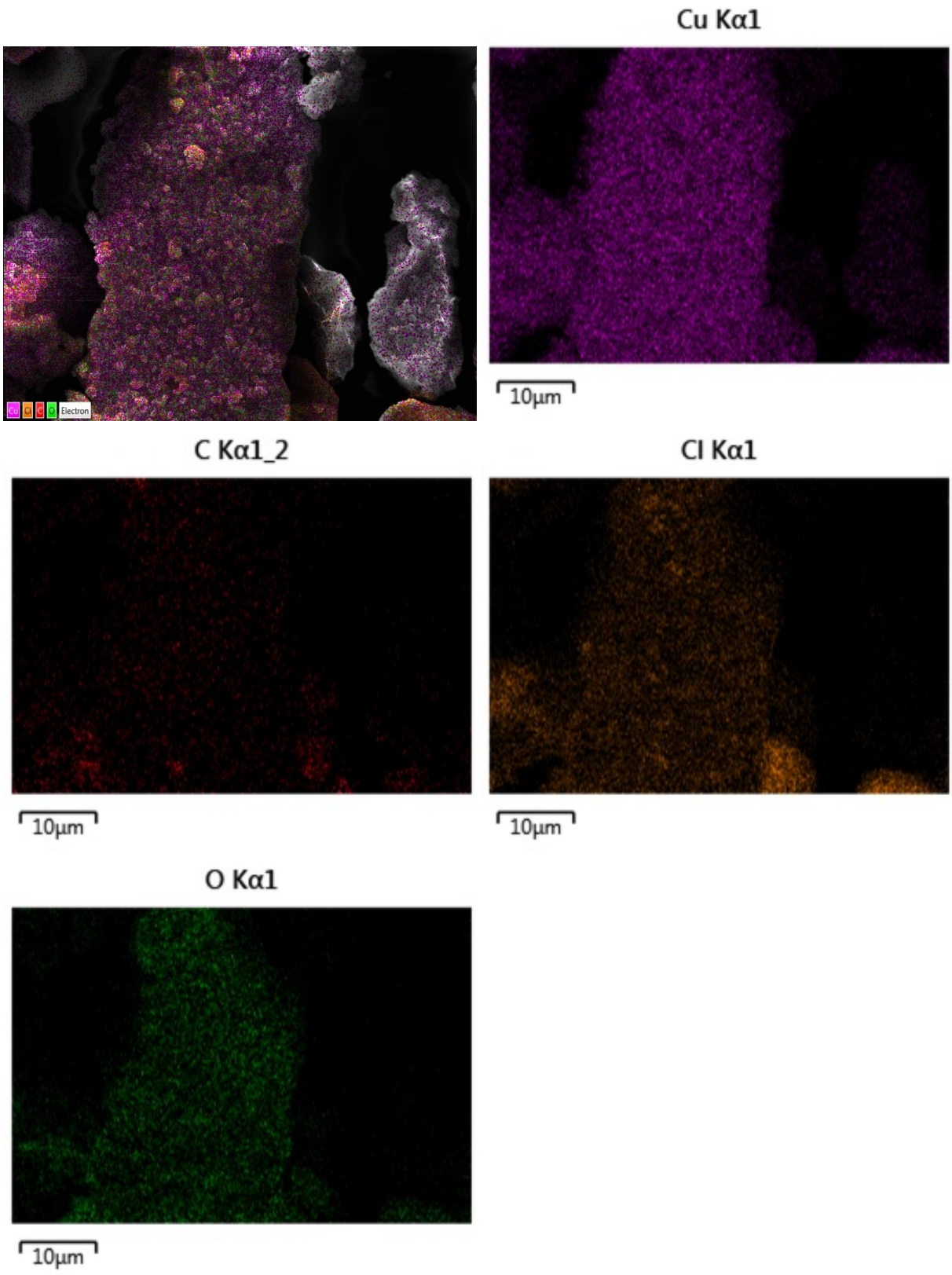

Figure 4.44: Elementary analysis of a site's surface from sample MCS-Cu showing the distribution of carbon, oxygen, copper, and chlorine.

4.4 Raman Spectroscopy

The Raman spectra of all four samples has been measured in the visible light region. In addition, Raman spectra of the pure silicon sample, SIL, has also been measured in order to be used as a reference. The measurements made for SIL samples are displayed in the appendix.

Raman spectra of MCS400, MCS325, and MCS300 have been collected and plotted in a single figure of intensity as a function of Raman shift. The peak with the highest intensity at 520cm^{-1} has been cut down in order to show the other peaks with lower intensities more clearly. The Raman spectra's intensity obtained for each of these three samples had been offset at an arbitrary starting value. Raman spectroscopy measurements for these three samples are displayed in Figure 4.45.

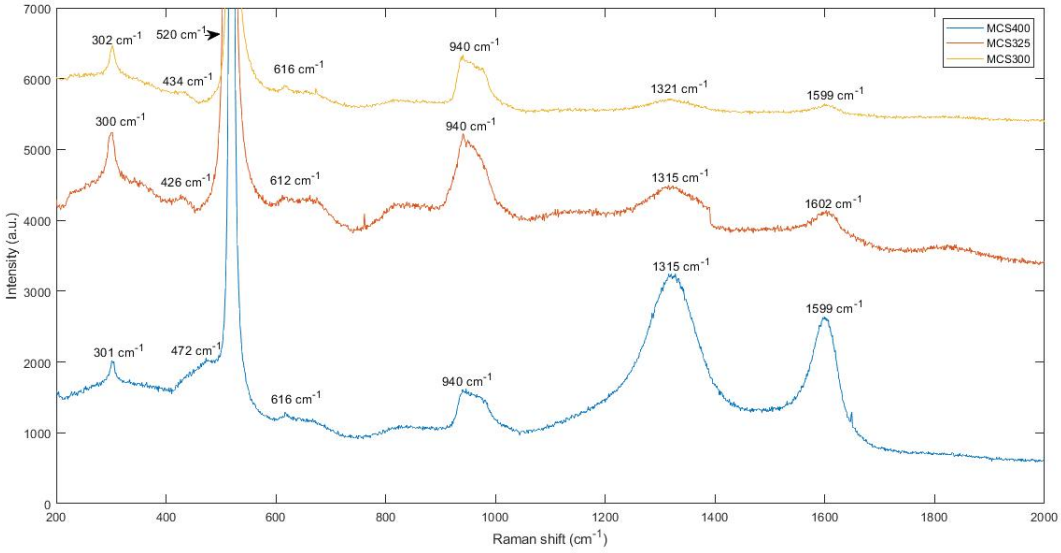

Figure 4.45: Raman spectra of MCS400, MCS325, and MCS300 in the visible light region. Highest intensity peak is modified to have same value for all three samples.

According to Uchinokura and coworkers, the peaks that are shown around 300cm^{-1}, 430cm^{-1}, 520cm^{-1}, 615cm^{-1}, and 940cm^{-1} are related to the standard Raman spectra of silicon[50]. This is also in accordance to the Raman spectra measurements obtained for SIL sample that showed the same peaks. The peak with the highest intensity observed at 520cm^{-1} is reported to be the main one-phonon peak[50]. Two-phonon spectrum is reported to be in the range between 600cm^{-1} and 1045cm^{-1} with the most intense peak usually between 920cm^{-1} and 1045cm^{-1}. Graczykowski and his coworkers declared that the peaks around 300cm^{-1} and 430cm^{-1} correspond to 2TA where TA

is the term used for transverse acoustic[51]. The highest intensity peak around 520cm^{-1} corresponds to LO where LO stands for longitudinal optical mode.

The peak around 615cm^{-1} corresponds to both TO and TA where TO stands for transverse optical. Finally, the peak around 940cm^{-1} corresponds to 2TO[51]. As for the other two peaks appearing around 1320cm^{-1} and 1600cm^{-1}, those peaks are related to carbonaceous materials. The band appearing around 1320cm^{-1} is defined as the (D) band where D stands for the term disorder and this band is related to structural defects in carbon materials[52]. The D band is described to be intense and broad in carbon that has poor order. On the other hand, the band appearing around 1600cm^{-1} is defined as the (G) band where G stands for the term graphitic band. The G band is a representation of in-plane vibrations aromatic carbons that have graphitic structure[52]. It has been reported that the G band is observed as a broad band at 1600cm^{-1} for carbons with poor order[52]. The ratio of intensity for the D band over the intensity of the G band (ID/IG) is used as a parameter for the disorder in the carbon materials being tested as this ratio increases with disorder[52]. For this reason, the (ID/IG) ratio has been calculated from the intensities obtained for each sample at the D and G bands and it is shown in Table 4.5.

Table 4.5: ID/IG ratio for MCS400, MCS325, and MCS300

Sample	ID (a.u.)	IG (a.u.)	ID/IG ratio
MCS400	3244	2640	1.23
MCS325	2992	2647	1.13
MCS300	714	643	1.11

Furthermore, MCS-Cu has also been characterized by Raman spectroscopy. Results for MCS-Cu are shown in separate figures since the composition of this sample is different than the other three samples. Three different sites have been tested for sample MCS-Cu and each site yielded different Raman spectra. Site one produced Raman spectra containing two significant peaks which are the D and G band related to carbonaceous material as discussed for the other samples. Raman measurements for site one are displayed in Figure 4.46. Site two produced Raman spectra with four distinct peaks around 293cm^{-1}, 342cm^{-1}, 623cm^{-1}, and 1103cm^{-1}. Xu and coworkers have declared that the peaks present at 293cm^{-1}, 342cm^{-1}, and 623cm^{-1} are related to copper(II) oxide[53]. They have declared that those three Raman peaks are the result of vibration of the oxygen atoms[53]. It was also reported that those peaks would look sharper and stronger with a shift to a higher wavenumber if the grain size increases[53]. The peak observed at 1103cm^{-1} is probably related to carbon species. Tallant and coworkers have reported that Raman spectra of amorphous carbon films exhibited a broad band in the range of 1100 to 1200 cm^{-1}, and this band has been related to four-coordinated carbon structures[54]. However, this band has been reported to be difficult to detect in the visible region and ulraviolet excitation is usually used to detect it[54].

Raman measurements for site two are displayed in Figure 4.47. As for the third and final site in MCS-Cu, Raman spectra measurements showed four distinct peaks around 281cm^{-1}, 337cm^{-1}, 1325cm^{-1}, and 1589cm^{-1}. The peaks at 281cm^{-1} and 337cm^{-1} are related to copper(I) oxide while the peaks at 1325cm^{-1} and 1589cm^{-1} are the D and G bands related to carbonaceous materials. The peak at 623cm^{-1} related to copper(II) oxide is not distinctly seen in the Raman spectra of this site. Raman measurements for site three of sample MCS-Cu are displayed in Figure 4.48.

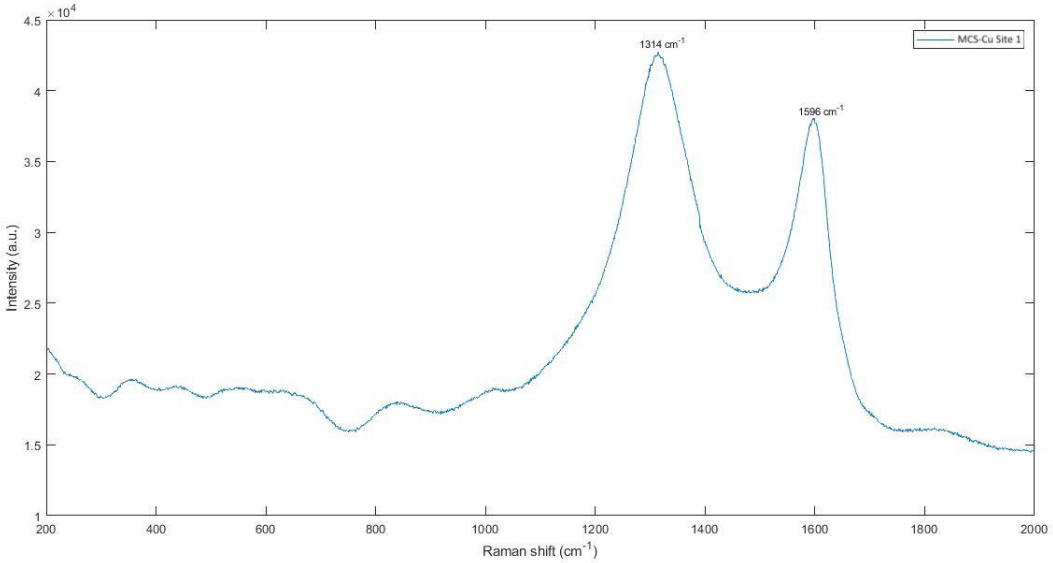

Figure 4.46: Raman spectra of site 1 from sample MCS-Cu showing the D and G bands obtained from the visible light region

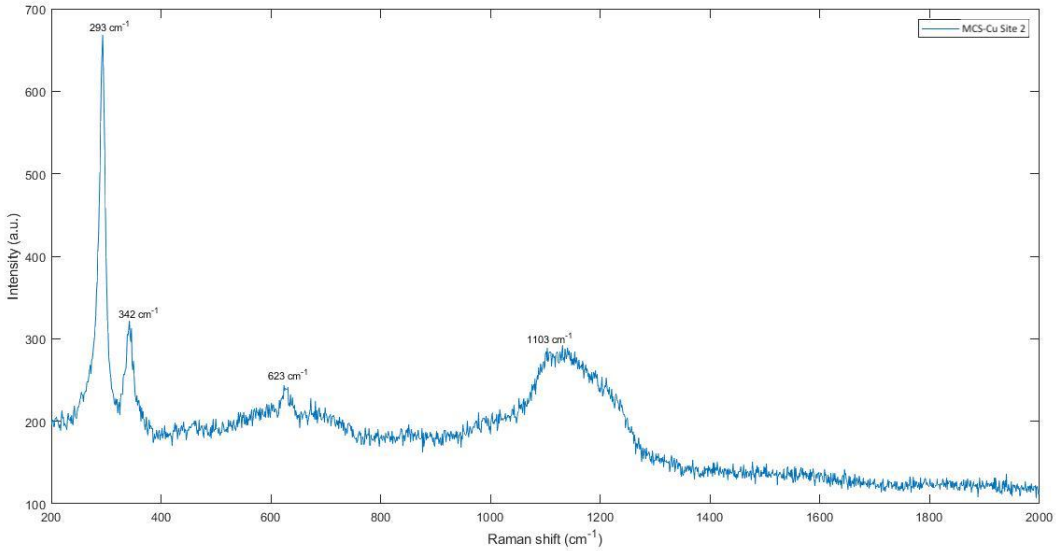

Figure 4.47: Raman spectra of site 2 from sample MCS-Cu obtained from the visible light region

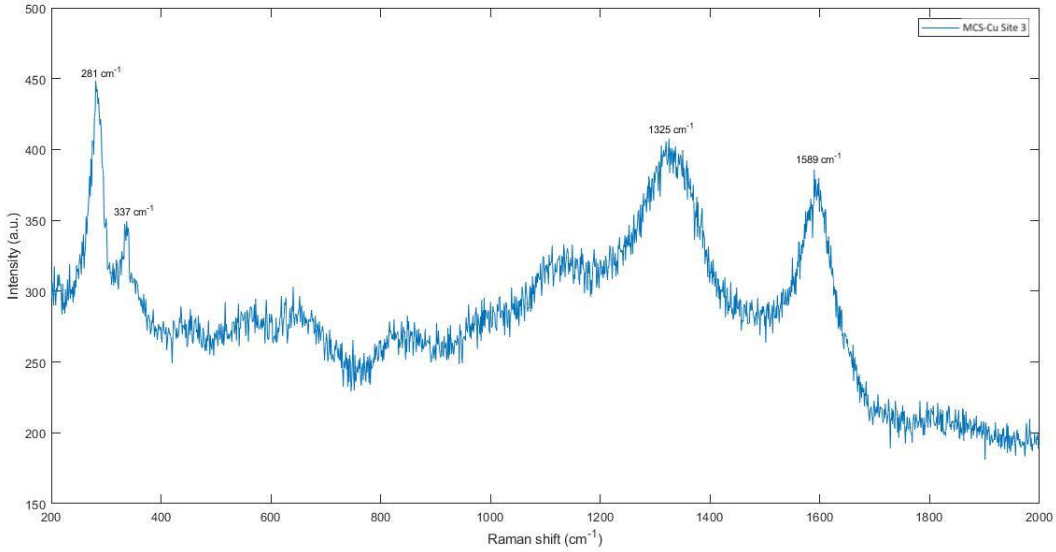

Figure 4.48: Raman spectra of site 3 from sample MCS-Cu obtained from the visible light region

4.5 X-ray diffraction

MCS400, MCS325, MCS300, and reference sample SIL have been examined by X-ray diffraction. Due to insufficient amount of MCS-Cu, it was not examined by X-ray diffraction. In addition, sample SIL has been examined to be used as a reference for the silicon peaks. X-ray diffraction results for MCS400, MCS325, and MCS300 are shown in Figure 4.49. The obtained peaks were matched with a powder diffraction file (PDF) that shows the standard peaks for silicon.

The measurements for all three contact mass samples yielded similar results with the most intense peak being at 28 2θ degrees. In addition to the silicon peaks observed in the results, the η-phase (Cu_3Si) was also seen with really small intensity peaks at 44.6 2θ degrees and 45 2θ degrees in samples MCS400 and MCS300. It is represented clearly in separate figures in the appendix due to the large difference in intensities compared to silicon.

The peak with the highest intesity for silicon at 28 2θ degrees corresponds to silicon(111) arrangement. The four other peaks observed for silicon at 47 2θ degrees, 56 2θ degrees, 69 2θ degrees, and 76 2θ degrees correspond to silicon(220), silicon(311), silicon(400), and silicon(331) respectively. Crystallite sizes of each sample have also been calculated with the Scherrer equation using the full width at half maximum intensity of the peak (FWHM) and the calculations are displayed in the appendix. Table 4.6 shows the phases found in each sample, FWHM, and the crystallite sizes in nanometer calculated from the Scherrer equation.

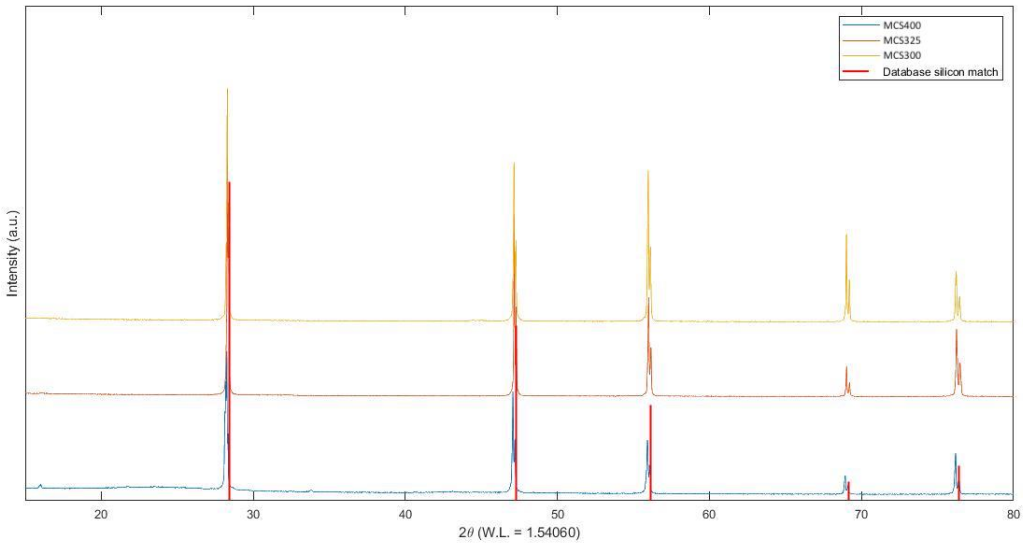

Figure 4.49: X-ray diffractogram obtained for MCS400, MCS325, and MCS300 within the 2θ range of 15°- 80°. Diffraction lines of silicon from the database were added as a reference.

Table 4.6: Phases detected in X-ray diffraction for each sample and their calculated crystallite sizes

Sample	Phases observed	FWHM	Crystallite size(nm)
MCS400	Silicon and Cu_3Si	0.167	54
MCS325	Silicon	0.083	109
MCS300	Silicon and Cu_3Si	0.088	103

4.6 Infrared Spectroscopy of extracts

The first Soxhlet extraction experiment was done on MCS-Cu with dichloromethane as a solvent for a period of 6 hours. After 6 hours, the obtained solution in the round bottom flask had a clear color change from the transparent color of dichloromethane to a dark color. First, the infrared spectrum of dichloromethane was obtained in order to be used as a reference. The spectra of the extract and dichloromethane have been fitted in the same figure in order to compare the obtained bands. The results for MCS-Cu extract spectrum along with dichloromethane spectrum can be seen in Figure 4.50. The clear difference that can be seen in the two spectra is the percentage of transmittance as the extract of MCS-Cu had lower transmittance at 702 cm^{-1},731 cm^{-1}, and 1264 cm^{-1}. Larkin reported that C-Cl stretching vibrations occur in the range of 505-860 cm^{-1}, and this explains the bands that are observed at 702 cm^{-1} and 731 cm^{-1}[55]. According to Chen and his coworkers, the band that is observed around 1264 cm^{-1} is related to the wiggling mode of CH_2 in dichloromethane[56]. In addition, the transmittance bands at 2852 cm^{-1} and 2923 cm^{-1} do not seem to appear in the spectrum of the extract of MCS-Cu. According to Larkin, the band around 2923 cm^{-1} could be related to the stretching of methylene CH bands[55].

Another attempt to extract carbonaceous species was done with sample MCS400. The Soxhlet extraction experiment was stopped after 24 hours this time. There was also a clear color change from transparent to a dark color. The spectra of MCS400 extract and dichloromethane have been fitted in the same figure in order to compare the obtained bands. The results for MCS400 extract spectrum along with dichloromethane spectrum can be seen in Figure 4.51. The results obtained are similar to those of MCS-Cu extract. Lower transmittance was seen for MCS400 extract at 702 cm^{-1},731 cm^{-1}, and 1264 cm^{-1}. The transmittance bands around 2852 cm^{-1} and 2923 cm^{-1} also do not seem to appear in the spectrum of the extract of MCS400.

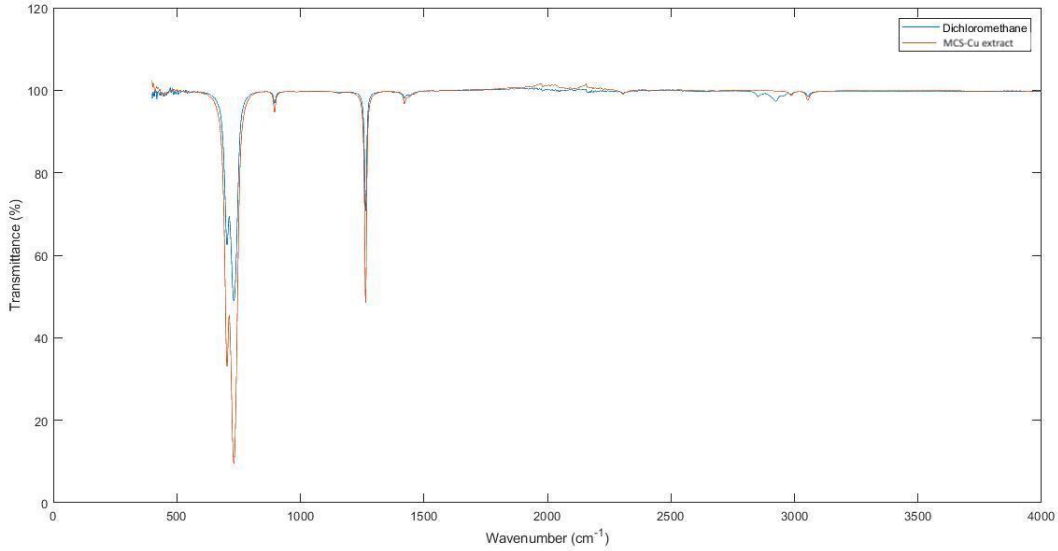

Figure 4.50: ATR-FTIR spectra of MCS-Cu extract and dichloromethane within the wavenumber range of 400-4000 cm^{-1}

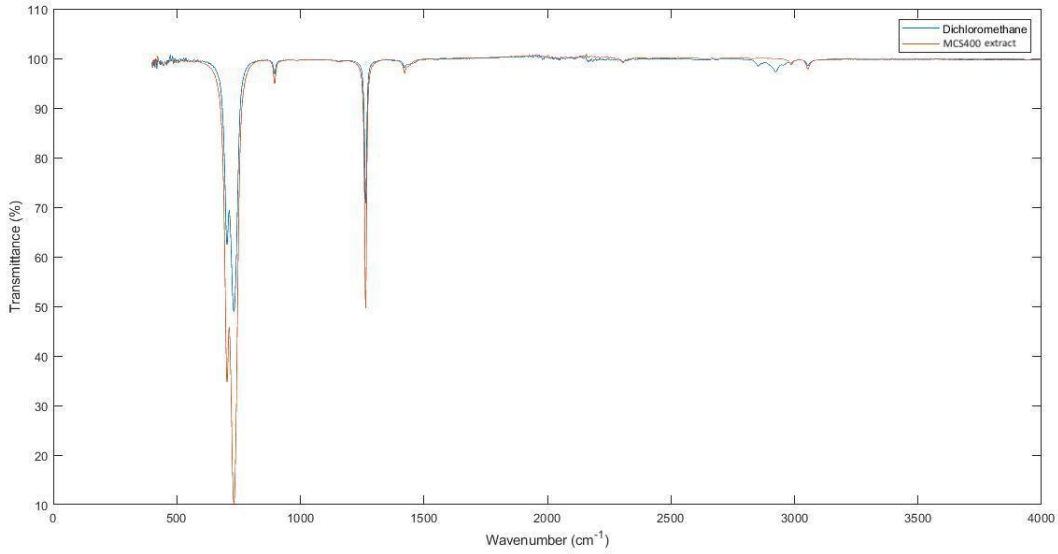

Figure 4.51: ATR-FTIR spectra of MCS400 extract and dichloromethane within the wavenumber range of 400-4000 cm^{-1}

5 Discussion

5.1 Thermal analysis

Thermal analysis has been conducted on all four samples MCS400, MCS325, MCS300, and MCS-Cu in both oxidizing and inert atmospheres. The change in mass has been investigated as a function of increasing temperature. Mass spectrometry is utilized to detect the gases evolving from the samples upon heating and those are to be correlated with the mass changes observed. In addition, the pure silicon sample, SIL, has been tested in thermogravimetric analysis to observe pure silicon's behavior under the used temperature profile.

In oxidizing atmosphere, the most significant mass losses witnessed were for samples MCS400 and MCS-Cu. Sample MCS400 recorded a mass loss of approximately 37%. The major mass of MCS400 loss occured in the temperature range 283°C-530°C. A sharp exothermic peak appears during this period accompanied with the formation of CO_2 and CH_4 at a temperature around 435°C. This means that the mass loss could be directly accredited to the formation of CO_2 and CH_4. Mass spectrometry also showed the formation of CH_3Cl at a temperature around 340°C. It is worth noting that the evolution of CO_2 occurred at a temperature close to the high process temperature (400°C) set for MCS400, and that CH_3Cl evolved at a temperature that is in the typical reaction temperature range for the direct process. The appearance of H_2O in the mass spectrometry at early stages in the experiment could be explained by drying of the sample. However, H_2O also appeared at temperatures above 300°C which could be explained by the release of hydrogen from C-H or O-H bonds in the carbonaceous species. CH_4 has been reported by Launer to be a hydrocarbon byproduct of the direct process[8], but its appearance in the mass spectrometry results could be due to the decomposition of carbonaceous species in the contact mass. Since MCS400 has shown significant mass loss that is accredited to carbonaceous species, it seems that increasing the process temperature highly increases the carbon formation in the direct process leading to a higher deactivation rate.

Furthermore, MCS-Cu showed the highest mass loss of approximately 61% in oxidizing atmosphere. Major mass loss of MCS-Cu occurs in the temperature range of 411°C-780°C. The evolved CO_2 observed in the mass spectrometry showed two distinct peaks in the temperature range 378°C-460°C accompanied by two exothermic peaks shown by DSC. Wessel reported in his paper that significant coking occurs on metallic copper, and it was suggested that coke formation occurs mainly on bulk metallic copper[25]. This explains the high amount of coke that is observed in this sample. A strange observation is that the first CO_2 peak appears a short time before the major mass loss occurs. Wessel also suggested that there are two types of coke forming on the contact mass: α-coke and β-coke[25]. The difference between those two forms of coke is that β-coke seems to be more aromatic in nature.

α-coke was reported not to have an influence on the reaction rate, but it is the β-coke that is capable of blocking active sites for dimethyldichlorosilane formation[25]. Two compounds also appear in the mass spectrometry before the major mass loss occurs which are CH_3Cl and H_2O at temperatures above 230°C.

A compound that is unique to MCS-Cu in mass spectrometry is Cl_2 which appears during the major mass loss period. The appearance of Cl_2 could be explained by the fact that the sample is highly chlorinated due to the cracking of methyl chloride on the surface of metallic copper.

Samples MCS325 and MCS300 showed almost identical behavior in thermogravimetric analysis. The mass loss for both samples did not exceed 2.6% where most of the mass loss could be accredited to drying of the samples in the first few minutes. The minor mass losses occuring in the temperature ranges 104°C-516°C for MCS325 and 104°C-476°C for MCS300 could be accredited to the evolution of CO_2 at 322°C and CH_3Cl at 334°C for both samples. According to Wessel, contact mass promoted with zinc and tin operated at a temperature of 310°C had evolved β-coke at a temperature of 338°C, which is close to the value seen for evolution of CO_2 from MCS325 and MCS300[25]. This might mean that the coke evolving from samples MCS325 and MCS300 is what Wessel referred to as β-coke that leads to deactivation of the contact mass. After the mass loss occurs, some mass gain is witnessed in the samples. This could be related to silicon oxidation which is highly enhanced when it is in an alloyed state[25]. The similarity in the behavior seen for MCS325 and MCS300 in thermogravimetric analysis and the low carbon content obtained for these two samples shows that the variation of reaction temperature between 300°C and 325°C does not highly influence carbon formation.

In inert atmosphere, where argon was used as a purge gas, MCS400 and MCS-Cu also showed significant mass loss. A total mass loss of approximately 10% is seen in MCS400 where initially the mass loss was caused by drying of the sample in the first couple of minutes. Mass loss proceeded in a linear manner after drying accompanied by the evolution of CO_2, CH_4, CH_3Cl, and H_2O. Three peaks were seen for CO_2 in mass spectrometry in the temperature range 328°C-800°C. In addition to initial drying, two peaks for H_2O were also seen in the temperature range 652°C-800°C. Only one distinct peak was seen for CH_4 at 586 °C, and also one peak appeared for CH_3Cl at 610°C. All the evolved gases correlate with the mass loss observed since the mass loss is continuous with the temperature increase. Appearance of H_2O at temperatures higher than 650°C could also be explained by the release of hydrogen from C-H or O-H bonds in the carbonaceous species.

Sample MCS-Cu showed very high mass loss of approximately 75%, which is even higher than the one seen in oxidizing atmosphere. It has to be to taken into account that the sample highly in-homogeneous and this was inspected in Raman spectroscopy as well. The observed CO_2 peaks are accompanied by exothermic peaks in the DSC,

but there are also several endothermic peaks seen in the heat exchange flow. H_2O also appeared at a temperature higher than 200°C in this case. Another compound contributing to the mass loss was CH_4 which appeared as two small peaks in the minor mass loss period. The mass loss of MCS-Cu in inert atmosphere is similar to that seen in oxidizing atmosphere. Mass loss for MCS400 was distinctly less in inert atmosphere. This might indicate that the stability of the carbon formed in MCS-Cu is different than that of contact mass in MCS400 where the carbon in MCS400 showed higher stability in inert atmosphere.

Samples MCS325 and MCS300 also showed almost identical behavior in an inert atmosphere where the mass loss did not exceed 3% in both samples. Most of the mass loss occurs in the early period of the experiment and this could be accredited to drying of the samples. CO_2 and H_2O were the only compounds inspected by mass spectrometry. For MCS325, CO_2 signal appeared as a broad peak centered at 562°C, and the H_2O signal closely at 547°C. As for MCS300, CO_2 signal appeared as three peaks in the range of 487°C-792°C, and H_2O signal appeared at 566°C similarly to MCS325. The evolution of CO_2 in an inert atmosphere gives an insight that the samples are already oxidized. This was confirmed by the other characterization techniques used for this project. This might mean that the evolved CO_2 and the observed mass loss in inert atmosphere could be the result of decomposition of hydrocarbon by-products found within the tested samples.

5.2 Surface morphology and composition

Surface morphology of all four samples MCS400, MCS325, MCS300, and MCS-Cu has been studied in order to see how the morphology changes after the reaction. Elemental analysis has also been done to examine the composition of the studied samples. Copper, silicon, carbon, chlorine, and oxygen have been seen in all samples except MCS-Cu that is silicon-free. In addition, the surface morphology of the pure silicon sample, SIL, has been examined in order to be used as a reference for non-reacted silicon.

A process temperature of 400°C had a distinguishable effect on sample MCS400. It can be seen that the contact mass is fiercely consumed due to high temperature. A reaction pit witnessed in MCS400 seemed to have a high concentration of copper and chloride. It seems that this is the site where copper(I) chloride reacts with the silicon to form the active sites for methylchlorosilanes production. This also explains the depletion of silicon in the reaction pit seen. The carbon formed seemed to cover the surface of the contact mass evenly in high concentrations as well.

Samples MCS325 and MCS300 showed somehow similar surface morphology. The consumption of silicon did not seem to be fierce like in MCS400. The reaction pits for the formation of methylchlorosilanes are clearly seen on the

surface of both samples. According to Banholzer and his coworkers, the observed reaction pits may be patches of the η-phase (Cu_3Si)[27]. It was expected to see a higher concentration of copper in the reaction pits of MCS325 and MCS300, but the copper seemed to be evenly distributed on the surface of silicon.
Chlorine, carbon, and oxygen also seemed to be evenly distributed on the surfaces of both MCS325 and MCS300. Banholzer and his coworkers indicated the oxide layer formed on the silicon can act as a barrier for the contact between copper and silicon[27]. Elemental analysis has not shown any specific sites for carbon deposition, but it showed that the carbon deposits all over the surface leading to the blocking of the active sites for methylchlorosilanes production.

Elemental analysis of MCS-Cu has shown that the surface of bulk metallic copper is highly chlorinated after the cracking of methyl chloride on it. In addition, it seems to be highly oxidized as well. It was expected to see higher concentrations of carbon the surface due to the high carbon content, however the concentration of carbon did not seem to be very high on some of the inspected sites. This can be explained by the in-homogeneity of the sample as seen by Raman spectroscopy results where some sites contained only copper(II) oxide.

5.3 Pyrolysis decomposition products

All the samples have been tested in a pyrolysis-gas chromatography setup that is connected to a mass spectrometer in order to see the resulting decomposition products. Three common products were found in all the samples which are carbon dioxide, n-hexadecanoic acid, and octadecanoic acid. In addition to those three compounds, MCS300 had two additional decomposition products detected by the mass spectrometer. All the detected compounds along with their chemical formulas are listed in Table 5.1.

Table 5.1: All the compounds detected by mass spectrometry after pyrolysis-gas chromatography of all the samples

Detected Compound	Chemical Formula	Relevant in
Carbon dioxide	CO_2	MCS400,MCS325,MCS300,MCS-Cu
n-Hexadecanoic acid	$C_{16}H_{32}O_2$	MCS400,MCS325,MCS300,MCS-Cu
Octadecanoic acid	$C_{18}H_{36}O_2$	MCS400,MCS325,MCS300,MCS-Cu
Phthalic acid, 2-ethoxyethyl ethyl ester	$C_{14}H_{18}O_5$	MCS300
8-Methoxy-quinoline-5-sulfonic acid butylamide	$C_{14}H_{18}N_2O_3S$	MCS300

Since the amount of sample being tested in pyrolysis-gas chromatography is really small, it should be noted that each experiment has been reproduced several times. There is a possibility to obtain other organic compounds

since the samples have shown to be in-homogeneous. The common factor that is seen in the obtained compounds is the length of the carbon chains. In addition to the two acids obtained from all four samples, an ester and an amide were also obtained from sample MCS300. According to Elkem, MCS300 has suffered from some minor issues during the run and this might explain the appearance of an ester and an amide in the mass spectrometry. Another common factor seen in the obtained compounds is the presence of the oxygen bond. It has been noticed from the used characterization methods that oxygen is present in all the samples. According to Clarke, the presence of oxygen facilitates the breaking down of methyl chloride on the contact mass without affecting the rate of formation of dimethyldichlorosilane, but it affects the selectivity towards dimethyldichlorosilane[14]. As stated previously, the oxide layer can act as a barrier for the contact between copper and silicon and this might lead to the presence of more free copper on the surface. Consequently, the presence of free copper on the surface leads to high carbon deposition. This indicates that the presence of oxygen might indirectly influence higher carbon deposition on the surface of the contact mass. Just like the conditions for inert thermogravimetric analysis, pyrolysis-gas chromatography is also run in inert conditions with helium being the carrier gas. This further supports the idea that the CO_2 obtained in inert thermogravimetric analysis is the result of the decomposition of hydrocarbon by-products present in the contact mass.

In terms of abundance, there was a variation for the highest abundant compound found in the four samples. MCS-Cu has shown to have the highest abundances for the oxygenated carbon compounds detected, and this is expected since the sample is highly oxidized and contains high amounts of carbonaceous species. MCS325 and MCS300 showed another form of similarity where the most abundant decomposition product from those samples was n-Hexadecanoic acid.

5.4 Raman spectroscopy

Raman spectroscopy revealed similar peaks for all contact mass samples MCS400, MCS325, and MCS300. The most intense peak obtained for these three samples is observed to be at a Raman shift of 520cm^{-1} and this peak corresponds to crystalline silicon. This peak has shown the highest intensity due to the fact that the contact mass is mainly made from silicon with only trace amounts of catalyst copper and promoters. The four other peaks observed around 300cm^{-1}, 430cm^{-1}, 615cm^{-1}, and 940cm^{-1} are also indicated to be related to crystalline silicon. This was also supported by the Raman spectra obtained for the pure silicon sample, SIL. However, as seen from the Raman spectra of MCS-Cu, two of the copper(II) oxide bands are located around 293cm^{-1} and 623cm^{-1}. Those two peaks could be contributing to the silicon peaks located at 300cm^{-1} and 615cm^{-1} since they are really close. The band that

is seen at 940cm^{-1} showed a distinct shape for all samples of contact mass. According to Socrates, there is a band that occurs in the range of 800-985cm^{-1} that is related to the deformation vibration of the Si-H group[57]. Due to the in-homogeneity of sample MCS-Cu, three different sites inspected with Raman spectroscopy yielded three different Raman spectra. The first site yielded Raman spectra that showed the D and G bands related to the carbonaceous species and they appeared at a Raman shift around 1320cm^{-1} and 1600cm^{-1} respectively at very high intensities. Another site yielded peaks related to copper(II) oxide and a peak related to carbon. The third and final site from MCS-Cu yielded Raman spectra showing peaks for copper(II) oxide and the D and G bands for carbon. This shows that some sites are rich in copper, other sites are rich in carbon, and some sites have a combination of both. This confirms why the inspected site of MCS-Cu in scanning electron microscopy did not show higher concentrations of carbon even though the sample is rich in carbonaceous species.

The inspected disorder (D) and graphitic (G) bands located around 1320cm^{-1} and 1600cm^{-1} respectively are related to the presence of carbonaceous species. As it has been observed, the intensity of those two peaks is way smaller than the intensity seen for silicon in samples MCS325 and MCS300. This could be due to the small amounts of carbon present in these two samples. According to Brolly and his coworkers, the G band occurs as a broad band located at 1600cm^{-1} in poorly ordered carbon and the D band also occurs as intense and broad in the case of carbon material with poor order[52]. The ratio of intensity of the D band over the intensity of the G band has been calculated for the contact mass samples. This ratio is used as an indicator for the disorder of the carbonaceous species found in the samples, and the ratio increases with the increase of the disorder.
MCS400 (process temperature 400°C) has shown to have the highest (I_D/I_G) ratio indicating that it has the highest degree of disorder followed by MCS325 (process temperature 325°C) and the lowest ratio was for MCS300 (process temperature 300°C). This indicates that the process temperature has an effect of increasing the disorder of the carbon formed during the direct process.

5.5 Crystalline structure

Samples MCS400, MCS325, and MCS300 were all examined by X-ray diffraction. MCS-Cu was not examined due to insufficient amount of the sample supplied. The pure silicon sample, SIL, has also been examined in order to be used as reference for the silicon peaks. The three examined samples showed peaks related to crystalline silicon with varying intensities. The structure of the silicon in the samples shows to be similar with peaks corresponding to silicon(111), silicon(220), silicon(311), silicon(400), and silicon(331). The crystallite sizes have been calculated

by using the Scherrer equation where MCS325 and MCS300 had similar crystallite sizes. However, the crystallite size calculated for MCS400 has shown to be approximately half of that calculated for MCS325 and MCS300. This correlates well with the morphology observed for MCS400 where some particles seemed to be fiercely consumed. In addition to the silicon phases identified by X-ray diffraction, the η-phase (Cu_3Si) has also been detected in MCS400 and MCS300. The Cu_3Si phase has been detected in the range of 44°-45°with peaks corresponding to very minimal intensity. Luo and coworkers reported finding Cu_3Si and $Cu_{15}Si_4$ in their X-ray diffraction analysis, but the $Cu_{15}Si_4$ phase was not seen here[23]. In another work done by Chen and coworkers, $Cu_{6\cdot 69}Si$ was also reported to be found in X-ray diffraction of waste contact mass but no peaks appeared for it in the results obtained[58]. The minimal intensity seen for Cu_3Si might be due to the fact that the samples were examined a long time after they were taken from the reactor, but it still shows the presence of the alloyed state of the silicon which is the active state of the contact mass. Luo and his coworkers also highlighted the fact that presence of free copper is very harmful to the direct process[23].

Furthermore, X-ray diffraction results did not show any peaks that are related to carbon. Even for the carbon rich sample, MCS400, no carbon peaks were detected. Luo and his coworkers also reported that carbon peaks did not appear in their X-ray diffraction experiments, and they have suggested that the carbon formed during the direct process might be of an amorphous form[23].

5.6 Infrared spectroscopy of extracts

As an attempt to extract carbonaceous species, Soxhlet extraction was carried out on two different carbon rich samples. This would make it easier to analyze the carbonaceous species by themselves without the other components. The first attempt was done on sample MCS-Cu where a small amount of sample was placed in a Soxhlet extraction setup. After 6 hours of extraction, the extract was collected and analyzed by attenuated total reflection Fourier-transform infrared spectroscopy. The infrared spectrum of dichloromethane was analyzed prior to the extract in order to compare the obtained bands. The bands obtained from the infrared spectrum of the extract of MCS-Cu has shown to be quite similar to that of dichloromethane. The only difference witnessed is the percentage of transmittance at three bands located at $702cm^{-1}$, $731cm^{-1}$, and $1264cm^{-1}$. The bands seen at $702cm^{-1}$ and $731cm^{-1}$ are related to C-Cl stretching vibrations, and the band at $1264cm^{-1}$ has a relation with wiggling mode of CH_2. There were no bands that could be related to hydrocarbons. The Soxhlet extraction of MCS-Cu was stopped after a clear color change in the solvent and it was expected to carry carbonaceous species. It was believed that running the

extraction for a longer period of time would yield an extract rich in carbonaceous species but the amount of MCS-Cu left was insufficient to run another extraction experiment.

For that reason, MCS400 was chosen since it is also carbon rich and more relevant by being a sample of contact mass. The extraction experiment was run for 24 hours and there was a clear color change by the end of it.

However, the yielded results are quite similar to those obtained for MCS-Cu. The lower percentage of transmittance obtained from both extracts signifies that there is a greater amount of light absorbed by the samples. The lower transmittance resembles a higher concentration at the observed bands for C-Cl stretching vibrations and CH_2 wiggling mode. Carbon species might not have appeared in the infrared spectrum due to low concentrations in the solvent. The amount of samples used was very small (less than 5 grams) but this was all what's available. It could also be that the extraction needs to run for a period of time even longer than 24 hours. Trying another solvent for extraction could also help in extracting the carbon species.

6 Conclusion

Dimethyldichlorosilane is produced in the direct process and it is the key product used for the production of silicone materials. Carbon formation in the direct process is a serious issue that leads to the deactivation of the contact mass. Four different samples obtained from different process conditions were provided by Elkem Silicon Materials. A sample of pure silicon has been also provided to be used as a reference. Various characterization methods have been used to examine the provided samples such as thermogravimetric analysis, pyrolysis-gas chromatography, Raman spectroscopy, scanning electron microscopy coupled with energy dispersive X-ray spectroscopy, and X-ray diffraction. In addition to those methods, Soxhlet extraction has been conducted as an attempt to extract carbon from the carbon rich samples and the extracts were then examined by the use of attenuated total reflection Fourier-transform infrared spectroscopy.

Thermogravimetric analysis was coupled with a mass spectrometer to investigate the gases evolving from the samples upon heating. In addition to CO_2 and H_2O, other compounds such as CH_3Cl, CH_4, and Cl_2 were also observed. CH_4 only appeared for the carbon rich samples and Cl_2 only appeared for the highly chlorinated sample MCS-Cu. The effect of process temperature ,at which the samples were extracted, was noticed. MCS400 was extracted at a process temperature of 400°C and it showed high carbon content. However, the variation of temperature between 300°C and 325°had no severe effect on carbon formation as it was seen from MCS325 and MCS300. In addition, it was noticed from MCS-Cu that carbon is formed in high amounts when methyl chloride cracks on free metallic copper. The nature of the carbon formed on MCS-Cu has shown to be less stable than that seen in samples of contact mass. In agreement with pyrolysis-gas chromatography, CO_2 also appeared in the mass spectrometry of inert experiments. This shows that CO_2 in that case was the result of decomposition of hydrocarbons found in the contact mass. Pyrolysis-gas chromatography showed that the decomposition products of all the samples are oxygenated carbon compounds with high abundances seen for acids and carbon dioxide. Two unique compounds were detected from the decomposition of MCS300 and this might be due to issues that happened in the process where MCS300 was used.

Raman spectroscopy showed the characteristic peaks for silicon which showed high intensities in the contact mass samples compared to the carbon peaks detected. Sample MCS-Cu yielded several Raman spectra and this shows the high in-homogeneity of this sample. The degree of disorder of carbonaceous species seemed to have a connection

with the process temperature as it increased with the increase in process temperature. Scanning electron microscopy also showed the severe effect of increasing the process temperature. Deep consumption of contact mass was witnessed for MCS400 and this was confirmed by the crystallite size calculated from X-ray diffraction results. The reaction pits for MCS325 and MCS300 have been observed to have great similarity as well which shows again that a variation of temperature between 300°C and 325°C does not affect the contact mass much.

Elemental analysis by energy dispersive X-ray spectroscopy showed that the carbon is evenly distributed on the surface of the contact mass. Copper was seen to be concentrated in the reaction pits only for MCS400, but it was also expected to have higher concentrations in the reaction pits of MCS325 and MCS300 to show the existence of the active sites. X-ray diffraction showed the existence of active Cu_3Si phase with minimal intensity compared to the silicon phases in two of the samples. Infrared spectroscopy of extracts obtained from Soxhlet extraction did not show any unique bands that are different than the ones obtained for the solvent (dichloromethane). Separating the carbonaceous species and characterizing them by themselves could be highly beneficial in understanding the nature of the carbon that is formed during the direct process.

7 Further work

Further investigations must be done in order to comprehend the phenomena of carbon formation and how to prevent or minimize it in the direct process. As a suggestion, it would be beneficial to obtain sufficient samples in a systematic manner. This could be done by extracting samples of contact mass from the reactor at different intervals throughout a single run. Obtaining samples in such a manner could help to identify the period of time where carbon starts forming in the direct process. It would also be useful if the samples were collected and stored in an inert atmosphere. This would help in figuring out if the contact mass is somehow already oxidized when it is in the reactor. Another suggestion would be to manipulate various process conditions and see how it would affect the formation of carbon. This could be done by varying the temperature and pressure used for the process. Temperature has already shown to have a crucial effect on carbon formation in the reaction. In addition, various concentrations of catalyst and promoters could be used in order to see how they affect carbon formation. Free copper in the reaction has proven to be troublesome, and it might be useful to figure out a method to remove the free copper from the contact mass mixture.

Thermogravimetric analysis coupled with mass spectrometry has proven to be a useful method for the purpose of this project. Various compounds evolving from the samples have been identified by this method and the observed mass loss could be correlated with those compounds. It would be better if all the samples were dried prior to the experiments so the mass loss would not be correlated with drying. Pyrolysis-gas chromatography has helped in identifying the decomposition products of the contact mass. Trying with a different temperature program might yield additional information as well.

Scanning electron microscopy that is coupled with energy dispersive X-ray spectroscopy has revealed how the surface morphology varies as a function of temperature. It has also provided an idea about the reaction pits and their shapes. Investigating the contact mass with a higher resolution might reveal more helpful information. This could be done by utilizing a scanning transmission electron microscope (S(T)EM). Raman spectroscopy has revealed the degree of disorder of the carbon present in the samples. However, one should be cautious when analyzing the obtained Raman bands. Several spots should be inspected due to the in-homogeneity of the samples.
Crystallite sizes was calculated according to the X-ray diffraction results. It is a useful method to indicate how the process conditions have affected the crystallite sizes. As for Soxhlet extraction, it might be a promising experimental

method in terms of separating the carbon from the rest of the elements in the contact mass. It would be favorable if the carbon is characterized individually without the other components present in the contact mass. No references have been found for Soxhlet extraction of carbon from the contact mass, but it is suggested to run the experiment for longer periods of time and to try with various extraction solvents. It might also be necessary to characterize the obtained extract with a method other than attenuated total reflection Fourier-transform infrared spectroscopy. In addition to all of the used characterization methods, it might be also be useful to utilize X-ray photoelectron spectroscopy in order to examine the chemical state of the samples. This would also help to identify the different types of bonds between the elements found in the samples.

References

[1] André Colas, *Silicones: Preparation, Properties and Performance*, Dow Corning, Life Sciences, **2005**.

[2] E. Yilgör, I. Yilgör, *Silicone containing copolymers: Synthesis, properties and applications*, Prog. Polym. Sci. 39 **(2014)** 1165–1195. doi:10.1016/j.progpolymsci.2013.11.003.

[3] T.B. Longenberger, K.M. Ryan, W.Y. Bender, A.K. Krumpfer, J.W. Krumpfer, *The Art of Silicones: Bringing Siloxane Chemistry to the Undergraduate Curriculum*, J. Chem. Educ. 94 **(2017)** 1682–1690. doi:10.1021/acs.jchemed.6b00769.

[4] W.J. Ward, A. Ritzer, K.M. Carroll, J.W. Flock, *Catalysis of the Rochow Direct Process*, J. Catal. 100 **(1986)** 240–249. doi:10.1016/0021-9517(86)90089-8.

[5] D. Seyferth, *Dimethyldichlorosilane and the Direct Synthesis of Methylchlorosilanes. The Key to the Silicones Industry* , Organometallics. 20 **(2002)** 4978–4992. doi:10.1021/om0109051.

[6] C. Wang, T. Liu, Y. Huang, G. Wang, J. Wang, *Promoter effects of Zn and Sn in the direct synthesis of methylchlorosilanes*, Ind. Eng. Chem. Res. 52 **(2013)** 5282–5286. doi:10.1021/ie303515q.

[7] J.C. Vlugter, R.J.H. Voorhoeve, *Mechanism and Kinetics of the Metal-Catalyzed of Methylchlorosilanes Synthesis*, J. Catal. 228 **(1965)** 220–228.

[8] P.J. Launer, *Hydrocarbon By-Products from the Rochow Direct Process for Methylchlorosilanes*, Journal of Chemical and Engineering Data. 11, **(1996)** 621–622. doi:10.1021/je60031a058.

[9] J. Acker, K. Bohmhammel, *Thermodynamic assessment of the copper catalyzed direct synthesis of methylchlorosilanes*, J. Organomet. Chem. 693 **(2008)** 2483–2493. doi:10.1016/j.jorganchem.2008.04.026

[10] D.T. Hurd, E.G. Rochow, *On the Mechanism of the Reaction between Methyl Chloride and Silicon-Copper*, J. Am. Chem. Soc. 67 **(1945)** 1057–1059. doi:10.1021/ja01223a007.

[11] A.L. Klebansky and V.S. Fikhtengolts, Journal Gen. Chem., 27 **(1957)**

[12] J. Joklík, M. Kraus, V. Bažant, *Organosiliciumverbindungen XXIX. Kinetik der direkten Synthese der Methylbromsilane*, Collect. Czech. Chem. Commun. **(1962)**, 27, 974-978. doi.org/10.1135/cccc19620974

[13] Y. Zhang, Y. Ji, J. Li, H. Liu, X. Hu, Z. Zhong, F. Su, *Morphology-dependent catalytic properties of nanocupric oxides in the Rochow reaction*, Nano Res. 11 **(2018)** 804–819. doi:10.1007/s12274-017-1689-x.

[14] M.P. Clarke, *The Direct Synthesis of Methylchlorosilanes*, Elsevier Sequoia S.A., J. of Organometallic Chemistry:376, **(1989)** 165–222.

[15] T.C. Frank, K.B. Kester, J.L. Falconer, *Surface Analysis of Methylchlorosilane Formation Catalysts*, J. Catal. 95 **(1985)** 396–405.

[16] R.J.H. Voorhoeve, J.C. Vlugter, *Mechanism and Kinetics of the Metal-Catalyzed of Methylchlorosilanes Synthesis*, J. Catal. 4 **(1965)** 123–133.

[17] C. Wang, G. Wang, J. Wang, *A Bi-component Cu catalyst for the direct synthesis of methylchlorosilane from silicon and methyl chloride*, Chinese J. Chem. Eng. 22 **(2014)** 299–304. doi:10.1016/S1004-9541(14)60034-3.

[18] A.D. Gordon, B.J. Hinch, D.R. Strongin, *Effects of individual promoters on the Direct Synthesis of methylchlorosilanes*, J. Catal. 266 **(2009)** 291–298. doi:10.1016/j.jcat.2009.06.026.

[19] J.P. Kim, D.G. Rethwisch, *The direct synthesis of methylchlorosilanes I. Steady-state and transient reaction kinetics*, J. Catal. 134 **(1992)** 168–178. doi:10.1016/0021-9517(92)90219-8.

[20] C.H. Bartholomew, *Mechanisms of catalyst deactivation*, 212 **(2001)** 17–60

[21] K. Kumbilieva, L. Petrov, *Reaction mechanism and deactivation modes of heterogeneous catalytic systems*, Rev. Roum. Chim. 53 **(2008)** 425–430. doi:10.1016/S1872-2067(10)60181-7.

[22] P.G. Menon, *Coke on catalysts-harmful, harmless, invisible and beneficial types*, J. Mol. Catal. 59 **(1990)** 207–220. doi:10.1016/0304-5102(90)85053-K.

[23] W. Luo, G. Wang, J. Wang, *Surface morphology and catalytic activity of the contact mass in organosilane synthesis*, Chem. Eng. Commun. 193 **(2006)** 754–763. doi:10.1080/00986440500267162.

[24] J.R. Anderson, B.H. McConkey, *Reactions of methyl chloride and of methylene chloride at metal surfaces. II. Reactions over evaporated films of titanium and other metals*, J. Catal. 11 **(1968)** 54–70. doi:10.1016/0021-9517(68)90009-2.

[25] T.J. Wessel, D.G. Rethwisch, *Deactivation of CuSi and CuZnSnSi due to coke formation during the direct synthesis of methylchlorosilanes*, J. Catal. 161 **(1996)** 861–866. doi:10.1006/jcat.1996.0248.

[26] S. Zou, Y. Ji, J. Li, Y. Zhang, Z. Jin, L. Jia, X. Guo, Z. Zhong, F. Su, *Novel leaflike Cu-O-Sn nanosheets as highly efficient catalysts for the Rochow reaction*, J. Catal. 337 **(2016)** 1–13. doi:10.1016/j.jcat.2016.01.009.

[27] W.F. Banholzer, N. Lewis, W. Ward, *Active site formation in the direct process for methylchlorosilanes*, J. Catal. 101 **(1986)** 405–415. doi:10.1016/0021-9517(86)90268-X.

[28] J.R. MacCallum, *Thermogravimetric analysis of polymers for assessing thermal degradation*, Thermochim. Acta. 96 **(1985)** 275–281. doi:10.1016/0040-6031(85)80068-X.

[29] B. Malič, A. Kupec, M. Kosec, *Thermal analysis*, Tsinghua University Press Limited, **(2013)**. doi:10.1007/978-3-211-99311-8-7

[30] S.J. Park, M.K. Seo, *Composite Characterization*, **(2011)**. doi:10.1016/B978-0-12-375049-5.00008-6.

[31] M. Wagner, *Introduction to Thermal Analysis*, Therm. Anal. Pract. **(2017)** 10–15. doi:10.3139/9781569906446.001.

[32] G. Höhne, W.F. Hemminger, H.-J. Flammersheim, *Differential Scanning Calorimetry*, Springer Science Business Media, **(2013)**

[33] University of Cambridge, Materials Science Metallurgy, *Differential Scanning Calorimetry*, URL:*https://www.phase-trans.msm.cam.ac.uk/2002/Thermal2.pdf*

[34] T.P. Wampler, *Pyrolysis Gas Chromatography*, Gas Chromatogr. **(2012)** 291–306. doi:10.1016/B978-0-12-385540-4.00011-0.

[35] E. Stauffer, J.A. Dolan, R. Newman, *Fire Debris Analysis*, Academic press, **(2008)** 235-293. doi.org/10.1016/B978-012663971-1.50012-9

[36] K.L. Sobeih, M. Baron, J. Gonzalez-Rodriguez, *Recent trends and developments in pyrolysis-gas chromatography*, J. Chromatogr. A. 1186 **(2008)** 51–66. doi:10.1016/j.chroma.2007.10.017.

[37] G.S. Bumbrah, R.M. Sharma, *Raman spectroscopy – Basic principle, instrumentation and selected applications for the characterization of drugs of abuse*, Egypt. J. Forensic Sci. 6 **(2016)** 209–215. doi:10.1016/j.ejfs.2015.06.001.

[38] A.D. Brooker, D.M. Leak, M.J. Lainchbury, B. Bennett, C.J. Dawe, M.J. Hill, *SEM-Raman spectroscopy*, Second Edition, Elsevier B.V., **(2018)**. doi:10.1201/9781351074636.

[39] N. John, S. George, *Raman Spectroscopy*, Spectrosc. Methods Nanomater. Charact. 2 **(2017)** 95–127. doi:10.1016/B978-0-323-46140-5.00005-4.

[40] A. Merlen, J. Buijnsters, C. Pardanaud, *A Guide to and Review of the Use of Multiwavelength Raman Spectroscopy for Characterizing Defective Aromatic Carbon Solids: from Graphene to Amorphous Carbons*, **(2017)**. doi:10.3390/coatings7100153.

[41] B. Karmakar, *Fundamentals of Glass and Glass Nanocomposites*, Elsevier Inc., **(2016)**. doi:10.1016/B978-0-323-39309-6.00001-8.

[42] A. Bogner, P.H. Jouneau, G. Thollet, D. Basset, C. Gauthier, *A history of scanning electron microscopy developments: Towards "wet-STEM" imaging*, Micron. 38 **(2007)** 390–401. doi:10.1016/j.micron.2006.06.008.

[43] Joseph I. Goldstein, Dale E. Newbury, Joseph R. Michael, Nicholas W.M. Ritchie, John Henry J. Scott, David C. Joy; *Scanning Electron Microscopy and X-ray Microanalysis*, Fourth Edition, Springer, **(2017)**

[44] A. Yoshida, Y. Kaburagi, Y. Hishiyama, *Chapter 5 - Scanning Electron Microscopy*, Tsinghua University Press Limited, **(2016)**. doi:10.1016/B978-0-12-805256-3.00005-2.

[45] J. Epp, *X-Ray Diffraction (XRD) Techniques for Materials Characterization*, Elsevier Ltd, **(2016)**. doi:10.1016/B978-0-08-100040-3.00004-3.

[46] A.K. Chatterjee, *Handbook of Analytical Techniques in Concrete Science and Technology: X-Ray Diffraction*, William Andrew Inc., **(2001)** 275-332 doi:10.1016/B978-0-8155-1437-4.50011-4.

[47] B.C. Smith, *Fundamentals of Fourier Transform Infrared Spectroscopy*, 2nd ed., CRC Press, **(2011)**. doi.org/10.1201/b10777

[48] A. Subramanian, L. Rodriguez-Saona, *Fourier Transform Infrared (FTIR) Spectroscopy*, 1st ed., Elsevier Inc., 2009. doi:10.1016/B978-0-12-374136-3.00007-9.

[49] M.D. Luque de Castro, L.E. García-Ayuso, *Soxhlet extraction of solid materials: An outdated technique with a promising innovative future*, Anal. Chim. Acta. 369 **(1998)** 1–10. doi:10.1016/S0003-2670(98)00233-5.

[50] K. Uchinokura, T. Sekine, Etsuyuki Matsuura, *Raman scattering by silicon*, Solid State Communications 11, **(1972)** 47-49. doi.org/10.1016/0038-1098(72)91127-1

[51] B. Graczykowski, A. El Sachat, J.S. Reparaz, M. Sledzinska, M.R. Wagner, S. Volz, Y. Wu, F. Alzina, C.M.S. Torres, Y. Wu, *Thermal conductivity and air-mediated losses in periodic porous silicon membranes at high temperatures*,Nat Commun.8, **(2017)** 415. doi:10.1038/s41467-017-00115-4.

[52] C. Brolly, J. Parnell, S. Bowden, *Raman spectroscopy: Caution when interpreting organic carbon from oxidising environments*, Planet. Space Sci. 121 **(2016)** 53–59. doi:10.1016/j.pss.2015.12.008.

[53] J.F. Xu, W. Ji, Z.X. Shen, W.S. Li, S.H. Tang, X.R. Ye, D.Z. Jia, X.Q. Xin, *Raman Spectra of CuO Nanocrystals*, J. Raman Spectrosc. 30, **(1999)** 413-415. https://doi.org/10.1002/(SICI)1097-4555(199905)30:5<413::AID-JRS387>3.0.CO;2-N

[54] D.R. Tallant, T.A. Friedmann, N.A. Missert, M.P. Siegal, J.P. Sullivan, *Raman Spectroscopy of Amorphous Carbon,* 498 **(1997)**. doi:10.1557/proc-498-37.

[55] P.J. Larkin, *General Outline for IR and Raman Spectral Interpretation,* Infrared Raman Spectrosc. **(2018)** 135–151. doi:10.1016/b978-0-12-804162-8.00007-0.

[56] M. Chen, R. Guo, Y. Zhao, S. Weng, Y. Xu, I. Noda, J. Wu, *Investigation on the intermolecular interaction between diethyl ether and dichloromethane in gaseous phase by using the DAOSD approach,* J. Mol. Struct. 1124 **(2016)** 244–248. doi:10.1016/j.molstruc.2015.12.015.

[57] G. Socrates, *Infrared and Raman Characteristic Group Frequencies Tables and Charts,* Third Edition, John Wiley sons, **(2001)**. https://doi.org/10.1002/jrs.1238

[58] X. Chen, L. Jia, Y. Wang, L. Song, Y. Zhu, W. Liu, Z. Zhong, F. Su, *Solvothermal synthesis of copper (I) chloride microcrystals with different morphologies as copper-based catalysts for dimethyldichlorosilane synthesis,* J. Colloid Interface Sci. 404 **(2013)** 16–23. doi:10.1016/j.jcis.2013.04.028.

Appendix A SIL Measurements

A.1 Thermogravimetric analysis

After drying in air at a temperature of 200°C, the pure silicon sample, SIL, has been examined in an oxidizing atmosphere in thermogravimetric analysis. This has been done in order to see the behavior of pure silicon in an oxidizing atmosphere. The sample shows a mass gain throughout the whole experiment. The mass gain accounted for about 0.45% of the initial mass and this is due to the oxidation of the sample. This type of mass gain was seen with other samples in oxidizing atmosphere after the carbon has evolved. The results for SIL in an oxidizing atmosphere are shown in Figure A.1.

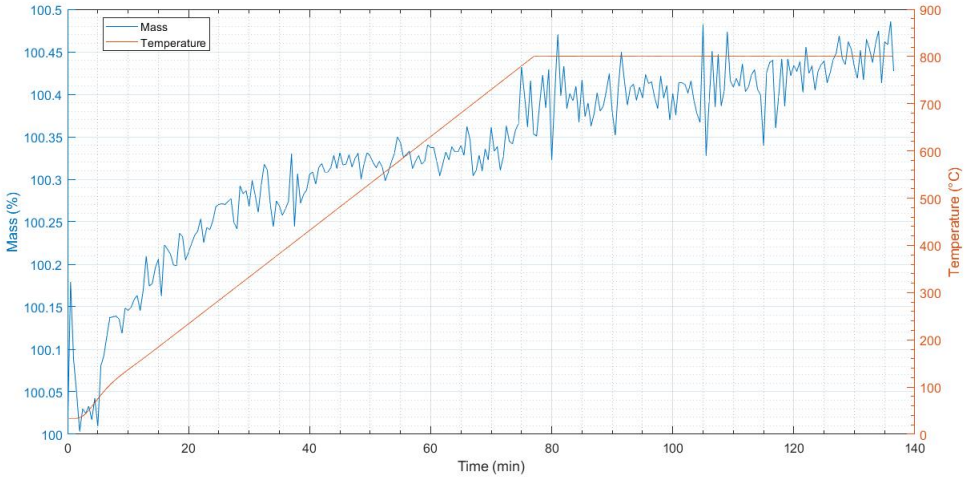

Figure A.1: Mass change as a function of temperature and time in sample SIL in an oxidizing atmosphere

A.2 Raman spectroscopy

Raman spectroscopy has been done on SIL in order to be used as a reference for the silicon bands in the Raman spectra obtained with the other samples. Pure silicon has shown to have five peaks that are located around 302cm^{-1}, 433cm^{-1}, 520cm^{-1}, 617cm^{-1}, and 941cm^{-1}. Raman spectra of SIL confirms that those peaks obtained around the same Raman shift with MCS400, MCS325, and MCS300 belong to crystalline silicon. The peak with highest intensity is also located at 520cm^{-1} and it has been cut down to show the other peaks clearly. Raman spectra of SIL can be seen in Figure A.2.

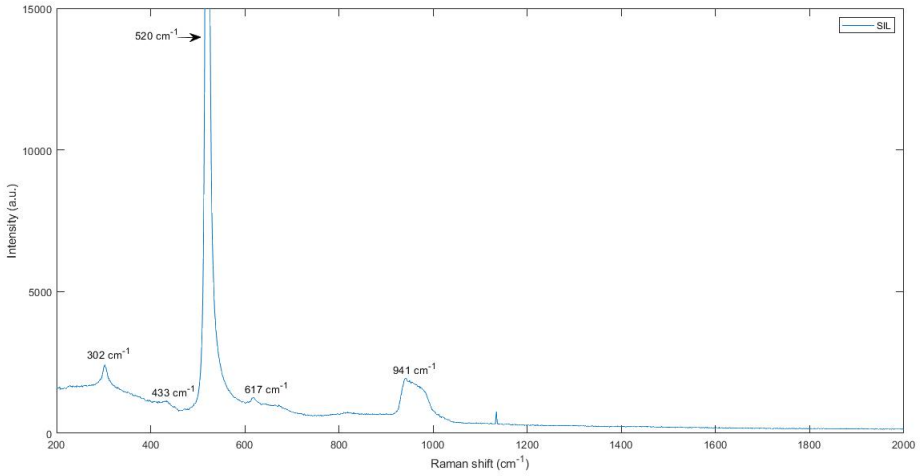

Figure A.2: Raman spectra of SIL in the visible light region. Highest intensity peak at 520cm^{-1} has been cut down in order to see the other peaks clearly.

A.3 X-ray diffraction

Sample SIL was examined with X-ray diffraction in order to be used as a reference for silicon peaks appearing in the other tested samples. The results have been matched with silicon peaks from the database. The results obtained from X-ray diffraction of sample SIL are shown in Figure A.3.

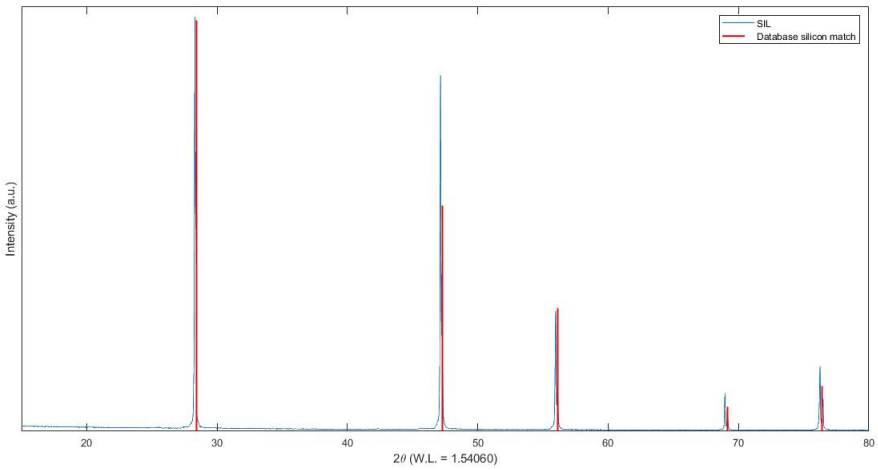

Figure A.3: X-ray diffractogram obtained for sample SIL within the 2θ range of 15°- 80°. Diffraction lines of silicon obtained from the database were added as a reference.

Appendix B X-ray diffraction additional data

In addition to the silicon phases detected in MCS400 and MCS300, the η-phase (Cu_3Si) has also been detected in those two samples with minimal intensities compared to silicon peaks. The Cu_3Si phase for MCS400 and MCS300 was detected in the range of 2θ 44°- 46°. This phase has been matched with peaks from the database indicating that it is Cu_3Si phase. The Cu_3Si phase has been plotted for MCS400 and MCS300 in Figures B.1 and B.2 respectively.

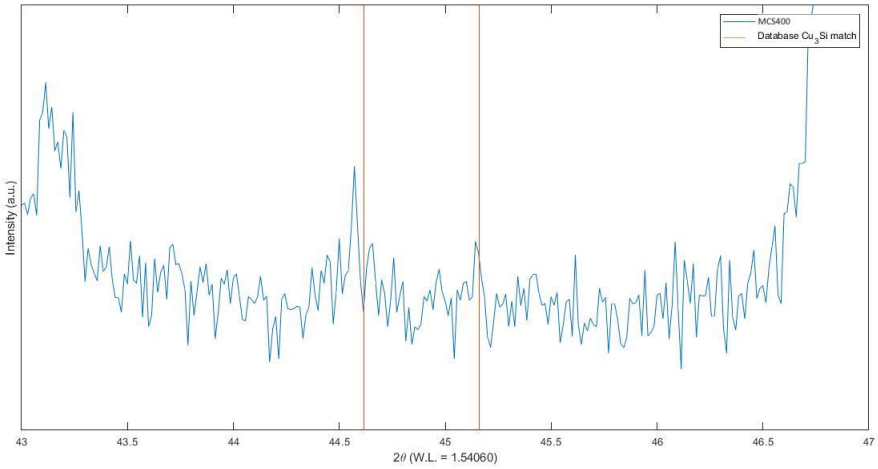

Figure B.1: X-ray diffractogram obtained for sample MCS400 within the 2θ range of 43°- 47°. Diffraction lines of Cu_3Si obtained from the database were added as a reference.

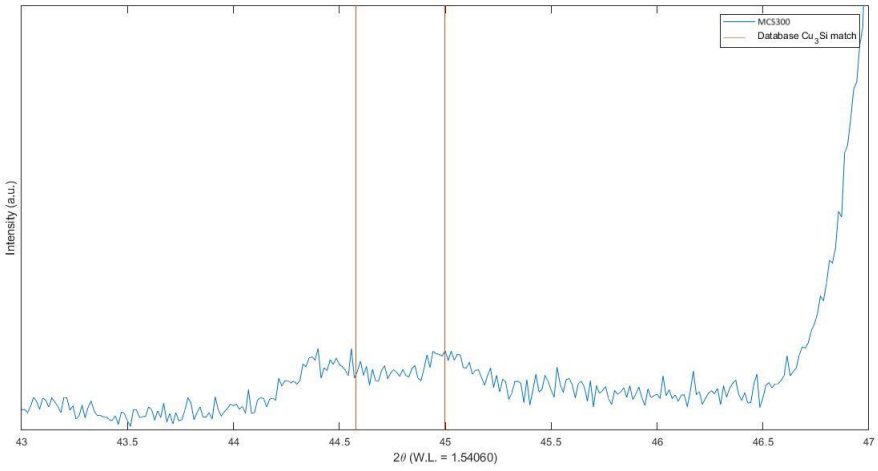

Figure B.2: X-ray diffractogram obtained for sample MCS300 within the 2θ range of 43°- 47°. Diffraction lines of Cu_3Si obtained from the database were added as a reference.

B.1 Crystallite size calculations

Crystallite sizes have been calculated by using the Scherrer equation stated in Equation 2.16. L is the crystallite size in angstrom, k is a constant that has a value of 1, λ is the value of the wavelength which is 1.54060, β is the width at half peak height (FWHM) in radians, and θ is the half value of 2θ.

The most intense peak for silicon is located at 2θ 28°and for that purpose the θ value used to calculate the crystallite sizes is 14°. The FWHM is converted to radians by using Equation B.1.

$$\frac{1° \times \pi}{180} = radians \tag{B.1}$$

For MCS400, the obtained FWHM is 0.167°:

$$L = \frac{1 \times 1.54060}{\frac{0.167 \times \pi}{180} \times \cos(14)} = 544\text{Å} = 54nm$$

For MCS325, the obtained FWHM is 0.083°:

$$L = \frac{1 \times 1.54060}{\frac{0.083 \times \pi}{180} \times \cos(14)} = 1096\text{Å} = 109nm$$

For MCS300, the obtained FWHM is 0.088°:

$$L = \frac{1 \times 1.54060}{\frac{0.088 \times \pi}{180} \times \cos(14)} = 1033\text{Å} = 103nm$$

Appendix C Pyrolysis-gas chromatography-mass spectrometry database search results

C.1 MCS-Cu

Compound number (#)	RT (min)	Scan number (#)	Area (Ab*s)	Baseline Heigth (Ab)	Absolute Heigth (Ab)	Peak Width 50% (min)	Hit Number	Hit Name	Quality	Mol Weight (amu)	Entry Number Library
1	2.278	643	105228	26316	26624	0.259	1	Carbon dioxide	3	43.99	82
							2	Carbon dioxide	3	43.99	81
							3	Nitrous oxide	3	44.001	83
							4	Nitrous oxide	3	44.001	84
							5	Acetaldehyde	2	44.026	72
							6	Ethyne, fluoro-	2	44.006	77
							7	Acetaldehyde	2	44.026	71
							8	Ethyne, fluoro-	2	44.006	76
							9	Ethylene oxide	2	44.026	75
							10	Ethylene oxide	2	44.026	73
							11	Ethylene oxide	2	44.026	74
							12	Propane	1	44.063	80
							13	Propane	1	44.063	79
							14	Propane	1	44.063	78
							15	Carbamic acid, monoammonium salt	1	78.043	1029
							16	Hydroxyurea	1	76.027	968
							17	Phenol, 4-[2-(methylamino)ethyl]-	1	151.1	24994
							18	dl-Alanyl-l-alanine	1	160.085	31013
							19	1,2-Propanediamine	1	74.084	788
							20	1,2-Propanediamine	1	74.084	792
2	23.376	6836	221916	47840	48370	0.317	1	n-Hexadecanoic acid	98	256.24	107547
							2	Tridecanoic acid	93	214.193	72647
							3	n-Hexadecanoic acid	91	256.24	107549
							4	Tridecanoic acid	83	214.193	72646
							5	Tridecanoic acid	64	214.193	72648
							6	Pentadecanoic acid	58	242.225	95851
							7	Dodecanoic acid	53	200.178	61122
							8	n-Hexadecanoic acid	53	256.24	107548
							9	Tetradecanoic acid	52	228.209	84453
							10	Pentadecanoic acid	52	242.225	95855
							11	Tetradecanoic acid	50	228.209	84452
							12	Tetradecanoic acid	50	228.209	84455
							13	Tridecanoic acid	50	214.193	72643
							14	Dodecanoic acid	47	200.178	61121
							15	Dodecanoic acid	43	200.178	61120
							16	n-Decanoic acid	43	172.146	39474
							17	n-Decanoic acid	35	172.146	39473
							18	Estra-1,3,5(10)-trien-17.beta.-ol	35	256.183	107688
							19	Decanoic acid, silver(1+) salt	27	278.044	125286
							20	Ethanone, 1-(4,5-dihydro-2-thiazolyl)-	22	129.025	12837
3	26.746	7825	300993	52929	55013	0.954	1	Octadecanoic acid	99	284.272	131262
							2	Octadecanoic acid	99	284.272	131261
							3	Octadecanoic acid	99	284.272	131259
							4	Octadecanoic acid	99	284.272	131258
							5	Octadecanoic acid	94	284.272	131260
							6	Pentadecanoic acid	86	242.225	95851
							7	Octadecanoic acid, 2-(2-hydroxyethoxy)ethyl ester	80	372.324	198268
							8	Tetradecanoic acid	68	228.209	84455
							9	Tetradecanoic acid	68	228.209	84452
							10	n-Hexadecanoic acid	64	256.24	107549
							11	n-Decanoic acid	64	172.146	39469
							12	Tetradecanoic acid	58	228.209	84453
							13	n-Decanoic acid	58	172.146	39470
							14	Tridecanoic acid	52	214.193	72643
							15	Pentadecanoic acid	45	242.225	95855
							16	Undecanoic acid	38	186.162	50052
							17	n-Decanoic acid	30	172.146	39474
							18	n-Decanoic acid	30	172.146	39473
							19	Oxalic acid, pentadecyl propyl ester	15	342.277	178430
							20	Oxalic acid, propyl tetradecyl ester	11	328.261	167553

Figure C.1: Library search results for sample MCS-Cu. The chosen compounds with suitable compatability have been highlighted

C.2 MCS300

Compound number (#)	RT (min)	Scan number (#)	Area (Ab*s)	Baseline Heigth (Ab)	Absolute Heigth (Ab)	Peak Width 50% (min)	Hit Number	Hit Name	Quality	Mol Weight (amu)	Entry Number	Library
1	0.803	210	3340	1828	2440	0.061	1	1,3,5-Triazine-2,4,6-triamine, N,N-dihexyl-N',N''-diphenyl-	7	446.316	226297	
							2	16-Epi-estriol-3 -TMS-phenylboronate	7	446.245	226296	
							3	Imidazole, 2,4,5-triiodo-	3	445.727	226491	
							4	Rhodium, (.eta.5-2,4-cyclopentadien-1-yl)[(1,2,3,4-.eta.)-2-(1,1-dimethylethyl)-3,4-diphenylphosphete]-	3	446.067	226196	
							5	Benzo-15-crown-5, 4'-(1,4,6,7-tetrahydro-1-methyl-5,8-dioxoimidazo[4,5-e][1,4]diazepin-7-yl)-	3	446.18	226149	
							6	Daidzein, bis(trifluoroacetate)	3	446.023	226130	
							7	Acetic acid, trifluoro-, 1-[(1,2,3,6-tetrahydro-1,3-dimethyl-2,6-dioxo-7H-purin-7-yl)methyl]-1,2-ethanediyl ester	3	446.066	226096	
							8	2,5-Diacetyl-3',4',6,7-tetramethoxyisoflavan	3	446.158	226173	
2	0.861	227	8509	3816	4443	0.221	1	Ethyne, fluoro-	2	44.006	77	
							2	Carbon dioxide	2	43.99	81	
							3	Ethylene oxide	2	44.026	75	
							4	Carbon dioxide	2	43.99	82	
							5	Nitrous oxide	2	44.001	84	
							6	Acetaldehyde	2	44.026	71	
							7	Ethyne, fluoro-	2	44.006	76	
							8	Nitrous oxide	2	44.001	83	
							9	Acetaldehyde	2	44.026	72	
							10	Ethylene oxide	2	44.026	74	
							11	Ethylene oxide	2	44.026	73	
							12	(2,2-Dichlorocyclopropyl)methanol	2	139.98	18128	
							13	Ethanedial, dioxime	2	88.027	1944	
							14	2-Hexynoic acid	2	112.052	6359	
							15	1,1-Cyclopropanedicarboxamide	2	128.059	12047	
							16	Furazan-3-carboxamide, oxime, 4-amino-N,N-dimethyl-	2	171.076	39157	
							17	Ethanone, 1-(4-pyridinyl)-, oxime	2	136.064	16162	
							18	Benzaldehyde, 3,5-dichloro-2-hydroxy-, 2,2-dimethylhydrazone	2	232.017	87936	
							19	Ethyl 2-(bromomethyl)acrylate	1	191.979	54815	
							20	Propane	1	44.063	80	
3	2.255	636	18803	5395	5678	0.15	1	Acetaldehyde	2	44.026	71	
							2	Ethyne, fluoro-	2	44.006	76	
							3	Carbon dioxide	2	43.99	82	
							4	Nitrous oxide	2	44.001	83	
							5	Nitrous oxide	2	44.001	84	
							6	Ethyne, fluoro-	2	44.006	77	
							7	Ethylene oxide	2	44.026	75	
							8	Acetaldehyde	2	44.026	72	
							9	Carbon dioxide	2	43.99	81	
							10	Ethylene oxide	2	44.026	73	
							11	Ethylene oxide	2	44.026	74	
							12	Propane	1	44.063	80	
							13	Propane	1	44.063	79	
							14	Propane	1	44.063	78	
							15	Carbamic acid, monoammonium salt	1	78.043	1029	
							16	1,2-Propanediamine	1	74.084	788	
							17	Benzeneethanamine, 3-fluoro-.beta.,5-dihydroxy-N-methyl-	1	185.085	49742	
							18	Phenol, 4-[2-(methylamino)ethyl]-	1	151.1	24994	
							19	2-Octanamine	1	129.152	13026	
							20	n-Hexylmethylamine	1	115.136	7886	
4	17.071	4985	35340	2186	2888	0.644	1	1,2,4-Triazolo[4,3-a]pyridin-3(2H)-one, 5-methyl-	9	149.059	23501	
							2	3-Amino-5-(2-furyl)pyrazole	9	149.059	23492	
							3	3-(4-Pyridyl)acrylic acid	9	149.048	23518	
							4	5-Chloro-2-methyl-3(2H)-isothiazolone	9	148.97	23415	
							5	Benzene, 1-isocyanato-3-methoxy-	9	149.048	23541	
							6	9-Aza-bicyclo[4.2.1]nona-2,4-diene-9-carboxaldehyde	9	149.084	23659	
							7	Tricyclo[4.3.1.1(3,8)]undecane, 1-bromo-	9	228.051	83946	
							8	Phthalic acid, hexyl 3-methoxybenzyl ester	9	370.178	196803	
							9	Tricyclo[4.3.1.1(3,8)]undecane-1-carboxylic acid, methyl ester	9	208.146	67769	
							10	Adamantane, 1,3-dimethyl-	9	164.157	33749	
							11	Adamantane, 1-isothiocyanato-3-methyl-	9	207.108	66928	
							12	Tricyclo[4.3.1.1(3,8)]undecane, 1-chloro-	9	184.102	48422	
							13	Adamantane, 1,3-dimethyl-	9	164.157	33752	
							14	2,3-Dihydroindole-4-ol-2-one	7	149.048	23532	
							15	1H-S-Triazolo[1,5-a]pyridin-4-ium, 2-hydroxy-1-methyl-, hydroxide, inner salt	7	149.059	23503	
							16	Ethanone, 1-(4-nitrosophenyl)-	7	149.048	23535	
							17	4-Isopropenyl-1-methylbicyclo[4.1.0]heptan-2-one oxime	7	179.131	44844	
							18	Benzo[1,3]dioxole-5-carboxamide, N-benzothiazol-2-yl-	5	298.041	142432	
							19	Oxazolidine, 3-phenyl-	5	149.084	23601	
							20	2H-1,3-Benzimidazol-2-one, 5-amino-1,3-dihydro-	5	149.059	23499	
5	17.374	5074	15098	8115	8583	0.136	1	Phthalic acid, 2-ethoxyethyl ethyl ester	83	266.115	115325	
							2	Phthalic acid, ethyl 2-(2-nitrophenyl)ethyl ester	78	343.106	179006	
							3	Phthalic acid, ethyl hex-2-yn-4-yl ester	78	274.121	122730	
							4	2-(Nonyloxycarbonyl)benzoic acid	72	292.167	137725	
							5	2-(Octyloxycarbonyl)benzoic acid	64	278.152	125795	
							6	Phthalic acid, monoamide, N-ethyl-N-(3-methylphenyl)-, ethyl ester	64	311.152	153790	
							7	Phthalic acid, monocyclohexyl ester	64	248.105	100546	
							8	Phthalic acid, cyclobutyl ethyl ester	64	248.105	100550	
							9	Phthalic acid, 2-ethoxyethyl pentyl ester	56	308.162	151133	
							10	2-((4-Methylpentyloxy)carbonyl)benzoic acid	56	250.121	102181	
							11	2-(sec-Butoxycarbonyl)benzoic acid	50	222.089	78810	
							12	2-(Pentyloxycarbonyl)benzoic acid	50	236.105	90420	
							13	Diethyl Phthalate	50	222.089	78786	
							14	1,2-Benzenedicarboxylic acid, monobutyl ester	50	222.089	78837	
							15	5-Methylthieno[3,2-b]pyridine	50	149.03	23567	
							16	1,2-Benzenedicarboxylic acid, butyl 2-ethylhexyl ester	50	334.214	172655	
							17	1,2-Benzenedicarboxylic acid, mono(2-ethylhexyl) ester	50	278.152	125890	
							18	2-(Heptyloxycarbonyl)benzoic acid	50	264.136	113875	
							19	Diethyl Phthalate	50	222.089	78782	
							20	2-(Hexyloxycarbonyl)benzoic acid	45	250.121	102155	
6	19.684	5752	7901	944	1202	0.273	1	(7-Methylbenzo(b)thien-3-yl)methanol	5	178.045	43654	
							2	2H-1-Benzothiopyran, 2-ethyl-3,4-dihydro-	5	178.082	43932	
							3	1-Piperidinecarboxaldehyde, 2-(1H-pyrrol-2-yl)-	5	178.111	43695	
							4	Phenol, 2-ethoxy-4-(2-propenyl)-	5	178.099	43793	
							5	8-Fluoro-1-benzosuberone	5	178.079	43726	
							6	2-Adamantylamine, N,N-dimethyl-	5	179.167	44859	
							7	2,3,5,6-Tetrafluorobenzaldehyde	5	178.004	44362	
							8	(7-Methylbenzo(b)thien-2-yl)methanol	5	178.045	43655	
							9	Phenol, 2-ethoxy-5-(1-propenyl)-	5	178.099	43792	
							10	Acethydrazide, N2-(2,4-dimethylphenyl)-	5	178.111	43682	
							11	Propane-1,3-diamine, N,N'-bis(4-methoxybenzyl)-	4	314.199	156519	
							12	1,2,5,6-Tetrahydropyridine, 1-(2-thienylmethyl)-	4	179.077	44782	
							13	Urea, 1-cyclopropylmethyl-3-[1-(3-isopropenylphenyl)-1-methylethyl]-1-propyl-	4	314.236	156669	
							14	Silane, dimethyl(dimethyl(4-methoxybenzyloxy)silyloxy)ethoxy-	4	314.137	155896	
							15	Propenone, 1-(4-fluorophenyl)-3-[3-(4-fluorophenyl)-3-oxo-1-propenyloxy]-	3	314.075	156200	
							16	4-Pyridinecarboxylic acid, butyl ester	3	179.095	44704	
							17	Niketh amide	3	178.111	43662	
							18	Phthalic acid, ethyl 4-methoxybenzyl ester	3	314.115	156212	
							19	4,7-Ethano-1H-inden-1-one, 3a,4,5,6,7,7a-hexahydro-3-hydroxy-	3	178.099	43918	
							20	N-(4-Chlorophenyl)-4-hydroxy-2(1H)-oxo-3-quinolinecarboxamide	3	314.046	155997	

Figure C.2: Library search results for sample MCS300 (1). The chosen compounds with suitable compatability have been highlighted

Compound number (#)	RT (min)	Scan number (#)	Area (Ab*s)	Baseline Heigth (Ab)	Absolute Heigth (Ab)	Peak Width 50% (min)	Hit Number	Hit Name	Quality	Mol Weight (amu)	Entry Number	Library
7	23.356	6830	63930	14033	14258	0.249	1	n-Hexadecanoic acid	99	256.24	107549	
							2	n-Hexadecanoic acid	95	256.24	107547	
							3	Tetradecanoic acid	53	228.209	84452	
							4	Pentadecanoic acid	52	242.225	95851	
							5	Tridecanoic acid	52	214.193	72643	
							6	Undecanoic acid	50	186.162	50051	
							7	n-Decanoic acid	50	172.146	39471	
							8	Undecanoic acid	43	186.162	50052	
							9	Lactose	43	342.116	177854	
							10	Trehalose	43	342.116	177856	
							11	1-Decanol, 2-octyl-	11	270.292	119525	
							12	Octane, 2-methyl-	10	128.157	12665	
							13	Octadecane, 2-methyl-	10	268.313	117646	
							14	Undecane, 2-methyl-	10	170.203	38324	
							15	Undecane, 4,7-dimethyl-	10	184.219	48860	
							16	Decane, 2,3,5,8-tetramethyl-	10	198.235	59901	
							17	Undecane, 5-methyl-	10	170.203	38332	
							18	Tridecane	10	184.219	48834	
							19	Undecane, 5-methyl-	10	170.203	38331	
							20	Hexadecane	10	226.266	83027	
8	25.683	7513	20835	3906	5024	0.16	1	8-Methoxy-quinoline-5-sulfonic acid butylamide	72	294.104	139109	
							2	8-Trifluoromethylnaphtho[2,1-b]thiophene-4-ethylene oxide	59	294.033	139257	
							3	Pyrido[3,2-d]pyrimidine, 2,4-diamino-6-(N-ethylbenzylamino)-	59	294.159	139319	
							4	Gona-1,3,5,7,9-pentaen-17-one, 13-ethyl-3-methoxy-, (13.alpha.)-	53	294.162	139761	
							5	Ebumamenin-14(15H)-one	53	294.173	139639	
							6	Benzo[b]naphtho[2,3-d]thiophene-6,11-dione, 8-methoxy-	50	294.035	139393	
							7	Furane-2-carboxamide, N-naphtho[1,2-d]thioazol-2-yl-	49	294.046	139258	
							8	3-Furan-2-yl-2-[4-(2-hydroxy-phenyl)-thiazol-2-yl]-acrylonitrile	47	294.046	139263	
							9	Aspidofractinine, 3-oxo-	47	294.173	139640	
							10	(1H)Benzimidazole, 2-(2-furyl)-6-(2-thienyl)carbonyl-	47	294.046	139259	
							11	Gona-1,3,5,7,9-pentaen-17-one, 13-ethyl-3-methoxy-	46	294.162	139753	
							12	4-Methylsulfanyl-N-pyridin-3-ylmethyl-benzenesulfonamide	43	294.05	139022	
							13	Indane-1,3-dione, 2-(3,4-dimethoxybenzylideno)-	43	294.089	139521	
							14	Triphenylphosphine sulfide	43	294.063	139541	
							15	3-Methoxy-D-homoestra-1,3,5(10),6,8-pentaen-17a-one, (14.alpha.)	43	294.162	139759	
							16	Benzene, 1,4-bis(phenylthio)-	43	294.054	139528	
							17	Triphenylphosphine sulfide	43	294.063	139542	
							18	3-Methoxy-D-homoestra-1,3,5(10),6,8-pentaene-17a-one, (14.beta.)	43	294.162	139760	
							19	4-(1,2,3,6,7,8-Hexahydro-4-pyrenyl)butanoic acid	38	294.162	139751	
							20	2-Pyrrolidinone, 1,5-dimethyl-3,3-diphenyl-	22	265.147	114900	
9	26.742	7824	52390	8559	11167	0.313	1	Octadecanoic acid	96	284.272	131258	
							2	Octadecanoic acid	95	284.272	131262	
							3	Octadecanoic acid	95	284.272	131260	
							4	Octadecanoic acid	87	284.272	131259	
							5	Octadecanoic acid, 2-(2-hydroxyethoxy)ethyl ester	43	372.324	198268	
							6	Octadecanoic acid	30	284.272	131261	
							7	Tetradecanoic acid	14	228.209	84453	
							8	Decanoic acid, silver(1+) salt	14	278.044	125286	
							9	Tridecanoic acid	14	214.193	72648	
							10	Tetradecanoic acid	14	228.209	84455	
							11	Pentadecanoic acid	14	242.225	95855	
							12	Tetradecanoic acid	14	228.209	84452	
							13	Pentadecanoic acid	14	242.225	95851	
							14	n-Decanoic acid	14	172.146	39474	
							15	Tridecanoic acid	14	214.193	72647	
							16	Dodecanoic acid	14	200.178	61122	
							17	n-Hexadecanoic acid	10	256.24	107549	
							18	Furo[2',3':4,5]thiazolo[3,2-g]purine-8-methanol, 4-amino-6.alpha.,7,8,9a-tetrahydro-7-hydroxy-, [6aS-(6a.alpha.,7.alpha.,8.beta.,9a.alpha.)]-	9	281.058	127862	
							19	3,4,5-Tris(methylthio)benzotrifluoride	9	283.998	130312	
							20	Isopropyl stearate	9	326.318	166202	

Figure C.3: Library search results for sample MCS300 (2). The chosen compounds with suitable compatability have been highlighted

C.3 MCS325

Compound number (#)	RT (min)	Scan number (#)	Area (Ab*s)	Baseline Heigth (Ab)	Absolute Heigth (Ab)	Peak Width 50% (min)	Hit Number	Hit Name	Quality	Mol Weight (amu)	Entry Number	Library
1	0.65	165	11193	3011	3283	0.3	1	Carbon dioxide	2	43.99	81	
							2	Ethyne, fluoro-	2	44.006	77	
							3	Ethyne, fluoro-	2	44.006	76	
							4	Ethylene oxide	2	44.026	75	
							5	Acetaldehyde	2	44.026	72	
							6	Acetaldehyde	2	44.026	71	
							7	Nitrous oxide	2	44.001	83	
							8	Nitrous oxide	2	44.001	84	
							9	Carbon dioxide	2	43.99	82	
							10	Ethylene oxide	2	44.026	74	
							11	Ethylene oxide	2	44.026	73	
							12	Propane	1	44.063	80	
							13	Propane	1	44.063	79	
							14	Propane	1	44.063	78	
							15	Phenol, 4-[2-[methylamino]ethyl]-	1	151.1	24994	
							16	Benzeneethanamine, 3-fluoro-.beta.,5-dihydroxy-N-methyl-	1	185.085	49742	
							17	Carbamic acid, monoammonium salt	1	78.043	1029	
							18	(2-Aziridinylethyl)amine	1	86.084	1623	
							19	2-Octanamine	1	129.152	13026	
							20	dl-Alanyl-l-alanine	1	160.085	31013	
2	0.953	254	16624	3462	3739	0.504	1	Propane	2	44.063	79	
							2	Carbon dioxide	2	43.99	82	
							3	Carbon dioxide	2	43.99	81	
							4	Ethyne, fluoro-	2	44.006	77	
							5	Ethyne, fluoro-	2	44.006	76	
							6	Ethylene oxide	2	44.026	75	
							7	Acetaldehyde	2	44.026	72	
							8	Acetaldehyde	2	44.026	71	
							9	Nitrous oxide	2	44.001	83	
							10	Nitrous oxide	2	44.001	84	
							11	Ethylene oxide	2	44.026	74	
							12	Ethylene oxide	2	44.026	73	
							13	Propane	1	44.063	80	
							14	Propane	1	44.063	78	
							15	Phenol, 4-[2-[methylamino]ethyl]-	1	151.1	24994	
							16	Benzeneethanamine, 3-fluoro-.beta.,5-dihydroxy-N-methyl-	1	185.085	49742	
							17	Carbamic acid, monoammonium salt	1	78.043	1029	
							18	(2-Aziridinylethyl)amine	1	86.084	1623	
							19	2-Octanamine	1	129.152	13026	
							20	dl-Alanyl-l-alanine	1	160.085	31013	
3	2.265	639	34366	8909	9171	0.14	1	Acetaldehyde	2	44.026	71	
							2	Ethyne, fluoro-	2	44.006	76	
							3	Carbon dioxide	2	43.99	82	
							4	Nitrous oxide	2	44.001	83	
							5	Nitrous oxide	2	44.001	84	
							6	Ethyne, fluoro-	2	44.006	77	
							7	Ethylene oxide	2	44.026	75	
							8	Acetaldehyde	2	44.026	72	
							9	Carbon dioxide	2	43.99	81	
							10	Ethylene oxide	2	44.026	73	
							11	Ethylene oxide	2	44.026	74	
							12	Propane	1	44.063	80	
							13	Propane	1	44.063	79	
							14	Propane	1	44.063	78	
							15	Carbamic acid, monoammonium salt	1	78.043	1029	
							16	1,2-Propanediamine	1	74.084	788	
							17	Benzeneethanamine, 3-fluoro-.beta.,5-dihydroxy-N-methyl-	1	185.085	49742	
							18	Phenol, 4-[2-[methylamino]ethyl]-	1	151.1	24994	
							19	2-Octanamine	1	129.152	13026	
							20	n-Hexylmethylamine	1	115.136	7886	
4	2.384	674	9123	2520	2972	0.14	1	2-Butene	9	56.063	172	
							2	2-Butene	9	56.063	175	
							3	1-Propene, 2-methyl-	9	56.063	188	
							4	1-Propene, 2-methyl-	7	56.063	187	
							5	1-Propene, 2-methyl-	7	56.063	186	
							6	2-Butene, (E)-	5	56.063	182	
							7	2-Butene, (Z)-	5	56.063	185	
							8	Cyclobutane	5	56.063	179	
							9	2-Butene, (E)-	5	56.063	183	
							10	2-Butene, (Z)-	5	56.063	184	
							11	2-Butene	5	56.063	174	
							12	2-Butene, (E)-	5	56.063	180	
							13	1-Butene	5	56.063	177	
							14	2-Butene, (Z)-	5	56.063	181	
							15	1-Butene	5	56.063	173	
							16	1-Butene	4	56.063	176	
							17	Cyclobutane	4	56.063	178	
							18	2-Propenal	3	56.026	166	
							19	Propane	3	44.063	80	
							20	Propane	3	44.063	79	
5	2.636	748	4932	1302	1617	0.119	1	Cyclopropane, 1,2-dimethyl-, cis-	53	70.078	581	
							2	Cyclopropane, 1,2-dimethyl-, trans-	53	70.078	584	
							3	2-Pentene, (E)-	42	70.078	562	
							4	Cyclopropane, 1,2-dimethyl-, trans-	42	70.078	583	
							5	2-Pentene	9	70.078	554	
							6	2-Butene, 2-methyl-	9	70.078	567	
							7	2-Butene, 2-methyl-	9	70.078	569	
							8	2-Pentene, (E)-	7	70.078	558	
							9	2-Methyl-1-butene	7	70.078	563	
							10	Cyclopropane, 1,1-dimethyl-	7	70.078	578	
							11	Cyclopropane, 1,1-dimethyl-	7	70.078	580	
							12	Cyclopropane, 1,2-dimethyl-, cis-	7	70.078	582	
							13	2-Butene, 2-methyl-	5	70.078	571	
							14	2-Pentene, (Z)-	4	70.078	557	
							15	1-Oxa-3,4-diazacyclopentadiene	4	70.017	495	
							16	2-Pentene	4	70.078	552	
							17	2-Pentene, (Z)-	4	70.078	559	
							18	Methyl vinyl ketone	4	70.042	542	
							19	Cyclopropane, 1,2-dimethyl-, trans-	4	70.078	585	
							20	Methyl vinyl ketone	4	70.042	539	
6	17.377	5075	3831	1578	1578	0.112	1	3,5-Diethyl-2-n-propylpyridine	5	177.152	43346	
							2	Benzene, 1-isocyanato-4-methoxy-	2	149.048	2543	
							3	Benzene, 1-isothiocyanato-4-methyl-	2	149.03	23574	
							4	1H-S-Triazolo[1,5-a]pyridin-4-ium, 2-hydroxy-1-methyl-, hydroxide, inner salt	2	149.059	23503	
							5	6-Methylthieno[2,3-b]pyridine	2	149.03	23565	
							6	m-Tolyl isothiocyanate	2	149.03	23556	
							7	4-Amino-2-methyl-5,6-trimethylenepyrimidine	2	149.095	23511	
							8	Benzene, 1-isocyanato-3-methoxy-	2	149.048	23537	
							9	Benzaldehyde, 4-(dimethylamino)-	2	149.084	23641	
							10	Benzaldehyde, 4-(dimethylamino)-	2	149.084	23644	
							11	7-Methylthieno[3,2-b]pyridine	2	149.03	23568	
							12	Benzothiazole, 2-methyl-	2	149.03	23561	
							13	Benzaldehyde, 4-(dimethylamino)-	2	149.084	23642	
							14	N,2,4,6-Tetramethylbenzenamine	2	149.12	23371	
							15	2-Ethylformanilide	2	149.084	23589	
							16	2H-1,3-Benzimidazol-2-one, 5-amino-1,3-dihydro-	2	149.059	23499	
							17	Furo[3,2-b]pyridine, 2-methyl-, 4-oxide	2	149.048	23553	
							18	Benzothiazole, 2-methyl-	2	149.03	23560	
							19	Pyridine, pentamethyl-	2	149.12	23354	
							20	Benzothiazole, 2-methyl-	2	149.03	23558	

Figure C.4: Library search results for sample MCS325 (1). The chosen compounds with suitable compatability have been highlighted

Compound number (#)	RT (min)	Scan number (#)	Area (Ab*s)	Baseline Heigth (Ab)	Absolute Heigth (Ab)	Peak Width 50% (min)	Hit Number	Hit Name	Quality	Mol Weight (amu)	Entry Number Library
7	23.366	6833	73122	17606	17844	0.194	1	n-Hexadecanoic acid	94	256.24	107547
							2	Pentadecanoic acid	58	242.225	95851
							3	Tetradecanoic acid	53	228.209	84452
							4	Tridecanoic acid	53	214.193	72647
							5	Tetradecanoic acid	53	228.209	84455
							6	Pentadecanoic acid	52	242.225	95855
							7	n-Decanoic acid	50	172.146	39469
							8	Tridecanoic acid	49	214.193	72643
							9	Pentadecanoic acid	47	242.225	95854
							10	Tridecanoic acid	47	214.193	72646
							11	Dodecanoic acid	43	200.178	61122
							12	n-Hexadecanoic acid	27	256.24	107549
							13	Undecane, 2,3-dimethyl-	10	184.219	48855
							14	Pentanedioic acid, 3-ethyl-3-methyl-, dimethyl ester	10	202.121	62306
							15	Tridecane	10	184.219	48832
							16	Oxalic acid, cyclobutyl heptadecyl ester	10	382.308	203491
							17	Pentadecane	10	212.25	71395
							18	Sulfurous acid, 2-propyl tetradecyl ester	10	320.239	161094
							19	Octatriacontyl pentafluoropropionate	10	696.584	242842
							20	Octane, 2,3,3-trimethyl-	10	156.188	28442
8	26.746	7825	73289	14770	16140	0.334	1	Octadecanoic acid	99	284.272	131262
							2	Octadecanoic acid	97	284.272	131260
							3	Octadecanoic acid	95	284.272	131259
							4	Octadecanoic acid, 2-(2-hydroxyethoxy)ethyl ester	62	372.324	198268
							5	Octadecanoic acid	49	284.272	131258
							6	Tetradecanoic acid	45	228.209	84452
							7	Octadecanoic acid	43	284.272	131261
							8	Tetradecanoic acid	43	228.209	84455
							9	Tetradecanoic acid	38	228.209	84453
							10	n-Hexadecanoic acid	38	256.24	107547
							11	Tridecanoic acid	35	214.193	72647
							12	Ethanone, 1-(4,5-dihydro-2-thiazolyl)-	30	129.025	12837
							13	Pentadecanoic acid	30	242.225	95851
							14	n-Hexadecanoic acid	30	256.24	107549
							15	Pentadecanoic acid	30	242.225	95855
							16	Ethanone, 1-(4,5-dihydro-2-thiazolyl)-	27	129.025	12836
							17	n-Decanoic acid	27	172.146	39474
							18	Tridecanoic acid	25	214.193	72648
							19	Dodecanoic acid	22	200.178	61122
							20	n-Decanoic acid	16	172.146	39473

Figure C.5: Library search results for sample MCS325 (2). The chosen compounds with suitable compatability have been highlighted

C.4 MCS400

Compound number (#)	RT (min)	Scan number (#)	Area (Ab's)	Baseline Heigth (Ab)	Absolute Heigth (Ab)	Peak Width 50% (min)	Hit Number	Hit Name	Quality	Mol Weight (amu)	Entry Number Library
1	2.254	636	135798	33374	33755	0.395	1	Carbon dioxide	4	43.99	81
							2	Ethylene oxide	3	44.026	75
							3	Carbon dioxide	3	43.99	82
							4	Nitrous oxide	3	44.001	83
							5	Nitrous oxide	3	44.001	84
							6	Ethyne, fluoro-	2	44.006	76
							7	Ethyne, fluoro-	2	44.006	77
							8	Acetaldehyde	2	44.026	71
							9	Acetaldehyde	2	44.026	72
							10	Ethylene oxide	2	44.026	74
							11	Ethylene oxide	2	44.026	73
							12	Carbamic acid, monoammonium salt	2	78.043	1029
							13	Propane	1	44.063	80
							14	Propane	1	44.063	79
							15	Propane	1	44.063	78
							16	Glycidol	1	74.037	805
							17	Glycidol	1	74.037	804
							18	dl-Alanine ethyl ester	1	117.079	8495
							19	l-Alanine ethylamide, (S)-	1	116.095	8000
							20	Benzeneethanamine, 4-fluoro-.beta.,3-dihydroxy-N-methyl-	1	185.085	49744
2	23.404	6844	143221	16863	17125	0.46	1	n-Hexadecanoic acid	96	256.24	107547
							2	Pentadecanoic acid	64	242.225	95851
							3	Tetradecanoic acid	58	228.209	84452
							4	n-Hexadecanoic acid	58	256.24	107549
							5	Tetradecanoic acid	53	228.209	84453
							6	Tetradecanoic acid	53	228.209	84455
							7	Pentadecanoic acid	53	242.225	95854
							8	Tridecanoic acid	52	214.193	72648
							9	Undecanoic acid	49	186.162	50051
							10	Undecanoic acid	47	186.162	50053
							11	Tridecanoic acid	47	214.193	72646
							12	Lactose	43	342.116	177854
							13	Pentadecanoic acid	43	242.225	95855
							14	n-Decanoic acid	43	172.146	39474
							15	n-Decanoic acid	43	172.146	39473
							16	Dodecanoic acid	43	200.178	61117
							17	n-Decanoic acid	38	172.146	39469
							18	11-Bromoundecanoic acid	38	264.072	113453
							19	n-Decanoic acid	38	172.146	39470
							20	Decanoic acid, silver(1+) salt	38	278.044	125286
3	25.853	7563	100969	3671	6507	1.042	1	Sulfurous acid, pentadecyl 2-propyl ester	27	334.254	172312
							2	Sulfurous acid, octadecyl 2-propyl ester	27	376.301	200449
							3	Ethanol, 2-(dodecyloxy)-	27	230.225	86145
							4	Ethanol, 2-(hexadecyloxy)-	25	286.287	133067
							5	Tetradecane, 1-chloro-	25	232.196	87666
							6	Tridecanoic acid, 2,2,3,3,4,4,4-heptafluorobutyl ester	23	396.19	209984
							7	Oxalic acid, 6-ethyloct-3-yl ethyl ester	22	258.183	108899
							8	Ascorbyl Palmitate	17	414.262	217163
							9	1-Dodecanol, 2-hexyl-	16	270.292	119526
							10	Oxalic acid, cyclobutyl tridecyl ester	16	326.246	165901
							11	Sulfurous acid, 2-propyl tetradecyl ester	16	320.239	161094
							12	Ethanol, 2-(dodecyloxy)-	16	230.225	86142
							13	1-Decanol, 2-octyl-	16	270.292	119525
							14	Ethanol, 2-(octadecyloxy)-	16	314.318	156673
							15	4,8-Dioxatricyclo[5.1.0.0(3,5)]octane, 1-methyl-5-(1-methylethyl)-, (1.alpha.,3.alpha.,5.alpha.,7.alpha.)-	14	168.115	36563
							16	Oxalic acid, cyclobutyl tetradecyl ester	12	340.261	176846
							17	Oxalic acid, allyl pentadecyl ester	12	340.261	176817
							18	Oxalic acid, allyl hexadecyl ester	12	354.277	186646
							19	Nonane, 1-iodo-	12	254.053	106031
							20	Oxalic acid, allyl undecyl ester	12	284.199	130915
4	26.763	7830	2081479	20517	26392	5.253	1	Octadecanoic acid	99	284.272	131262
							2	Octadecanoic acid	98	284.272	131258
							3	Octadecanoic acid	94	284.272	131260
							4	Octadecanoic acid	93	284.272	131259
							5	Octadecanoic acid	80	284.272	131261
							6	Octadecanoic acid, 2-(2-hydroxyethoxy)ethyl ester	64	372.324	198268
							7	Tetradecanoic acid	49	228.209	84452
							8	n-Decanoic acid	35	172.146	39471
							9	n-Decanoic acid	35	172.146	39469
							10	Pentadecanoic acid	35	242.225	95854
							11	n-Hexadecanoic acid	27	256.24	107549
							12	Dimethylmalonic acid, 2,5-dichlorophenyl pentyl ester	22	346.074	180892
							13	.alpha.-D-Glucopyranose, 4-O-.beta.-D-galactopyranosyl-	22	342.116	177860
							14	Maltose	22	342.116	177853
							15	5-Acetoxypentadecane	18	270.256	119376
							16	Lactose	14	342.116	177855
							17	Adipic acid, octyl trans-2-methylcyclohexyl ester	14	354.277	186719
							18	3,5-Difluorobenzaldehyde carbamoylhydrazone	11	199.056	60687
							19	2-Pentenoic acid, 2-methoxy-3-methyl-, methyl ester	10	158.094	30096
							20	Malonic acid, 3,3-dimethylbut-2-yl heptyl ester	10	286.214	132829

Figure C.6: Library search results for sample MCS400. The chosen compounds with suitable compatability have been highlighted